

Temperature Profiles and Spectra of Accretion Disks around Rapidly Rotating Neutron Stars

A Thesis
Submitted for the Degree of
Doctor of Philosophy
in the Faculty of Science

by

Sudip Bhattacharyya



Department of Physics
Indian Institute of Science
Bangalore INDIA

2001

Declaration

I hereby declare that the work reported in this thesis titled “Temperature Profiles and Spectra of Accretion Disks around Rapidly Rotating Neutron Stars” is entirely original and has been carried out by me independently in the Department of Physics, Indian Institute of Science, and Indian Institute of Astrophysics, under the Joint Astronomy Programme, under the supervisions of Dr. Pijushpani Bhattacharjee, Indian Institute of Astrophysics, Bangalore 560 034 and Dr. Arnab Rai Choudhuri, Indian Institute of Science, Bangalore 560 012. I further declare that this work has not formed the basis for the award of any degree, diploma, fellowship, associateship or similar title of any University or Institution.

(Sudip Bhattacharyya)

Department of Physics
Indian Institute of Science
Bangalore 560 012, India.

To the memory of Professor Bhaskar Datta

Acknowledgments

I thank late Dr. Bhaskar Datta for his invaluable help and guidance in the early years of my ph.d. work. His sad and untimely demise on 3rd December, 1999 has been the rudest shock I have ever received in my life.

My heartfelt thanks are to Dr. Pijush Bhattacharjee for stepping in as my official advisor after Dr. Datta's death and for constant encouragement and academic help that he has extended towards me in the later years of my ph.d. work.

I wish to thank Dr. Arnab Rai Choudhuri for the academic discussions that we have had and his support throughout my ph.d. years. I also thank Dr. Chanda J. Jog for her help.

I am grateful to Dr. Dipankar Bhattacharya for having helped me in all possible ways after the demise of Dr. Bhaskar Datta. It is with his help that I have been able to complete my ph.d. work in reasonable time.

Dr. Arun V. Thampan has stood beside me from the early days of my ph.d. work. I have used his numerical code extensively. It is a pleasure to thank him for his support.

I thank my collaborators Dr. Ranjeev Misra and Dr. Ignazio Bombaci for their cooperation academically and otherwise.

I would like to acknowledge the Director, Indian Institute of Astrophysics, for all the facilities provided. I am indebted to the faculty and scientific staff of IIA for everything that they have done for me. I thank the staff of the Director's office, the Librarian and the library staff, the computer center staff and the administrative staff for trying their best to ensure that the road towards attaining my ph.d. degree has been smooth.

I thank the Chairman, the faculty and the students of physics department, IISc. I acknowledge the staff of the physics office, especially Rakma, for their help. I also thank the Chairman of SERC, IISc and the staff there for all the state-of-the-art computation facilities provided.

I wish to thank the Director of Raman Research Institute for all the facilities provided to me. I acknowledge all the faculty members, the students, the computer center staff, the library staff and in general all my colleagues in RRI.

I thank Dr. Sreekumar and Vivek for helping me learn X-ray data analysis. I also thank Lolita, Ishwar and the rest of the staff of Technical Physics Division, ISRO for their support.

The discussions with Drs. Bala Iyer, Paul Wiita, Ajit Kembhavi and Sandip Chakrabarti were

extremely helpful for me and I thank all of them.

I thank all the past and present IISc astronomy students, especially Srikanth, Sushan, Rajguru, Dharam, Ashish, Bhaswati, Dibyendu, Girish and Resmi for their help and friendship.

I acknowledge my batchmates Subhabrata and Niruj for always being understanding and helpful to me.

I am indebted to all the students, past and present, in IIA. I specially want to thank Rajesh, Manoj, Ravindra, Maheswar, Pavan, Sonjoy, Jana, Mangala, Sridharan, Rajalakshmi, Ramchandra, Dilip and Preeti. I also thank Dr. Parthasarathy Joarder for his help.

I would like to thank Banibrata for all our discussions and I sincerely hope that he would be able to overcome his present predicament soon.

I am thankful to Ayan for his friendship and company throughout my ph.d. years. I also thank Apratim, Sutirtha, Sudipta and Sriparna for making my life in IISc so much enjoyable. I will never forget the many wonderful saturday evenings that we had in Hotel Ratna – which has been like a home outside home for me, with its quality food and general ambience. The weekend screenings of IISc Film Society and film festivals organized by the Bangalore Film Society have, besides exposing me to the best cinema of the world, provided the much-needed breaks from academics.

Last but not the least, I am grateful to my parents and brother for their support throughout my life. Without them, I would not be what I am now.

Contents

1	Introduction	1
1.1	General Introduction	1
1.2	X-ray Binaries	3
1.2.1	High Mass X-ray Binary (HMXB)	4
1.2.2	Low Mass X-ray Binary (LMXB)	4
1.3	Newtonian Accretion Disk	5
1.4	Effects of Schwarzschild Space-Time	7
1.5	Plan of the Thesis	10
2	Formalism for Rapidly Rotating Neutron Stars	11
2.1	Introduction	11
2.2	Structure Calculation	13
2.3	Luminosity Calculation	20
2.4	Equation of State	23
2.5	The Results	26
2.6	Concluding Remarks	28
3	Calculation of Disk Temperature Profile	31
3.1	Introduction	31
3.2	The Effective Temperature of the Disk	33
3.2.1	Effects of General Relativity and Rotation	33
3.2.2	Disk Irradiation by the Neutron Star	35

3.3	The Results	37
3.4	Summary and Discussion	43
4	Disk Temperature Profile: Implications for Five LMXB Sources	47
4.1	Introduction	47
4.2	Procedure of Comparison with Observations	48
4.3	The Results	50
4.4	Summary and Discussion	51
5	General Relativistic Spectra of Accretion Disks around Rotating Neutron Stars	59
5.1	Introduction	59
5.2	Calculation of the Spectrum: Without Light-Bending Effect	61
5.3	Calculation of the Spectrum: With Light-Bending Effect	62
5.4	The Results	64
5.5	Conclusion	68
6	Functional Approximation of Disk Spectra	73
6.1	Introduction	73
6.2	Functional Approximation Method	74
6.3	The Results	74
6.4	Summary and Discussion	78
7	Disk Temperature Profiles for Strange Stars: A Comparison With Neutron Stars	83
7.1	Introduction	83
7.2	Equation of State	85
7.3	The Results	86
7.4	Summary and Discussion	92
8	Summary and Conclusion	99
8.1	Introduction	99

8.2	Disk Temperature Profile	102
8.3	Disk Spectrum	103
8.4	Strange Star	105
8.5	Future Prospects	106
8.6	Final Conclusion	107

Chapter 1

Introduction

1.1 General Introduction

Astronomy stepped into a new era with the discovery of discrete galactic X-ray sources (for example, Scorpius X-1) by the rocket-borne Geiger counters in 1962 (Giacconi et al. 1962). Subsequent rocket and Balloon flights confirmed this result. Before 1970, about 20 X-ray sources had been identified, with most of them believed to be galactic sources. The binary nature of these galactic X-ray sources was established (Schreier et al. 1972; Tananbaum et al. 1972) by the first astronomy satellite *Uhuru* (launched by NASA in 1970). The same satellite also discovered binary X-ray pulsars. Later X-ray and optical observations confirmed that there are two types of X-ray emitting binary systems (see for example, Bhattacharya & van den Heuvel 1991 and the references therein): (1) high mass X-ray binaries (HMXBs), with identified optical counterparts associated with very massive and luminous (late O or early B supergiants) stars, and (2) low mass X-ray binaries (LMXBs), associated with objects for which the optical counterparts, if identified, are associated with low mass (M or K spectral type) stars (see section 1.2 for discussions). Both types of X-ray emitting systems show different kinds of spectral and temporal behaviors. In our work, we are interested in LMXBs and briefly describe the major observational properties exhibited by them.

Some of the LMXBs show X-ray bursts (Grindlay et al. 1976; Belian, Conner & Evans 1976). Two types of bursts have been identified: (1) Type I: the recurring time of the burst is several hours and a distinct spectral softening occurs during burst decay (timescales of 10 sec. to a few minutes). The origin of such a burst is believed to be the thermonuclear flashes taking place on the neutron star surface (Joss 1978) and the subsequent spectral softening may be caused by the cooling of the stellar surface after the burst. The majority of the bursting sources show this type of behavior. (2) Type II: these bursts, seen for the sources 4U 1730-335 (the Rapid Burster), Cir X-1, GRO J17444-28, are repetitive and the timescale is smaller than that for type I bursts (for the Rapid

Burster, the burst interval is ~ 7 sec.). Spasmodic accretion may cause such rapid variations in X-ray intensity (Lewin et al. 1976).

Although most of the LMXBs are persistent in their X-ray luminosities, some of them show transient behavior in the timescale of days to weeks. The X-ray luminosity may vary upto 10^4 times for such a source. Such transience may be caused by an instability of the accretion disk (in section 1.2 accreion disk is defined) or of the mass transfer process (see Tanaka & Shibazaki 1996 and Campana et al. 1998 for reviews). The periodic dipping activity (Walter et al. 1982; White & Swank 1982) seen in some sources is believed to be due to the obscuration of the central accretor by a portion of the accretion disk. The partial eclipses, observed for a few X-ray sources, may be caused by partial occultation of matter at some portion of the system.

The X-ray satellite *EXOSAT* discovered time variabilities (frequency range $\sim 6 - 60$ Hz) in the X-ray intensities of several X-ray sources. As the corresponding power spectra can be fitted by broad Lorentzian profiles, such temporal behaviors are called Quasi Periodic Oscillations (QPOs). The origin of QPOs is not yet clear and there exist several models, though none of them can explain it fully. The most popular model is the beat-frequency model (Alpar & Shaham 1985), in which the QPO frequency is believed to be the difference between the (fixed) spin frequency of the neutron star and the (variable) Keplerian frequency of matter moving in the accretion disk at the Alfvén radius.

In 90's, the X-ray satellite *RXTE* discovered QPOs with very high frequencies (from a few hundred Hz to more than a kHz). These are called kHz QPOs. The origin of them is unknown, but beat-frequency model (instead of Alfvén radius, disk inner edge radius is taken for the simplest form of the model) is the most popular among all the existing models.

It has been seen that both the QPO and the kHz QPO are strongly corelated with the spectral behaviors of the sources. Such corelation can be studied very well with the help of color-color diagram (CD) and hardness-intensity diagram (HID) (see van der Klis 1995 for a description). There are six very luminous X-ray sources, that trace Z-like curves (with three branches: horizontal branch, normal branch and flaring branch) in CD and HID. These are called Z sources. On the other hand, there are several comparatively less luminous sources, which are called atoll sources. An atoll source has a clustered branch (island state) and an upwardly curved branch (banana state) in CD and HID. Most of the Z and atoll sources display QPO and kHz QPO. The position of an LMXB in CD (or HID) determines its spectral nature. This position is also strongly corelated with the nature of QPOs and kHz QPOs. Therefore the relation between the temporal and the spectral behavior can be studied using CD (and HID). For the details of this corelation, see van der Klis (1995; 2000).

A few LMXBs show regular X-ray pulsations. The frequency of such an X-ray pulsar is believed to be the rotational frequency of the central accretor (like radio pulsars). The LMXB SAX J1808.4-3658 shows milli-second X-ray pulsation, which supports the conjecture that LMXBs are progenitors of milli-second radio pulsars.

In our work, We do not try to explain the temporal behavior of the LMXBs; rather we calculate the accretion disk spectrum considering the full effect of general relativity and rapid rotation of the neutron star. In section 1.2, we briefly describe the nature of the X-ray binaries. We explain the Newtonian accretion disk in section 1.3 and mention the effect of the inclusion of Schwarzschild metric in section 1.4. In section 1.5, we describe the plan of the thesis.

1.2 X-ray Binaries

An X-ray Binary is a binary stellar system with a compact primary star (black hole, neutron star or strange star) and a secondary (or companion) star (main sequence star, blue super-giant star, red sub-giant star or white dwarf) rotating around each other. These are galactic sources that emit a substantial part of their energy in X-rays. The typical luminosities of the strongest sources among these systems are in the range $10^{34} - 10^{38}$ erg s⁻¹. The source of this energy is the gravitational energy release, as the transfer of matter occurs from the secondary to the primary. Due to the deep potential well of the compact primary, a considerable part ($\sim 20\%$ for a neutron star) of the rest mass of the transferred matter is converted to energy, which is eventually emitted in the form of X-rays (as this matter, near the compact star, is expected to be very hot: temperature $\sim 10^6$ K for neutron stars).

It is believed that there are two main reasons behind this mass transfer (Frank, King & Raine 1992): (1) the companion star may increase in radius, or the binary separation shrink, to the point where the gravitational pull of the primary star can remove the outer layer of its envelope (Roche-lobe overflow); (2) a substantial amount of mass of the secondary star may be ejected in the form of stellar wind and a part of it may be gravitationally captured by the primary.

In our work, we consider only the Roche-lobe overflow. The mechanism of such a overflow is as follows (see, for example, Kopal 1959; Tsevevich 1973; Frank et al. 1992). In a coordinate system co-rotating with the binary, there is a pear-shaped equipotential (combination of both the gravitational and the centrifugal forces) surface around each component. If one goes outwards from each of the mass centers, at a certain value of the potential, these two surfaces touch each other at the first Lagrangian point L_1 , located on the connecting line of the centers of two components. This critical equipotential surface through L_1 is called the *Roche-lobe*. When the secondary star

fills its Roche lobe, matter from its outer layer flows in a narrow jet towards the primary due to the unbalanced pressure at L_1 (where the net gravity vanishes). Due to initial angular momentum, this matter can not flow radially towards the compact star, rather it takes a circuital path and eventually forms a disk (because of angular momentum redistribution and friction among the particles). Such a disk is called an accretion disk.

X-ray binaries belong to two categories as described below. These systems, with neutron stars as the central accretors, are the most luminous galactic X-ray sources (first suggested by Zeldovich & Guseynov 1965). In our work, we consider only such systems.

1.2.1 High Mass X-ray Binary (HMXB)

These sources contain early type (massive) stars (generally, O or B type) as the companions. So the optical spectra of HMXBs are dominated by the spectra of their secondary components. We observe relatively hard X-ray spectra ($kT \gtrsim 15$ keV in exponential fit; Jones 1977) and $L_{\text{opt}}/L_X > 1$ for these systems (L_{opt} and L_X are the optical and X-ray luminosities respectively). They show regular X-ray pulsations, but no X-ray bursts, which indicates that their surface dipole field strengths are typically of the order of 10^{11} to 10^{13} Gauss (see for example, Taam & van den Heuvel 1986). HMXBs are found to be concentrated in the galactic plane. Hence they form a young stellar population (age $< 10^7$ yrs.), which is consistent with the fact that they contain early type secondary stars.

As they contain very bright secondary components, which can be easily detected, one can determine their orbital period, observing the regular X-ray eclipses. Such eclipses are very frequent in these systems. With this and the Doppler radial velocity curves of the neutron star (or pulsar) and its companion, and the light curve, the mass of each component, as well as the average radius of the companion star can be determined (Rappaport & Joss 1983; Rappaport & Joss 1984).

1.2.2 Low Mass X-ray Binary (LMXB)

These systems contain late type (low mass) companion stars, which can not be detected easily (in fact, normal companions have been detected for very few cases). So the determination of the masses of the components is not possible for most of the cases. We observe softer X-ray spectra ($kT \lesssim 10$ keV in exponential fit; van Paradijs 1989) and $L_{\text{opt}}/L_X < 0.1$ for them. LMXBs show X-ray bursts for many cases, but regular X-ray pulsations for very few cases. They concentrate in the galactic center and globular clusters. They are old systems (age $\sim (5 - 15) \times 10^9$ yrs.). The neutron stars in these systems generally have weak surface magnetic fields (Bhattacharya & van den Heuvel 1991). We study these systems in our work.

1.3 Newtonian Accretion Disk

In this section, we briefly discuss the accretion disks around neutron stars in Newtonian formalism. In many cases, the disk flow is confined very closely to the orbital plane and one can regard the disk as a two-dimensional gas flow to a first approximation. This *thin disk approximation* has proved very successful (Frank et al. 1992). The present interest in accretion disks has been developed from the encouraging results of comparison between the theory and observations of close binary systems.

A non-relativistic, incompressible fluid around an unmagnetized star should be governed by the Navier-stokes equation (see, for example, Landau & Lifshitz 1987):

$$\frac{\partial \vec{v}}{\partial t} + (\vec{v} \cdot \vec{\nabla}) \vec{v} = -\frac{1}{\rho} \vec{\nabla} P - \vec{\nabla} \Phi + \nu \nabla^2 \vec{v}. \quad (1.1)$$

Here ρ is the mass density, \vec{v} is the velocity, P is the pressure, ν is the kinematic viscosity of the fluid and Φ is the gravitational potential of the central star.

However, we directly use the laws of conservation of mass and angular momentum, to derive the basic governing equation for thin disk. We assume that the disk is Keplerian, i.e., the angular speed of a particle in the disk is

$$\Omega_K(r) = \left(\frac{GM}{r^3} \right)^{1/2} \quad (1.2)$$

where G is the gravitational constant, M is the mass of the central star and r is the radial coordinate. The corresponding linear speed is $v_\phi = r\Omega_K(r)$. In addition to v_ϕ , the gas is assumed to possess a small radial drift speed (v_r) towards the star. This is because, due to friction among the particles in the disk, most of the angular momentum is taken away by a small number of particles and most of the particles move inwards losing their angular momentum (see Frank et al. 1992 for detailed discussion). We characterize the disk by its surface density $\Sigma(r, t)$ (t is time), which is the mass per unit surface area of the disk, given by integrating the gas density ρ in the z -direction (i.e., perpendicular to the plane of the disk). Now the conservation laws for mass and angular momentum (in combination with the expression for viscous torque in the disk; see Frank et al. 1992) give

$$\frac{\partial \Sigma}{\partial t} = \frac{3}{r} \frac{\partial}{\partial r} \left\{ r^{1/2} \frac{\partial}{\partial r} (\nu \Sigma r^{1/2}) \right\} \quad (1.3)$$

as the basic equation governing the time evolution of surface density in a Keplerian disk.

As the radial structure in a thin disk changes in the timescales $\sim t_{\text{visc}} \sim r^2/\nu$, and the external conditions (for example, mass accretion rate) in many systems change on timescales longer than t_{visc} , a steady-state approximation ($\frac{\partial}{\partial t} = 0$) for the disk should be more or less valid. Therefore from the mass conservation law, we get $r\Sigma v_r = \text{constant}$, i.e., if \dot{M} is the (constant) mass accretion rate, then we get

$$\dot{M} = 2\pi r\Sigma(-v_r) \quad (1.4)$$

since $v_r < 0$, as the particles move inwards.

The rotation rate of the star is expected to be slower than the break-up speed at its equator, i.e.,

$$\Omega_* < \Omega_K(R) \quad (1.5)$$

where Ω_* is the stellar rotation rate and R is the radius of the star. Therefore, very near the surface of the star the angular speed of the disk particles should decrease and attain the value Ω_* at $r = R$. This small region, in which angular speed decreases, is called the boundary layer. The width (b) of the boundary layer is much smaller than R , as shown in Frank et al. (1992).

Now combining Eq. (1.4), the law of conservation of angular momentum (with the condition $\frac{\partial}{\partial t} = 0$) and the condition $b \ll R$, one can derive the equation

$$\nu\Sigma = \frac{\dot{M}}{3\pi} \left\{ 1 - \left(\frac{R}{r} \right)^{1/2} \right\} \quad (1.6)$$

using which we get the viscous dissipation per unit disk face area as (see Frank et al. 1992 for derivation)

$$F(r) = \frac{3GM\dot{M}}{8\pi r^3} \left\{ 1 - \left(\frac{R}{r} \right)^{1/2} \right\}. \quad (1.7)$$

Therefore, the disk energy flux comes out to be independent of viscosity. This is a very important result, as we can try to understand the values of M , \dot{M} and R for a particular source by fitting the observational data, without having much idea about the physical nature of the disk viscosity.

Energy comes out also from the thin boundary layer (around the equator of the neutron star), as the matter hits the stellar surface. The source of both boundary layer luminosity (L_{BL}) and disk luminosity (L_{D}) is the gravitational potential energy release. It is easy to see that, for Newtonian case,

$$L_{\text{BL}} = L_{\text{D}} = \frac{GM\dot{M}}{2R}. \quad (1.8)$$

It is very important to calculate the disk temperature profile, as the disk spectrum can be calculated from it. Fitting this theoretical spectrum to the observed one for a source, one can hope to constrain the values of its parameters. If the disk is optically thick in the z -direction, each element of it is expected to radiate roughly as a blackbody. The temperature profile ($T(r)$) of such a blackbody disk is given by

$$\sigma T^4(r) = F(r) \quad (1.9)$$

where σ is the Stefan-Boltzmann constant. Now using Eq. (1.7), we get

$$T(r) = \left[\frac{3GM\dot{M}}{8\pi r^3 \sigma} \left\{ 1 - \left(\frac{R}{r} \right)^{1/2} \right\} \right]^{1/4}. \quad (1.10)$$

In the next section, we will see how this expression is modified if we consider the general relativistic formalism.

1.4 Effects of Schwarzschild Space-Time

Most of the X-rays from an LMXB come from a region which is very close to the compact star. The gravity is so strong in this region that Newtonian theory does not provide an adequate description. The correct theory that can describe the motion of the particles near the compact star is expected to be general relativity. In this section, we briefly describe the effects of this theory for non-rotating neutron stars (i.e., the Schwarzschild space-time). General relativity introduces some new effects, not found in the Newtonian framework. One of these is the existence of an innermost stable circular orbit (ISCO), that we discuss below.

For a non-rotating neutron star the configuration is spherically symmetric and the corresponding space-time geometry (outside the star) is described by the Schwarzschild metric (see, for example, Misner, Thorne & Wheeler 1973):

$$\begin{aligned}
ds^2 &= g_{\lambda\beta} dx^\lambda dx^\beta \quad (\lambda, \beta = 0, 1, 2, 3) \\
&= -\left(1 - \frac{2GM}{c^2 r}\right) dt^2 + \left(1 - \frac{2GM}{c^2 r}\right)^{-1} dr^2 + r^2(d\theta^2 + \sin^2 \theta d\phi^2)
\end{aligned} \tag{1.11}$$

where we have used the $(- + + +)$ convention. In the above metric, r is the radial coordinate, while θ and ϕ are the polar and azimuthal coordinates respectively. The quantity M is the mass of the star.

It is to be noted that the structure of a neutron star can not be calculated using Newtonian theory, as the gravity is too strong inside it. Therefore, general relativity must be explicitly included in constraining the equation of state of the neutron star (discussed in latter chapters). We can formulate the structure equations for a non-rotating neutron star using the perfect fluid assumption (for the stellar material) and Einstein's field equations. These are

$$\frac{dP}{dr} = -G \frac{(m + 4\pi r^3 P/c^2)(\rho + P/c^2)}{r^2 \{1 - (2Gm/c^2 r)\}} \tag{1.12}$$

$$\frac{dm}{dr} = 4\pi r^2 \rho \tag{1.13}$$

where P , ρ and m are the pressure, mass-energy density of the system and the mass contained in a radius r respectively and all of them are functions of r . Here we use the line element (Misner, Thorne & Wheeler 1973)

$$ds^2 = -e^{2\Phi} dt^2 + \left(1 - \frac{2Gm}{c^2 r}\right)^{-1} dr^2 + r^2(d\theta^2 + \sin^2 \theta d\phi^2) \tag{1.14}$$

with the source function Φ given by

$$\frac{d\Phi}{dr} = \frac{m + 4\pi r^3 P/c^2}{r \{r - (2Gm/c^2)\}}. \tag{1.15}$$

For $r \geq R$ (R is the radius of the star), the pressure vanishes and hence the line element (1.14) becomes identical with the Schwarzschild line element (1.11). Eq. (1.12) is the Tolman-Oppenheimer-Volkoff (TOV) equation (Oppenheimer & Volkoff 1939). Eqs. (1.12) and (1.13) can be solved to

get the structure parameters of the neutron star if its equation of state (i.e., P as a function of ρ) is known. As the neutron star is degenerate (except a thin outer shell), the temperature does not enter in the equation of state.

In the Schwarzschild metric, the specific energy \tilde{E} and the specific angular momentum l are constants of motion (see Shapiro & Teukolsky 1983). The equations of motion of a particle (confined to the equatorial plane) in this metric are (Thampan 1999):

$$\frac{dt}{d\tau} = \tilde{E} \left(1 - \frac{r_g}{r}\right)^{-1} \quad (1.16)$$

$$\frac{d\phi}{d\tau} = \frac{l}{r^2} \quad (1.17)$$

$$\frac{dr}{d\tau} = \tilde{E}^2 - \tilde{V}^2 \quad (1.18)$$

where we have used geometric units $c = G = 1$. In the above equations, r_g is the Schwarzschild radius ($2GM/c^2$), τ represents the proper time and \tilde{V} is the effective potential given by

$$\tilde{V}^2 = \left(1 - \frac{r_g}{r}\right) \left(1 + \frac{l^2}{r^2}\right). \quad (1.19)$$

The conditions for circular orbits and the extremum of energy are $\tilde{E}^2 = \tilde{V}^2$ and $\tilde{V}_{,r} = 0$ respectively. The radius (r_{orb}) of the ISCO (as mentioned earlier) can be calculated from the equation $\tilde{V}_{,rr} = 0$. Here a comma followed by a variable as subscript to a quantity, represents the derivative of the quantity with respect to the variable. There can be no stable circular orbit inside the ISCO. Therefore the accretion disk can exist upto the ISCO and then the matter quickly (i.e., the radial speed increases enormously) falls on the surface of the central star. However, if the stellar radius is greater than the radius of the ISCO, the disk will be extended upto the surface of the star. Therefore, the radius (r_{in}) of the inner edge of the disk is R (r_{orb}) for $R > r_{\text{orb}}$ ($r_{\text{orb}} > R$). It is to be noted that throughout our work, we assume that the magnetic field of the neutron star is too weak to affect the accretion flow.

The specific disk luminosity (E_{D}) is given by the energy difference between a particle (of unit mass) at infinity and the same particle at $r = r_{\text{in}}$. The specific boundary layer luminosity (E_{BL})

is defined by the same kind of energy difference, but with the particle positions $r = r_{\text{in}}$ and $r = R$ (i.e., the particle sitting on the surface of the star).

For Schwarzschild metric, the energy flux of the disk is given by (Yamada & Fukue 1993; Novikov & Thorne 1973)

$$F(r) = \frac{3\mu\dot{M}}{8\pi r^{\frac{5}{2}}(r - 3\mu)} \cdot \left[\sqrt{r} - \sqrt{r_{\text{in}}} + \frac{\sqrt{3\mu}}{2} \cdot \ln \frac{(\sqrt{r} + \sqrt{3\mu})(\sqrt{r_{\text{in}}} - \sqrt{3\mu})}{(\sqrt{r} - \sqrt{3\mu})(\sqrt{r_{\text{in}}} + \sqrt{3\mu})} \right] \quad (1.20)$$

With $\mu = \frac{GM}{c^2}$ and $c = 1$. The disk temperature profile is then calculated from Eq. (1.9).

1.5 Plan of the Thesis

In this thesis, we calculate the temperature profile and the spectrum of an accretion disk around a rapidly rotating neutron star. In Chapter 2, we give the formalism for the structure calculation of a fast rotating star. We also describe different sequences possible for such a star. We also give the details of luminosity calculation and mention the neutron star equations of state used in this work.

In Chapter 3, we calculate the disk temperature profiles for different values of stellar rotation rate and for all the chosen equations of state. We compare these results with those for Newtonian and Schwarzschild cases and point out the importance of incorporating the effects of general relativity and rapid rotation in the accretion disk calculations.

We compare the theoretical results (calculated in Chapter 3) with the observational (*EXOSAT*) data for five LMXB sources and constrain several properties for these systems in Chapter 4. We also discuss possible constraints on the neutron star equation of state.

In Chapter 5, we compute the general relativistic spectrum of an accretion disk around a rotating neutron star. We show that the effect of light-bending is very important at higher energies.

We fit the calculated (in Chapter 5) spectrum with an analytical function in Chapter 6. Here we suggest a method to distinguish between a Newtonian spectrum and a general relativistic spectrum observationally.

It has been proposed that the central accretors of at least some of the LMXBs are strange stars (and not neutron stars). In order to try to answer this question, in Chapter 7, we calculate the values of several properties (including the disk temperature profile) of a rotating strange star and compare them with those of a rotating neutron star.

In Chapter 8, we give a summary of our work and discuss the future prospects. We also mention the main conclusions of the thesis.

Chapter 2

Formalism for Rapidly Rotating Neutron Stars

2.1 Introduction

The necessary condition for disk accretion is that the accreted matter must have intrinsic angular momentum. Because of this property, matter coming out of the companion star can not fall on the surface of the neutron star radially, but moves almost in circular orbit and forms a disk. The specific angular momentum of this matter is much higher than that of a neutron star. As a result, when it hits the star, the stellar angular momentum increases, making the star rotate faster in general. Therefore accreting neutron stars are expected to be rapidly rotating due to such accretion induced angular momentum transfer. This was the reason that the LMXBs were speculated to be the progenitors of millisecond radio pulsars for long time (Bhattacharya & van den Heuvel 1991). Recently such speculation has been confirmed with the discovery of a millisecond pulsar (SAX J1808.4–3658) in an LMXB (Wijnands & van der Klis 1998). SAX J1808.4–3658 shows periodic pulsations ($P = 2.49$ ms) in X-rays, which proves that accretion can actually spin up the central accretor very effectively. We also observe kHz QPO and Burst Oscillation (van der Klis 2000). The frequency separation (~ 300 Hz) between the two simultaneously observed peak of kHz QPO is equal to the rotational frequency of the central star according to the beat-frequency model. The Burst Oscillation frequency is also believed to be close to (or integer multiple of) the stellar angular frequency (van der Klis 2000). These indicate the rapid rotation of the accreting neutron star.

It is therefore essential to construct equilibrium sequences for rapidly rotating neutron stars, considering the full effect of general relativity. The Schwarzschild metric is no longer valid even outside a rotating neutron star, as the relativistic effect of dragging of inertial frames in the vicinity

of the star will be important. This will affect the luminosity and the spectra of the accretion disk. Therefore to model the observed spectra more accurately, we need to compute the metric coefficients around rapidly rotating neutron stars.

Relativistic models of slowly rotating neutron stars were constructed by Hartle & Thorne (1968). Their formalism is valid for strong gravitational fields, but only in the limit of slow rotation (neglects terms higher than $O(\Omega_*^2/\Omega_{\text{ms}}^2)$) compared to the critical angular speed for centrifugal break-up (Ω_{ms}). Similar calculations, using the same formalism, were performed by Datta & Ray (1983), to construct models based on a variety of proposed equations of state. An extensive study of the properties of these models has been made by Datta, Kapoor & Ray (see, for example, Datta 1988 and references therein). For a description of the structure calculation of slowly rotating neutron stars, see Thampan (1999).

A formalism, appropriate for a rapidly rotating neutron star, should be exact in its treatment of Ω_* . The metric coefficients for such models are to be calculated numerically, unlike the case of slowly rotating models, where the metric coefficients have analytic expressions. The exact models are the solutions of Einstein's equations for the stationary gravitational field in axisymmetry, coupled to the equation of hydrostatic equilibrium. Such models have previously been constructed by several authors, including Bonazzola & Schneider (1974), Butterworth (1976) (for polytropic EOS) and Friedman, Ipser & Parker (1986) (for realistic EOS). An alternative approach using spectral methods was developed by Bonazzola et al. (1993) and used for many realistic EOS by Salgado et al. (1994a; 1994b). However, we follow the procedure used by Cook, Shapiro & Teukolsky (1994), based on a formalism due to Komatsu, Eriguchi & Hachisu (1989). For a comparison of different formalisms, see Stergioulas (1998).

For our preliminary study, we calculate different sequences. These are mainly of two types: evolutionary sequence and limit sequence. We call sequences along which the rest mass M_0 is held fixed evolutionary sequences. An isolated neutron star is expected to evolve along such a sequence, as it slowly loses energy and angular momentum via, for example, electromagnetic or gravitational radiation. The set of all evolutionary sequences is naturally divided into two groups: the normal sequences and the supramassive sequences. Normal evolutionary sequences are those that terminate at one end with a nonrotating, spherically symmetric solution. Supramassive sequences do not contain such static solution.

The set of equilibrium solutions for a given EOS forms a two parameter family. The boundary of the set of stable equilibrium solutions is formed by the four limits. The first limit is the static limit, where $\Omega_* \rightarrow 0$ and total angular momentum $J \rightarrow 0$. Models on the static limit sequence are solutions of the TOV equations for spherically symmetric models, described in Chapter 1.

The second limit is the mass–shed limit, which is reached when the gravitational attraction at the stellar equator is not sufficient to keep matter bound to the surface. For the case of general differential rotation, mass–shed limit occurs when

$$\frac{1}{2} \frac{\partial}{\partial r} (\rho + \gamma) - \frac{\tilde{v}}{1 - \tilde{v}^2} \frac{\partial \tilde{v}}{\partial r} + F(\Omega_*) \frac{\partial \Omega_*}{\partial r} = 0 \quad (2.1)$$

at the equator (Cook et al. 1994). Here the relation $F(\Omega_*) = u^t u_\phi$ specifies the rotation law, \tilde{v} is the proper velocity of matter at the equator with respect to a zero-angular-momentum-observer (ZAMO) and ρ & γ are the metric coefficients (see section 2).

The third limit is the stability limit, where an equilibrium solution is marginally stable to quasi–radial perturbations. The stability limit sequence begins at the maximum–mass point on the static limit sequence and usually terminates near the maximum–mass point on the mass–shed limit sequence. The intermediate points lie on supramassive evolutionary sequences where the stability condition

$$\left(\frac{\partial J}{\partial \epsilon_c} \right)_{M_0} < 0 \quad (2.2)$$

is marginally satisfied (Cook et al. 1994). Here ϵ_c is the central total energy density.

Finally, there is the low–mass limit, below which a neutron star cannot form. However, we have not attempted to determine this limit, as it is of minimal importance.

In our work, we, in general, choose gravitational mass (M) and Ω_* as the independent parameters for a given EOS. The reason is that these are the quantities that can be observationally measured. Therefore we construct gravitational mass sequences (i.e., M is kept constant) and study the values of different quantities for equilibrium configurations.

In section 2.2 and 2.3, we describe the procedure for structure calculation of a rapidly rotating neutron star, considering the full effect of general relativity and the corresponding luminosity–calculation–procedure respectively. A description of equations of state is given in section 2.4. We show our results in section 2.5 and give concluding remarks in section 2.6.

2.2 Structure Calculation

We assume that the space–time in and around a rotating neutron star is stationary, axisymmetric, asymptotically flat and reflection–symmetric (about the equatorial plane). The metric may be written in the form (Bardeen 1970)

$$\begin{aligned}
ds^2 &= g_{\lambda\beta} dx^\lambda dx^\beta \quad (\lambda, \beta = 0, 1, 2, 3) \\
&= -e^{\gamma+\rho} dt^2 + e^{2\alpha} (d\bar{r}^2 + \bar{r}^2 d\theta^2) + e^{\gamma-\rho} \bar{r}^2 \sin^2\theta (d\phi - \omega dt)^2
\end{aligned} \tag{2.3}$$

where the metric potentials γ , ρ , α , and the angular speed (ω) of zero-angular-momentum-observer (ZAMO) with respect to infinity, are all functions of the quasi-isotropic radial coordinate (\bar{r}) and polar angle (θ). \bar{r} is related to the Schwarzschild-like radial coordinate (r) through the equation $r = \bar{r}e^{(\gamma-\rho)/2}$ (see Misner, Thorne & Wheeler 1974). Here we use geometric units $c = G = 1$.

We assume that the matter source is a perfect fluid with a stress-energy tensor given by

$$T^{\mu\nu} = (\epsilon + P)u^\mu u^\nu + P g^{\mu\nu} \tag{2.4}$$

where ϵ is the total energy-density, P is the pressure and u^μ is the matter four-velocity, given by (Cook et al. 1994)

$$u^\mu = \frac{e^{-(\gamma+\rho)/2}}{(1 - \tilde{v}^2)^{1/2}} (1, 0, 0, \Omega_*) \tag{2.5}$$

Here $\Omega_* \equiv u^3/u^0$ is the angular speed and the proper velocity \tilde{v} of the matter, relative to ZAMO, is given by

$$\tilde{v} = (\Omega_* - \omega)\bar{r} \sin\theta e^{-\rho} \tag{2.6}$$

The tilde over a variable represents the corresponding dimensionless quantity. For example, we use $\tilde{r} \equiv \kappa^{-1/2}\bar{r}$, $\tilde{t} \equiv \kappa^{-1/2}ct$, $\tilde{\omega} \equiv \frac{1}{c}\kappa^{1/2}\omega$, $\tilde{\Omega}_* \equiv \frac{1}{c}\kappa^{1/2}\Omega_*$, $\tilde{\epsilon} \equiv \frac{G}{c^2}\kappa\epsilon$, $\tilde{P} \equiv \frac{G}{c^4}\kappa P$, $\tilde{J} \equiv \frac{G}{c^3}\kappa^{-1}J$ and $\tilde{M} \equiv \frac{G}{c^2}\kappa^{-1/2}M$, where the fundamental length scale $\kappa^{1/2}$ is given by $\kappa \equiv \frac{c^2}{G\epsilon_o}$, with $\epsilon_o = 10^{15} \text{g cm}^{-3}$.

For an axisymmetric and equatorial plane symmetric configuration, the computational domain in spherical polar coordinates covers $0 \leq r \leq \infty$ and $0 \leq \theta \leq \pi/2$. For numerical convenience, we make a change of variables ($r \rightarrow s$ and $\theta \rightarrow \mu$) given by

$$\begin{aligned}
\tilde{r} &= \tilde{r}_e \frac{s}{1-s}; \\
\theta &= \cos^{-1} \mu
\end{aligned} \tag{2.7}$$

where \bar{r}_e is the quasi-isotropic radial coordinate of the equator. It is easy to see that s and μ vary in the range $0 \leq s \leq 1$ & $0 \leq \mu \leq 1$ and at the equator $s = 0.5$.

For these variables, the Einstein field equations projected on to the frame of reference of a ZAMO yield three elliptic equations for the metric potentials ρ, γ & ω and two linear ordinary differential equations for the metric potential α (Bardeen & Wagoner 1971; Butterworth & Iperser 1976; Komatsu et al. 1989). The elliptic equations are of the form (Thampan 1999):

$$\tilde{\Delta}[\rho e^{\gamma/2}] = \tilde{S}_\rho(s, \mu) \quad (2.8)$$

$$\left(\tilde{\Delta} + \frac{(1-s)^3}{s} \frac{\partial}{\partial s} - \frac{(1-s)^2 \mu}{s^2} \frac{\partial}{\partial \mu} \right) \gamma e^{\gamma/2} = \tilde{S}_\gamma(s, \mu) \quad (2.9)$$

$$\left(\tilde{\Delta} + \frac{2(1-s)^3}{s} \frac{\partial}{\partial s} - \frac{2(1-s)^2 \mu}{s^2} \frac{\partial}{\partial \mu} \right) \hat{\omega} e^{(\gamma-\rho)/2} = \tilde{S}_{\hat{\omega}}(s, \mu) \quad (2.10)$$

where the elliptic differential operator $\tilde{\Delta}$ is given by

$$\begin{aligned} \tilde{\Delta} = & (1-s)^4 \left(\frac{\partial^2}{\partial s^2} \right) - 2(1-s)^3 \left(\frac{\partial}{\partial s} \right)^2 + \frac{2(1-s)^3}{s} \left(\frac{\partial}{\partial s} \right) \\ & + \frac{(1-s)^2(1-\mu^2)}{s^2} \left(\frac{\partial^2}{\partial \mu^2} \right) - \frac{(1-s)^2 \mu}{s^2} \left(\frac{\partial}{\partial \mu} \right) + \frac{(1-s)^2}{s^2(1-\mu^2)} \left(\frac{\partial^2}{\partial \phi^2} \right) \end{aligned} \quad (2.11)$$

The effective sources \tilde{S} 's are defined as (Cook et al. 1994)

$$\begin{aligned} \tilde{S}_\rho(s, \mu) = & e^{\gamma/2} \left[8\pi e^{2\alpha} \bar{r}_e^2 (\tilde{\epsilon} + \tilde{P}) \left(\frac{s}{1-s} \right)^2 \frac{1 + \tilde{v}^2}{1 - \tilde{v}^2} \right. \\ & + \left(\frac{s}{1-s} \right)^2 (1-\mu^2) e^{-2\rho} \{ [s(1-s)\hat{\omega}_{,s}]^2 + (1-\mu^2)\hat{\omega}_{,\mu}^2 \} \\ & + s(1-s)\gamma_{,s} - \mu\gamma_{,\mu} + \frac{\rho}{2} \left\{ 16\pi e^{2\alpha} \bar{r}_e^2 \tilde{P} \left(\frac{s}{1-s} \right)^2 \right. \\ & \left. \left. - s(1-s)\gamma_{,s} \left(\frac{s(1-s)}{2}\gamma_{,s} + 1 \right) - \gamma_{,\mu} \left(\frac{1-\mu^2}{2}\gamma_{,\mu} - \mu \right) \right\} \right] \end{aligned} \quad (2.12)$$

$$\begin{aligned} \tilde{S}_\gamma(s, \mu) &= e^{\gamma/2} \left[16\pi e^{2\alpha} \tilde{r}_e^2 \tilde{P} \left(\frac{s}{1-s} \right)^2 \right. \\ &\quad \left. + \frac{\gamma}{2} \left\{ 16\pi e^{2\alpha} \tilde{r}_e^2 \tilde{P} \left(\frac{s}{1-s} \right)^2 - \frac{s^2(1-s)^2}{2} \gamma_{,s}^2 - \frac{1-\mu^2}{2} \gamma_{,\mu}^2 \right\} \right] \end{aligned} \quad (2.13)$$

$$\begin{aligned} \tilde{S}_{\hat{\omega}}(s, \mu) &= e^{(\gamma-2\rho)/2} \left[-16\pi e^{2\alpha} \frac{(\hat{\Omega}_* - \hat{\omega})}{1-\tilde{v}^2} \tilde{r}_e^2 (\tilde{\epsilon} + \tilde{P}) \left(\frac{s}{1-s} \right)^2 \right. \\ &\quad + \hat{\omega} \left\{ -8\pi e^{2\alpha} \tilde{r}_e^2 \frac{(1+\tilde{v}^2)\tilde{\epsilon} + 2\tilde{v}^2 \tilde{P}}{1-\tilde{v}^2} \left(\frac{s}{1-s} \right)^2 \right. \\ &\quad - s(1-s) \left(2\rho_{,s} + \frac{1}{2}\gamma_{,s} \right) + \mu \left(2\rho_{,\mu} + \frac{1}{2}\gamma_{,\mu} \right) \\ &\quad + \frac{s^2(1-s)^2}{4} (4\rho_{,s}^2 - \gamma_{,s}^2) + \frac{1-\mu^2}{4} (4\rho_{,\mu}^2 - \gamma_{,\mu}^2) \\ &\quad \left. \left. - (1-\mu^2) e^{-2\rho} \left(s^4 \hat{\omega}_{,s}^2 + \frac{s^2(1-\mu^2)}{(1-s)^2} \hat{\omega}_{,\mu}^2 \right) \right\} \right] \end{aligned} \quad (2.14)$$

where

$$\begin{aligned} \hat{\omega} &\equiv \tilde{r}_e \tilde{\omega} ; \\ \hat{\Omega}_* &\equiv \tilde{r}_e \tilde{\Omega}_* \end{aligned} \quad (2.15)$$

The differential equation for α with respect to s does not provide any new information (see Butterworth & Ipson 1976). Here we use the differential equation for α with respect to μ

$$\begin{aligned} \alpha_{,\mu} &= -\frac{1}{2}(\rho_{,\mu} + \gamma_{,\mu}) - \{(1-\mu^2)[1 + s(1-s)\gamma_{,s}]^2 + [-\mu + (1-\mu^2)\gamma_{,\mu}]^2\}^{-1} \\ &\quad \times \left[\frac{1}{2} \{ s(1-s)[s(1-s)\gamma_{,s}]_{,s} + s^2(1-s)^2 \gamma_{,s}^2 - [(1-\mu^2)\gamma_{,\mu}]_{,\mu} \right. \\ &\quad - \gamma_{,\mu} [-\mu + (1-\mu^2)\gamma_{,\mu}] [-\mu + (1-\mu^2)\gamma_{,\mu}] + \frac{1}{4} [s^2(1-s)^2 (\rho_{,s} + \gamma_{,s})^2 \\ &\quad - (1-\mu^2)(\rho_{,\mu} + \gamma_{,\mu})^2] [-\mu + (1-\mu^2)\gamma_{,\mu}] - s(1-s)(1-\mu^2) \\ &\quad \times \left(\frac{1}{2}(\rho_{,s} + \gamma_{,s})(\rho_{,\mu} + \gamma_{,\mu}) + \gamma_{,s\mu} + \gamma_{,s}\gamma_{,\mu} \right) [1 + s(1-s)\gamma_{,s}] \\ &\quad \left. + s(1-s)\mu\gamma_{,s}[1 + s(1-s)\gamma_{,s}] + \frac{1}{4}(1-\mu^2)e^{-2\rho} \right. \\ &\quad \left. \times \left\{ 2\frac{s^3}{1-s}(1-\mu^2)\hat{\omega}_{,s}\hat{\omega}_{,\mu}[1 + s(1-s)\gamma_{,s}] \right. \right. \end{aligned}$$

$$-\left\{s^4\hat{\omega}_{,s}^2 - \frac{s^2}{(1-s)^2}(1-\mu^2)\hat{\omega}_{,s}^2\right\}[-\mu + (1-\mu^2)\gamma_{,\mu}] \quad (2.16)$$

with the initial condition that $\alpha = (\gamma - \rho)/2$ at $\mu = 1$.

In the formalism given by Komatsu et al. (1989), the elliptical differential equations are converted to integral equations (so that the boundary conditions can be handled easily) using Green's function approach. Therefore, the three metric potentials ρ, γ & ω can be written as

$$\begin{aligned} \rho(s, \mu) = & -e^{-\gamma/2} \sum_{n=0}^{\infty} P_{2n}(\mu) \left[\left(\frac{1-s}{s} \right)^{2n+1} \int_0^s \frac{ds' s'^{2n}}{(1-s')^{2n+2}} \int_0^1 d\mu' P_{2n}(\mu') \tilde{S}_\rho(s', \mu') \right. \\ & \left. + \left(\frac{s}{1-s} \right)^{2n} \int_s^1 \frac{ds' (1-s')^{2n-1}}{s'^{2n+1}} \int_0^1 d\mu' P_{2n}(\mu') \tilde{S}_\rho(s', \mu') \right] \quad (2.17) \end{aligned}$$

$$\begin{aligned} \gamma(s, \mu) = & -\frac{2e^{-\gamma/2}}{\pi} \sum_{n=1}^{\infty} \frac{\sin[(2n-1)\theta]}{(2n-1)\sin\theta} \left[\left(\frac{1-s}{s} \right)^{2n} \right. \\ & \times \int_0^s \frac{ds' s'^{2n-1}}{(1-s')^{2n+1}} \int_0^1 d\mu' \sin[(2n-1)\theta'] \tilde{S}_\gamma(s', \mu') + \left(\frac{s}{1-s} \right)^{2n-2} \\ & \left. \times \int_s^1 \frac{ds' (1-s')^{2n-3}}{s'^{2n-1}} \int_0^1 d\mu' \sin[(2n-1)\theta'] \tilde{S}_\gamma(s', \mu') \right] \quad (2.18) \end{aligned}$$

$$\begin{aligned} \hat{\omega}(s, \mu) = & -e^{(2\rho-\gamma)/2} \sum_{n=1}^{\infty} \frac{P_{2n-1}^1(\mu)}{2n(2n-1)\sin\theta} \left[\left(\frac{1-s}{s} \right)^{2n+1} \right. \\ & \times \int_0^s \frac{ds' s'^{2n}}{(1-s')^{2n+2}} \int_0^1 d\mu' \sin\theta' P_{2n-1}^1(\mu') \tilde{S}_\omega(s', \mu') + \left(\frac{s}{1-s} \right)^{2n-2} \\ & \left. \times \int_s^1 \frac{ds' (1-s')^{2n-3}}{s'^{2n-1}} \int_0^1 d\mu' \sin\theta' P_{2n-1}^1(\mu') \tilde{S}_\omega(s', \mu') \right] \quad (2.19) \end{aligned}$$

where $P_n(\mu)$ are the Legendre polynomials, $P_n^m(\mu)$ are the associated Legendre polynomials and $\sin(n\theta)$ is a function of μ through $\theta = \cos^{-1}\mu$.

The equation of hydrostatic equilibrium for a barytropic fluid is

$$h(\tilde{P}) - h_p \equiv \int_{\tilde{P}_p}^{\tilde{P}} \frac{d\tilde{P}}{\tilde{\epsilon} + \tilde{P}} = \ln u^t - \ln u_p^t - \int_{\tilde{\Omega}_{*,c}}^{\tilde{\Omega}_*} F(\tilde{\Omega}_*) d\tilde{\Omega}_* \quad (2.20)$$

where $h(\tilde{P})$ is the dimensionless specific enthalpy as a function of pressure. \tilde{P}_p, u_p^t and h_p are the dimensionless values of pressure, t-component of the four-velocity and the specific enthalpy at the

pole. $\tilde{\Omega}_{*,c}$ is the (dimensionless) central value of the angular speed, which on the rotation axis is constant and equal to its value at the pole. $F(\tilde{\Omega}_*) = u^t u_\phi$ is obtained from an integrability condition on the equation of hydrostatic equilibrium. Choosing the form of this function fixes the rotation law for the matter. Following Komatsu et al. (1989), we set it to

$$F(\tilde{\Omega}_*) = A^2(\tilde{\Omega}_{*,c} - \tilde{\Omega}_*) \quad (2.21)$$

where A is a rotation constant such that rigid rotation is achieved in the limit $A \rightarrow \infty$. An appropriately chosen value of h_p defines the surface of the star.

Integrating Eq. (2.20), we obtain

$$h(\tilde{P}) - h_p = \frac{1}{2}[\gamma_p + \rho_p - \gamma - \rho - \ln(1 - \tilde{v}^2) + A^2(\tilde{\Omega}_* - \tilde{\Omega}_{*,c})^2] \quad (2.22)$$

where γ_p and ρ_p are the values of the metric potentials at the pole. Therefore for the center and the equator of a rigidly rotating neutron star, we get

$$h(\tilde{P}_c) - h_p - \frac{1}{2}[\gamma_p + \rho_p - \gamma_c - \rho_c] = 0 \quad (2.23)$$

and

$$(\gamma_p + \rho_p - \gamma_e - \rho_e) - \ln[1 - (\tilde{\Omega}_{*,e} - \tilde{\omega}_e)^2 \tilde{r}_e^2 e^{-2\rho_e}] = 0 \quad (2.24)$$

where the subscripts p, e and c denote the values at the pole, equator and center respectively.

We follow the formalism of Komatsu et al. (1989) to compute the equilibrium configurations of a rapidly rotating neutron star. For a given equation of state (EOS), we take the maximum energy density ϵ_c and the ratio (\tilde{r}_p/\tilde{r}_e) of the coordinate radii at the pole and equator as the inputs. An equilibrium solution for given values of the configuration parameters is obtained iteratively in the following way. Let \tilde{r}'_e and the metric potentials $\rho', \gamma' & \alpha'$ be values of the current approximate solution. Then $\rho', \gamma' & \alpha'$ are first scaled (divided) by $(\tilde{r}'_e)^2$ to obtain $\hat{\rho}, \hat{\gamma} & \hat{\alpha}$. A new value for \tilde{r}_e

$$\tilde{r}_e^2 = \frac{2[h(\tilde{P}(\tilde{\epsilon}_c)) - h_p]}{\hat{\gamma}_p + \hat{\rho}_p - \hat{\gamma}_c - \hat{\rho}_c} \quad (2.25)$$

is obtained using Eq. (2.23). Using Eq. (2.24), we compute the value of $\hat{\Omega}_{*,c}$ as

$$\hat{\Omega}_{*,c} = \hat{\omega}_e + e^{\rho_e} [1 - e^{(\gamma_p + \rho_p - \gamma_e - \rho_e)}]^{1/2} \quad (2.26)$$

Now $\hat{\rho}$, $\hat{\gamma}$ & $\hat{\alpha}$ are rescaled (multiplied) by the new value of \tilde{r}_e^2 . Using these values, we solve Eq. (2.23) to obtain the new matter–energy distribution, namely $\tilde{\epsilon}$, \tilde{P} , \tilde{v} etc. Finally, Eqs. (2.16)–(2.19) are solved for the new values of the metric potentials. These steps are repeated until the value of \tilde{r}_e converges to within a tolerance of 10^{-5} . For a detailed description of the numerical procedure, see Cook et al. (1994); Datta et al. (1998) and Thampan (1999).

Once \tilde{r}_e converges, the metric potentials ρ , γ , $\hat{\omega}$ and α together with the density ($\tilde{\epsilon}$) and pressure (\tilde{P}) profiles can be used to compute the structure parameters with the following formulae (Cook et al. 1994). The total mass M is

$$M = \frac{4\pi\kappa^{1/2}c^2\tilde{r}_e^3}{G} \int_0^1 \frac{s^2 ds}{(1-s)^4} \int_0^1 d\mu e^{2\alpha+\gamma} \times \left\{ \frac{\tilde{\epsilon} + \tilde{P}}{1 - \tilde{v}^2} \left[1 + \tilde{v}^2 + \frac{2s\tilde{v}}{1-s} (1 - \mu^2)^{1/2} \hat{\omega} e^{-\rho} \right] + 2\tilde{P} \right\} \quad (2.27)$$

The total rest (baryonic) mass M_0 of the system is given by

$$M_0 = \frac{4\pi\kappa^{1/2}m_B c^2 \tilde{r}_e^3}{G} \int_0^1 \frac{s^2 ds}{(1-s)^4} \int_0^1 d\mu e^{2\alpha+(\gamma-\rho)/2} \frac{\tilde{n}}{(1-\tilde{v}^2)^{1/2}} \quad (2.28)$$

where \tilde{n} is the dimensionless baryonic number density and m_B is the mass per baryon. The total proper mass M_p of the system represents the energy stored in the configuration excluding gravitational potential energy and rotational kinetic energy. It is defined as

$$M_p = \frac{4\pi\kappa^{1/2}c^2\tilde{r}_e^3}{G} \int_0^1 \frac{s^2 ds}{(1-s)^4} \int_0^1 d\mu e^{2\alpha+(\gamma-\rho)/2} \frac{\tilde{\epsilon} + \tilde{P}}{(1-\tilde{v}^2)^{1/2}} \quad (2.29)$$

The total angular momentum J of the system is given by

$$J = \frac{4\pi\kappa c^3 \tilde{r}_e^4}{G} \int_0^1 \frac{s^3 ds}{(1-s)^5} \int_0^1 d\mu (1 - \mu^2)^{1/2} e^{2\alpha+\gamma-\rho} (\tilde{\epsilon} + \tilde{P}) \frac{\tilde{v}}{1 - \tilde{v}^2} \quad (2.30)$$

The moment of inertia I is obtained by the prescription

$$I = \frac{J}{\Omega_*} \quad (2.31)$$

The total rotational kinetic energy T of the system is defined by

$$T = \frac{2\pi\kappa^{1/2}c^2\tilde{r}_e^3}{G} \int_0^1 \frac{s^3 ds}{(1-s)^5} \int_0^1 d\mu (1-\mu^2)^{1/2} e^{2\alpha+\gamma-\rho} (\tilde{\epsilon} + \tilde{P}) \frac{\tilde{v}\hat{\Omega}_*}{1-\tilde{v}^2} \quad (2.32)$$

Then the gravitational binding energy W of the star is given by

$$W = M_p + T - M \quad (2.33)$$

The circumferential radius R at the equator is defined by

$$R = \kappa^{1/2}\tilde{r}_e e^{(\gamma_e-\rho_e)/2} \quad (2.34)$$

where the subscript ‘e’ denotes evaluation at the equator.

2.3 Luminosity Calculation

We calculate the luminosities of the accretion disk and the boundary layer using the test particle approach, i.e., we determine the amount of gravitational energy release by a test particle, as it spirals in. Since the chosen metric (given by Eq. 2.3) is stationary and axisymmetric, the energy and angular momentum of this particle are constants of motion. As we consider a geometrically thin disk, the particle is always confined to the equatorial plane. Then using the standard Lagrangian technique, the equations of motion of the particle can be written as (Thampan & Datta 1998)

$$\dot{t} \equiv \frac{dt}{d\tau} = e^{-(\gamma+\rho)}(\tilde{E} - \omega l) \quad (2.35)$$

$$\dot{\phi} \equiv \frac{d\phi}{d\tau} \equiv \Omega_{\text{tp}} \dot{t} = e^{-(\gamma+\rho)}\omega(\tilde{E} - \omega l) + \frac{l}{\tilde{r}^2 e^{(\gamma-\rho)}} \quad (2.36)$$

$$\dot{\bar{r}}^2 \equiv e^{2\alpha+\gamma+\rho} \left(\frac{d\bar{r}}{d\tau} \right)^2 = \tilde{E}^2 - \tilde{V}^2 \quad (2.37)$$

Here τ is the proper time, Ω_{tp} , \tilde{E} and l are the angular speed, specific energy and specific angular momentum of the test particle respectively and \tilde{V} is the effective potential given by

$$\tilde{V}^2 = e^{\gamma+\rho} \left[1 + \frac{l^2/\bar{r}^2}{e^{\gamma-\rho}} \right] + 2\omega\tilde{E}l - \omega^2 l^2 \quad (2.38)$$

The conditions for circular orbits, extremum of energy and minimum of energy are respectively:

$$\tilde{E}^2 = \tilde{V}^2 \quad (2.39)$$

$$\tilde{V}_{,\bar{r}} = 0 \quad (2.40)$$

$$\tilde{V}_{,\bar{r}\bar{r}} > 0 \quad (2.41)$$

For marginally stable orbits,

$$\tilde{V}_{,\bar{r}\bar{r}} = 0 \quad (2.42)$$

In our notation, a comma followed by one ‘ \bar{r} ’ represents a first order partial derivative with respect to \bar{r} and so on.

Using Eqs. (2.35), (2.36) and (2.39), the condition for circular orbits can be written as

$$\tilde{E} - \omega l = \frac{e^{(\gamma+\rho)/2}}{\sqrt{1 - \tilde{v}_{\text{tp}}^2}} \quad (2.43)$$

$$l = \frac{\tilde{v}_{\text{tp}} \bar{r} e^{(\gamma-\rho)/2}}{\sqrt{1 - \tilde{v}_{\text{tp}}^2}} \quad (2.44)$$

where v_{tp} , the proper velocity (in the equatorial plane) of the test particle relative to ZAMO, is given by

$$\tilde{v}_{\text{tp}} = (\Omega_{\text{tp}} - \omega) \bar{r} e^{-\rho} \quad (2.45)$$

Conditions (2.40) and (2.42) yield respectively,

$$\tilde{v}_{\text{tp}} = \frac{e^{-\rho} \bar{r}^2 \omega_{,\bar{r}} \pm [e^{-2\rho} \bar{r}^4 \omega_{,\bar{r}}^2 + 2\bar{r}(\gamma_{,\bar{r}} + \rho_{,\bar{r}}) + \bar{r}^2(\gamma_{,\bar{r}}^2 - \rho_{,\bar{r}}^2)]^{1/2}}{2 + \bar{r}(\gamma_{,\bar{r}} - \rho_{,\bar{r}})} \quad (2.46)$$

$$\begin{aligned} \tilde{V}_{,\bar{r}\bar{r}} \equiv & 2 \left[\frac{\bar{r}}{4} (\rho_{,\bar{r}}^2 - \gamma_{,\bar{r}}^2) - \frac{1}{2} e^{-2\rho} \omega_{,\bar{r}}^2 \bar{r}^3 - \rho_{,\bar{r}} + \frac{1}{\bar{r}} \right] \tilde{v}_{\text{tp}}^2 \\ & + [2 + \bar{r}(\gamma_{,\bar{r}} - \rho_{,\bar{r}})] \tilde{v}_{\text{tp}} \tilde{v}_{\text{tp},\bar{r}} - e^{-\rho} \omega_{,\bar{r}} \bar{r} \tilde{v}_{\text{tp}} \\ & + \frac{\bar{r}}{2} (\gamma_{,\bar{r}}^2 - \rho_{,\bar{r}}^2) - e^{-\rho} \bar{r}^2 \omega_{,\bar{r}} \tilde{v}_{\text{tp},\bar{r}} = 0 \end{aligned} \quad (2.47)$$

where we have made use of Eq. (2.46) and its derivative with respect to \bar{r} in order to eliminate the second order derivatives in Eq. (2.47). The zero of $\tilde{V}_{,\bar{r}\bar{r}}$ gives the radius (r_{orb}) of the innermost stable circular orbit (ISCO) and the corresponding \tilde{v}_{tp} yields \tilde{E} and l . In Eq. (2.46), the positive sign refers to the co-rotating particles and the negative sign to the counter-rotating particles. In our work we consider only the co-rotation case.

In a circular orbit, the Keplerian angular speed of the test particle is denoted by Ω_{K} . Using Eq. (2.45), we get the Ω_{K} profile as

$$\Omega_{\text{K}}(\bar{r}) = e^{\rho(\bar{r})} \frac{\tilde{v}_{\text{tp}}(\bar{r})}{\bar{r}} + \omega(\bar{r}) \quad (2.48)$$

where \tilde{v}_{tp} is given by Eq. (2.46). The value of Ω_{K} in an orbit at the surface of the neutron star puts a firm upper limit on the angular speed the star can attain (Friedman et al. 1986) and hence the boundary layer luminosity, when the star attains this maximum Ω_* , should be zero (Sunyaev & Shakura 1986).

Depending on the chosen EOS and the values of M and Ω_* , the equatorial radius (R) of the neutron star can be greater than or less than r_{orb} . The accretion luminosities are different for these two cases (Kluźniak & Wagoner 1985; Sunyaev & Shakura 1986; Datta et al. 1995). These quantities can be calculated in the following way.

For $R > r_{\text{orb}}$, the disk extends upto the surface of the weak magnetic field neutron star. The energy of a test particle at infinite distance from the star is equal to its rest mass m_0 . Now the specific disk luminosity (E_{D}) is equal to the gravitational energy release by the particle in the unit of m_0 . Therefore

$$E_{\text{D}} = 1 - \tilde{E}_{\text{K}}(r = R) \quad (2.49)$$

where $E_K(r = R)$ is the specific energy of the particle in Keplerian orbit at the surface, obtained by solving Eq. (2.43), (2.44) and (2.46).

The specific boundary layer luminosity (E_{BL}) is equal to the energy loss (in the unit of m_0) by the particle in the boundary layer (a very narrow gap near the neutron star surface). Therefore

$$E_{\text{BL}} = \tilde{E}_K(r = R) - \tilde{E}_0 \quad (2.50)$$

where \tilde{E}_0 is the energy of the particle ‘at rest’ on the stellar surface (the particle will be moving with the velocity $\tilde{v}_{\text{tp}} = \tilde{v}_*$ of the stellar fluid at the surface, where \tilde{v}_* is obtained by substituting into Eq. (2.6) all the relevant parameters for $r = R$) and is calculated by solving Eqs. (2.43) and (2.44) for \tilde{E} at $r = R$ and $\tilde{v}_{\text{tp}} = \tilde{v}_*$.

For $R < r_{\text{orb}}$, the accretion disk does not touch the surface of the star. The specific disk luminosity is given by

$$E_{\text{D}} = 1 - \tilde{E}_{\text{orb}} \quad (2.51)$$

Consequently the specific boundary layer luminosity is

$$E_{\text{BL}} = \tilde{E}_{\text{orb}} - \tilde{E}_0 \quad (2.52)$$

Here \tilde{E}_{orb} is the specific energy of the particle in ISCO, calculated using the Eqs. (2.43), (2.44) and (2.46) for $r = r_{\text{orb}}$.

2.4 Equation of State

For calculating the structure of a neutron star, we need to know its equation of state (EOS), i.e., the pressure P as a function of the matter–energy density ϵ . The outer crust of the star is expected to be made of ^{56}Fe , as its binding energy per nucleon is the lowest among all the atoms. As we proceed towards the center, the density increases enormously and the matter becomes degenerate. At the nuclear density ($\epsilon_0 = 2.4 \times 10^{14} \text{g cm}^{-3}$), the nuclei dissolve and all the nucleons form a single huge nucleus. The composition of matter upto this density is fairly well understood. For densities $\epsilon > \epsilon_0$, we have to rely on extrapolation from known nuclear properties under terrestrial conditions. The goodness of such extrapolations is checked by how well it reproduces the values of

parameters like compression modulus of equilibrium nuclear matter, the nuclear saturation density, symmetry energy etc. (for which experimental estimates are available).

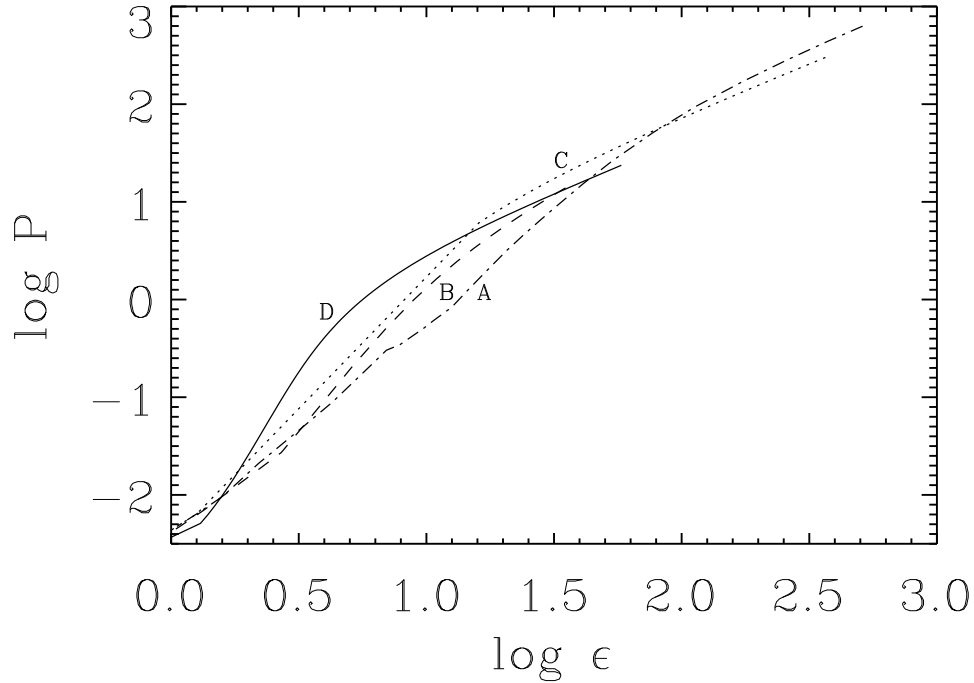


Figure 2.1: Logarithmic plot of pressure vs. matter density for the EOS models used here. The density and pressure are in units of $1.0 \times 10^{14} \text{ g cm}^{-3}$ and $(1.0 \times 10^{14}) c^2 \text{ cgs}$ respectively.

The structure of neutron stars depends sensitively on the EOS at high densities. Although the main composition of degenerate matter at densities higher than ϵ_0 is expected to be dominated by neutrons, significant admixtures of other elementary particles (such as pions, kaons and hyperons) are not ruled out. In the literature, many EOS models are available. The various formalisms used in deriving these models give rise to a substantial spread in their qualitative features. Which of these is the correct EOS model is therefore a fundamental question of physics. It is hoped that a theoretical computation of quantities of astrophysical interests using representative EOS models and subsequent comparison with observations will provide an answer to this question. This is one of the main motivations for the work presented in this thesis.

For excellent reviews on neutron star EOS models, we refer Canuto (1974), Canuto (1975) and Baym & Pethick (1975) (also see Shapiro & Teukolsky 1983). In this thesis, we have studied luminosities, disk temperature profiles and spectra for certain representative EOS models. An important

quantity that characterises EOS models is the stiffness parameter, defined as $S = d \log P / d \log \epsilon$. For higher values of S , the EOS model is stiffer. For every EOS, there exists a maximum possible stable mass (M_{\max}). The stiffer the EOS, the higher is the value of M_{\max} .

For our calculations, we choose four EOS models of widely varying stiffness parameters. This ensures sufficient generality of our results. We describe below the salient features of these models.

(A) *Pandharipande (hyperonic matter)*: One of the early attempts to derive nuclear EOS with admixture of hyperons is due to Pandharipande (1971), who assumed the hyperonic potentials to be similar to the nucleon–nucleon potentials, but altered suitably to represent the different isospin states. The many–body method adopted is based on the variational approach of Jastrow (1955). The two–body wave function was taken as satisfying a simplified form of the Bethe–Goldstone equation, in which terms representing the Pauli exclusion principle were omitted but simulated by imposing a ‘healing’ constraint on the wave function. This model is soft, i.e., the value of S is comparatively low. The nonrotating M_{\max} for this EOS is $1.41 M_{\odot}$.

(B) *Baldo, Bombaci & Burgio (AV14 + 3bf)*: Baldo, Bombaci & Burgio (1997) have given a microscopic EOS for asymmetric nuclear matter, derived from the Brueckner–Bethe–Goldstone many–body theory with explicit three–body terms. The three–body force parameters are adjusted to give a reasonable saturation point for nuclear matter. This model is intermediate in stiffness with nonrotating $M_{\max} = 1.79 M_{\odot}$.

(C) *Walecka (neutrons)*: The EOS model of Walecka (1974) corresponds to pure neutron matter and is based on a mean–field theory with exchange of scalar and (isoscalar) vector mesons representing the nuclear interaction. It is a stiff EOS model with nonrotating $M_{\max} = 2.28 M_{\odot}$.

(D) *Sahu, Basu & Datta*: Sahu, Basu & Datta (1993) gave a field theoretical EOS for neutron–rich matter in beta equilibrium based on the chiral sigma model. The model includes an isoscalar vector field generated dynamically and reproduces the empirical values of the nuclear matter saturation density and binding energy and also the isospin symmetry coefficient for asymmetric nuclear matter. The energy per nucleon of nuclear matter according to these authors is in very good agreement, upto about four times the equilibrium nuclear matter density, with estimates inferred from heavy–ion collision experimental data. This model is the stiffest among all the EOS models we have considered. The nonrotating M_{\max} for this EOS is $2.59 M_{\odot}$.

The pressure–density relationship of the above EOS models is illustrated in Fig 2.1. The composite EOS for the entire span of neutron star densities is constructed by joining one of the selected high density EOS models to that of Negele & Vautherin (1973) for the density range $10^{14} - 5 \times 10^{10} \text{ g cm}^{-3}$, Baym, Pethick & Sutherland (1971) for densities down to $\sim 10^3 \text{ g cm}^{-3}$ and

Feynman, Metropolis & Teller (1949) for densities less than 10^3g cm^{-3} .

2.5 The Results

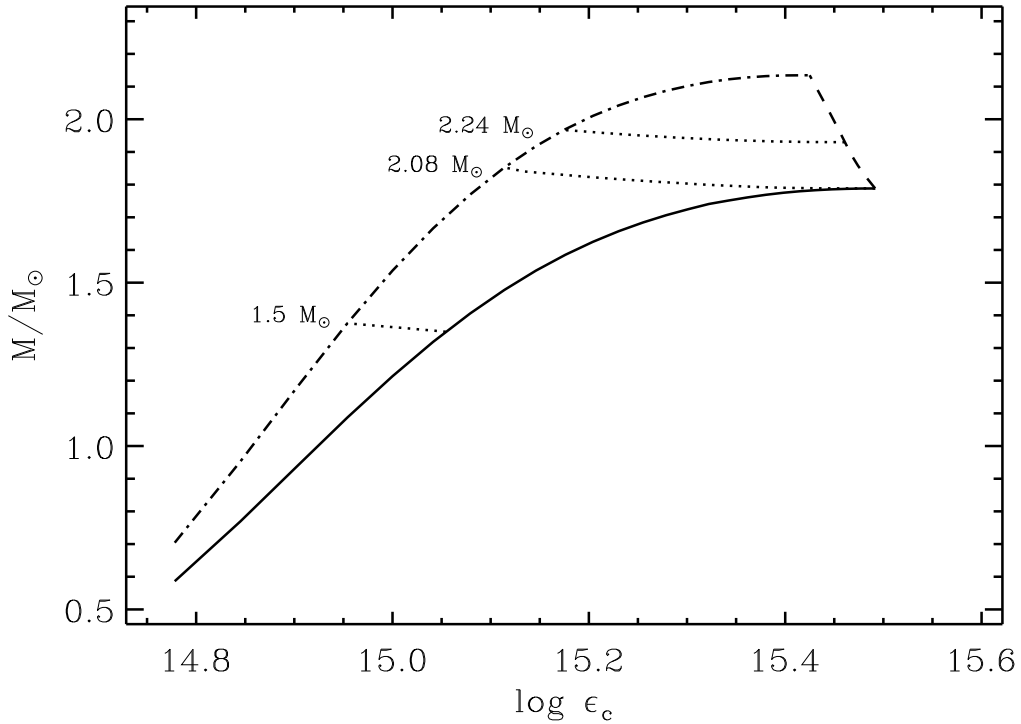


Figure 2.2: Semi-logarithmic plot of gravitational mass vs. central matter density (in unit of 10^{14}g cm^{-3}) for the EOS model B. The solid line is for static limit, dash-dot line is for mass-shed limit and the dashed line is for radial-instability limit. The stable equilibrium configurations occur only in the region, bound by these three limits (see the text). The dotted lines are evolutionary sequences with the values of corresponding M_0 written.

We calculate the equilibrium configurations of neutron stars with Ω_* ranging from 0 to the mass-shed limit value. In Fig 2.2, we illustrate the nonrotating limit, mass-shed limit and radial instability limit for the EOS model (B). Several evolutionary sequences are also shown.

In Fig 2.3, the above three limits are illustrated in $M - R$ space, for the same EOS model. It is to be noted that $M - R$ diagram has in general a negative slope for neutron stars (as we will see in Chapter 7, the slope is positive for strange stars).

We construct gravitational mass sequences for all the chosen EOS models. We take $M = 1.4 M_\odot$ (the canonical mass) for the purpose of illustration. In Fig 2.4, we plot Ω_* vs. J from the

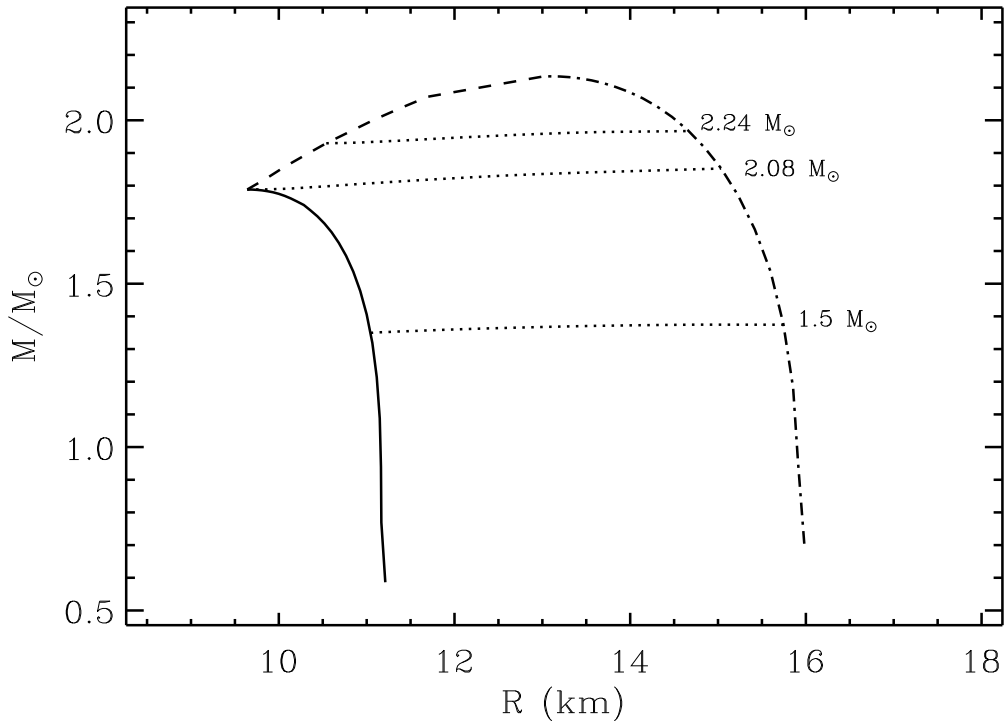


Figure 2.3: Plot of gravitational mass vs. equatorial radius for the EOS model B. All the lines are as described in Fig. 2.2.

nonrotating limit to the mass-shed limit. We see that both J and Ω_* increase monotonically. We also notice that for softer EOS, higher value of Ω_* can be achieved at the mass-shed limit, but the corresponding value of J is smaller.

In Fig 2.5, we plot Ω_* vs. T/W with other specifications same as in Fig 2.4. Here we always present the absolute value of W . As we will elaborate in Chapter 7, the higher the value of T/W , the greater is the possibility for the star to be a subject of triaxial instability. As we see from the figure, for a stiffer EOS, the value of T/W is higher, but the maximum value does not exceed 0.12. (for strange stars, it is 0.25 – 0.30, see Chapter 7).

The value of r_{orb} compared to that of R has profound effect on the disk luminosity, temperature profile and spectrum. We will illustrate the variations of r_{in} (radius of disk inner edge) and luminosities with Ω_* (for $M = 1.4 M_{\odot}$) in the next chapter.

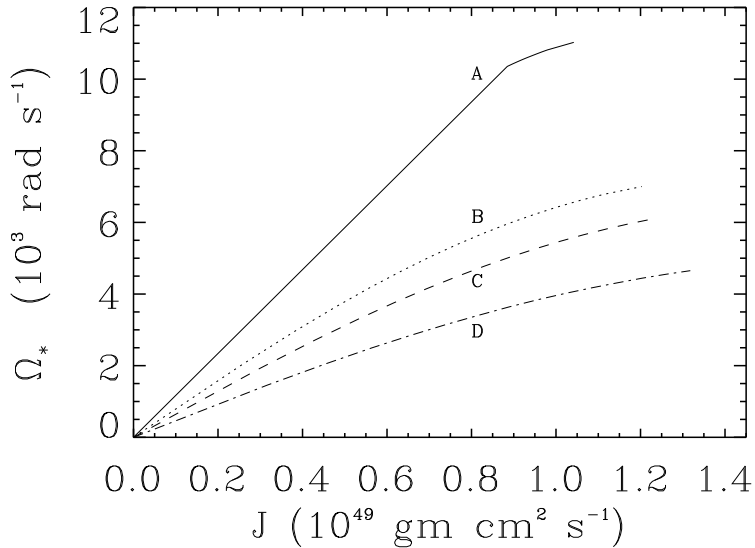


Figure 2.4: Angular speed (Ω_*) as a function of total angular momentum (J). The curves are for different EOS models (mentioned in the figure) and are for a fixed gravitational mass ($M = 1.4 M_\odot$).

2.6 Concluding Remarks

It is expected that the accreting neutron stars are rapidly rotating because of the huge amount of angular momentum, transferred to them by the accreted matter. The very short pulsation period ($P = 2.49\text{ms}$) of SAX J1808.4–3658 strengthens this speculation. Therefore we compute the equilibrium configurations for rapidly rotating neutron stars, considering the full effect of general relativity. Then using the structure parameters and metric coefficients for these configurations, we calculate general relativistically correct values for luminosities, disk temperature profiles and disk spectra as functions of Ω_* . Comparing these model spectra with the observed ones will help to constrain neutron star structure parameters, as well as the EOS. In the subsequent chapters, we will elaborate the importance of rapid-rotation-calculation, by showing that the results for such calculation is considerably different from those for Schwarzschild or Newtonian case.

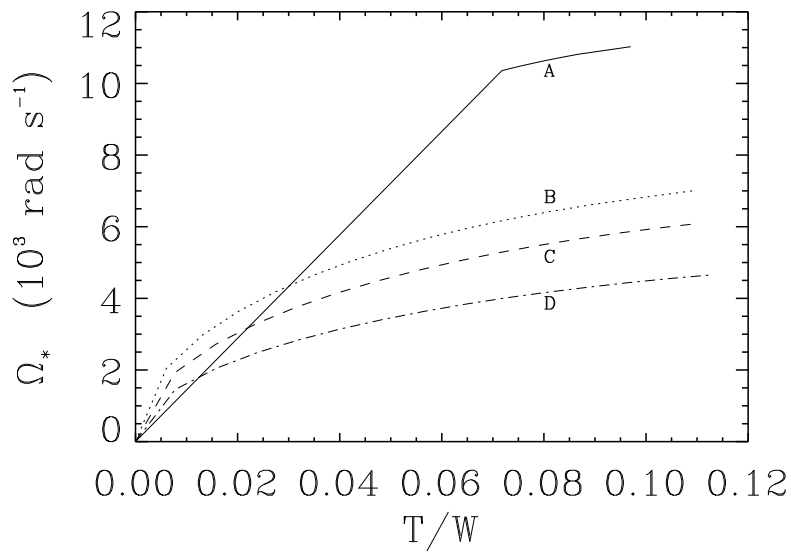


Figure 2.5: Angular speed (Ω_*) as a function of the ratio of rotational kinetic energy and gravitational binding energy (T/W). Curve labels have the same meaning as in Fig. 2.4.

Chapter 3

Calculation of Disk Temperature Profile

3.1 Introduction

The soft X-ray spectra of luminous low-mass X-ray binaries (LMXBs) are believed to originate in geometrically thin accretion disks around neutron stars with weak surface magnetic fields (see for e.g. White 1995). An important parameter in modeling these spectra is the maximum value of the effective temperature in the accretion disk. The effective temperature profile in the disk can be estimated (assuming the disk to radiate from its surface like a blackbody) if one knows the accretion energy released in the disk. In a Newtonian treatment, the innermost region of an accretion disk surrounding a neutron star with weak magnetic field will extend rather close to the neutron star surface. The amount of energy released in the disk will be one-half of the total accretion energy, the other half being released in the thin boundary layer between the disk's inner edge and the neutron star's surface. This then gives the disk effective temperature (T_{eff}) varying with the radial distance (r) as $T_{\text{eff}} \propto r^{-3/4}$ and the maximum effective temperature ($T_{\text{eff}}^{\text{max}}$) will depend on the (nonrotating) neutron star mass (M) and radius (R) as $T_{\text{eff}}^{\text{max}} \propto (M\dot{M}/R^3)^{1/4}$, where \dot{M} is the steady state mass accretion rate. The value of ($T_{\text{eff}}^{\text{max}}$) in the disk, in this approach, occurs at a radial distance $1.36 R$.

Mitsuda et al. (1984) parameterized the disk spectrum by the maximum temperature of the disk, using the above formalism and assuming the mass of the neutron star is equal to $1.4 M_{\odot}$. These authors assumed that the inner parts of the disk do not contribute to the X-ray spectrum, and suggested a multi-color spectrum for the X-ray emission from the disk. It was shown by these authors, that the observed spectra of Sco X-1, 1608-52, GX 349+2 and GX 5-1, obtained with the *Tenma* satellite, can be well fitted with the sum of a multi-color spectrum and a single

blackbody spectrum (presumably coming from the boundary layer). White, Stella & Parmar (1988) (WSP) suggested that the simple blackbody accretion disk model should be modified to take into account the effects of electron scattering. Using *EXOSAT* observations, these authors compared the spectral properties of the persistent emission from a number of X-ray burst sources with various X-ray emission models. This work suggests that either the neutron star (in each system considered) rotates close to equilibrium with the Keplerian disk, or that most of the boundary layer emission is not represented by a blackbody spectrum.

For accretion disks around compact objects, one possibility is that of the accretion disk not being Keplerian in nature. For e.g. Titarchuk, Lapidus & Muslimov (1998) have formulated a boundary problem in which the Keplerian accretion flow in the inner disk is smoothly adjusted to the neutron star rotation rate. The generality of such a formulation permits application even to black holes, but only for certain assumed inner boundary conditions. These authors demonstrate that there exists a transition layer (having an extent of the order of the neutron star radius) in which the accretion flow is sub-Keplerian. An attractive feature of this formalism is that it allows super-Keplerian motion at the outer boundary of the transition layer, permitting the formation of a hot blob that ultimately bounces out to the magnetosphere. This formalism (Titarchuk & Osherovich 1999; Osherovich & Titarchuk 1999a; Osherovich & Titarchuk 1999b; Titarchuk, Osherovich & Kuznetsov 1999) therefore provides a mechanism for the production of high frequency quasi-periodic oscillations (QPOs) observed in the X-ray flux from several LMXBs. Such effects, when taken into account, can modify the Newtonian disk temperature profile (Chakrabarti & Titarchuk 1995).

There are several other effects which will modify the Newtonian disk temperature profile, such as the effects of general relativity and of irradiation of the disk by the central neutron star. The wind mass loss from the disk and the residual magnetic field near the disk's inner edge may also play a part in modifying the effective temperature (Knigge 1999). Czerny, Czerny & Grindlay (1986) calculated LMXB disk spectra assuming that a disk radiates locally as a blackbody with the energy flux determined by viscous forces, as well as irradiation by the boundary layer, and took into account relativistic effects, some of them in an approximate way. The possible effects of general relativity were also discussed by Hanawa (1989), using the Schwarzschild (nonrotating) metric, assuming that the neutron star radius is less than the radius of the innermost stable circular orbit ($r_{\text{in}} = 6GM/c^2$), which they identified as the disk inner boundary. The color temperature was assumed to be higher than the effective temperature by a factor of 1.5. It was found by Hanawa (1989) that the observations are consistent with a geometrically thin, optically thick accretion disk, whose inner edge is at $r = r_{\text{in}}$, r being the Schwarzschild radial coordinate.

An important dynamical aspect of disk accretion on to a weakly magnetized neutron star is that

the neutron star will get spun up to its equilibrium period, which is of the order of milliseconds (see Bhattacharya & van den Heuvel 1991, and references therein). The effect of rotation is to increase the equatorial radius of the neutron star, and also to relocate the innermost stable circular orbit (for a corotating disk) closer to the stellar surface (as compared to the Schwarzschild case). These effects will be substantial for rapid rotation rates in a fully general relativistic treatment that includes rotation. Therefore, for accreting neutron stars with low magnetic fields, the stellar radius can be greater or less than the radius of the innermost stable orbit, depending on the neutron star equation of state and the spacetime geometry. The effect of magnetic field will be to constrain the location of the inner-edge of the accretion disk to the magnetospheric (Alfvén) radius. In such a case, r_{in} would lose the astrophysical relevance as discussed here. However, this will be so only if the magnetic field strength (B) is large. The problem addressed in this paper refer to LMXBs which contain old neutron stars which are believed to have undergone sufficient magnetic field decay (Bhattacharya & Datta 1996). Clearly, for low magnetic field case, a number of different disk geometries will be possible if general relativistic effects of rotation are taken into account. These structural differences influence the effective temperature profile and the conclusions derived by Czerny, Czerny & Grindlay (1986) and Hanawa (1989) are likely to be modified.

In this chapter, we attempt to highlight the effects of general relativity and rotation of the neutron star on the accretion disk temperature profile. For simplicity (unlike Titarchuk, Lapidus & Muslimov 1998), we assume the accretion disk to be fully Keplerian, geometrically thin and optically thick. We construct gravitational mass sequences for the chosen EOS models and calculate the luminosities and temperature profiles for equilibrium configurations corresponding to different Ω_* values.

In section 3.2, we will describe the procedure for disk temperature profile calculation. We will show the results in section 3.3 and summarise the content of the chapter in section 3.4.

3.2 The Effective Temperature of the Disk

3.2.1 Effects of General Relativity and Rotation

The effective temperature in the disk (assumed to be optically thick) is given by

$$T_{\text{eff}} = (F/\sigma)^{1/4} \quad (3.1)$$

where σ is the Stephan–Boltzmann constant and F is the X–ray energy flux per unit surface area. We use the formalism given by Page & Thorne (1974), who gave the following general relativistic

expression for F emitted from the surface of an (geometrically thin and non-self-gravitating) accretion disk around a rotating black hole:

$$F(r) = \frac{\dot{M}}{4\pi r} f(r) \quad (3.2)$$

where

$$f(r) = -\Omega_{K,r}(\tilde{E} - \Omega_K l)^{-2} \int_{r_{\text{in}}}^r (\tilde{E} - \Omega_K l) l_{,r} dr. \quad (3.3)$$

Here r_{in} is the disk inner edge radius, \tilde{E} , l are the specific energy and specific angular momentum of a test particle in a Keplerian orbit and Ω_K is the Keplerian angular velocity at radial distance r . In our notation, a comma followed by a variable as subscript to a quantity, represents a derivative of the quantity with respect to the variable. We use the geometric units $c = G = 1$. Eq. (3.3) is valid for a spacetime described by a stationary, axisymmetric, asymptotically flat and reflection-symmetric (about the equatorial plane) metric. Our metric (2.3) satisfies all these conditions.

For accreting neutron stars located within the disk inner edge, the situation is analogous to the black hole binary case, and the above formula, using a metric describing a rotating neutron star, can be applied directly for our purpose. However, unlike the black hole binary case, there can be situations for neutron star binaries where the neutron star radius exceeds the innermost stable circular orbit radius. In such situations, the boundary condition, assumed by Page & Thorne (1974), that the torque vanishes at the disk inner edge will not be strictly valid. Use of Eq. (3.1) will then be an approximation. This will affect the temperatures close to the disk inner edge, but not the $T_{\text{eff}}^{\text{max}}$ to any significant degree (see section 3.4 for discussion).

In order to evaluate T_{eff} using Eq. (3.1), we need to know the radial profiles of \tilde{E} , l and Ω_K . For this purpose, first we construct gravitational mass sequences starting from the static limit all the way upto the mass-shed limit. Then the radial profiles are calculated using Eqs. (2.43), (2.44) and (2.48).

Eq. (3.1) gives the effective disk temperature T_{eff} with respect to an observer comoving with the disk. From the observational viewpoint this temperature must be modified, taking into account the gravitational redshift and the rotational Doppler effect. In order to keep our analysis tractable, we use the expression given in Hanawa (1989) for this modification :

$$1 + z = \left(1 - \frac{3M}{r}\right)^{-1/2}. \quad (3.4)$$

This equation is a special case of Eq. (5.3) with the inclination angle $i = 0$ and Schwarzschild metric used. Such assumptions make the calculation easier, but does not affect the general conclusion of Chapter 4. With this correction for $(1+z)$, we define a temperature relevant for observations (T_{obs}) as:

$$T_{\text{obs}} = \frac{1}{1+z} T_{\text{eff}} \quad (3.5)$$

3.2.2 Disk Irradiation by the Neutron Star

For luminous LMXBs, there can be substantial irradiation of the disk surface by the radiation coming from the neutron star boundary layer. The radiation temperature at the surface of a disk irradiated by a central source is given by (King, Kolb & Burderi 1996)

$$T_{\text{irr}}(r) = \left(\frac{\eta \dot{M} c^2 (1-\beta) h}{4\pi\sigma r^2} \frac{h}{r} (n-1) \right)^{1/4} \quad (3.6)$$

where η is the efficiency of conversion of accreted rest mass to energy, β is the X-ray albedo, h is the half-thickness of the disk at r and n is given by the relation $h \propto r^n$. For actual values of β , h/r and n , needed for our computation here, we choose the same values (i.e., 0.9, 0.2 and 9/7 respectively) as given in King, Kolb & Burderi (1996). It is to be noted that the constant value taken for h/r is an approximation, as $n \neq 1$. However, it does not change the relative feature (which may be important for disk instability) of $T_{\text{irr}}(r)$ and $T_{\text{eff}}(r)$ much. Although Eq. (3.6) is derived based on Newtonian considerations, corrections due to general relativity (including that of rapid rotation) will be manifested through the factor η . We have made a general relativistic evaluation of η for various neutron star rotating configurations, corresponding to realistic neutron star EOS models, as described in Thampan & Datta (1998). Since $T_{\text{irr}}(r) \propto r^{-1/2}$ and $T_{\text{eff}}(r) \propto r^{-3/4}$, T_{irr} will dominate over T_{eff} only at large distances. The net effective temperature of the disk will be given by (see Vrtilik et al. 1990)

$$T_{\text{disk}}(r) = (T_{\text{eff}}^4(r) + T_{\text{irr}}^4(r))^{1/4} \quad (3.7)$$

For the modeling of X-ray sources presented in Chapter 4, we find that T_{irr} does not play any significant role. However, since this quantity has consequences for the disk instability, we calculate it using Eq. (3.6) and illustrate it for the rotating neutron star models considered here.

Table 3.1: Centrifugal mass-shed limit (Ω_{ms}), the neutron star radius (R), the disk inner edge radius (r_{in}), specific gravitational energy release in the boundary layer (E_{BL}) and in the disk (E_{D}), their ratio $E_{\text{BL}}/E_{\text{D}}$, the maximum effective temperature ($T_{\text{eff}}^{\text{max}}$), the radial location ($r_{\text{eff}}^{\text{max}}$) in the disk corresponding to $T_{\text{eff}}^{\text{max}}$, $T_{\text{obs}}^{\text{max}}$ (see text) and the radial location ($r_{\text{obs}}^{\text{max}}$) corresponding to this. These values are listed for two values of M for all EOS models considered here (except for EOS model (A), where the maximum neutron star mass is less than $1.78 M_{\odot}$, so only $M = 1.4 M_{\odot}$ is considered). The number following the letter E represents powers of 10. The values of E_{BL} & $E_{\text{BL}}/E_{\text{D}}$ corresponding to $\Omega_* = \Omega_{\text{ms}}$ are expected to be zero and the small values given here are the measure of numerical error.

EOS Model		(A)	(B)		(C)		(D)	
M		$1.4 M_{\odot}$	$1.4 M_{\odot}$	$1.78 M_{\odot}$	$1.4 M_{\odot}$	$1.78 M_{\odot}$	$1.4 M_{\odot}$	$1.78 M_{\odot}$
Ω_{ms} (10^3 rad s^{-1})		11.026	7.001	8.219	6.085	6.808	4.652	5.088
R (km)	$\Omega_* = 0$	7.46	11.01	9.84	12.28	12.32	14.74	15.76
	$\Omega_* = \Omega_{\text{ms}}$	11.44	15.72	15.19	17.26	17.28	20.74	21.16
r_{in} (km)	$\Omega_* = 0$	12.40	12.41	15.81	12.41	15.75	14.74	15.79
	$\Omega_* = \Omega_{\text{ms}}$	11.44	15.72	15.19	17.26	17.28	20.74	21.16
E_{BL} ($m_0 c^2$)	$\Omega_* = 0$	0.275	0.153	0.262	0.128	0.185	0.097	0.136
	$\Omega_* = \Omega_{\text{ms}}$	9.0E-5	5.0E-5	5.0E-5	4.0E-5	1.4E-4	1.4E-4	6.0E-5
E_{D} ($m_0 c^2$)	$\Omega_* = 0$	0.057	0.057	0.057	0.057	0.057	0.055	0.057
	$\Omega_* = \Omega_{\text{ms}}$	0.073	0.057	0.071	0.053	0.064	0.045	0.054
$E_{\text{BL}}/E_{\text{D}}$	$\Omega_* = 0$	4.809	2.673	4.574	2.248	3.239	1.779	2.387
	$\Omega_* = \Omega_{\text{ms}}$	1.0E-3	9.0E-4	7.0E-4	8.0E-4	2.0E-3	3.0E-3	1.0E-3
$T_{\text{eff}}^{\text{max}}$ ($M_{17}^{1/4} \times 10^5 \text{ K}$)	$\Omega_* = 0$	47.64	47.64	42.16	47.64	42.16	45.98	42.16
	$\Omega_* = \Omega_{\text{ms}}$	56.94	46.54	49.28	43.80	45.45	38.32	39.42
$r_{\text{eff}}^{\text{max}}$ (km)	$\Omega_* = 0$	19.76	19.76	25.18	19.75	25.06	21.13	25.16
	$\Omega_* = \Omega_{\text{ms}}$	16.14	21.64	21.42	23.68	24.05	28.39	29.21
$T_{\text{obs}}^{\text{max}}$ ($M_{17}^{1/4} \times 10^5 \text{ K}$)	$\Omega_* = 0$	39.98	39.98	35.05	39.98	35.05	38.87	35.05
	$\Omega_* = \Omega_{\text{ms}}$	45.99	39.98	39.98	37.79	37.79	33.95	33.95
$r_{\text{obs}}^{\text{max}}$ (km)	$\Omega_* = 0$	22.29	22.31	28.45	22.31	28.30	23.44	28.41
	$\Omega_* = \Omega_{\text{ms}}$	18.70	23.69	24.58	25.60	26.90	30.14	31.72

3.3 The Results

We have calculated the disk temperature profiles for rapidly rotating, constant gravitational mass sequences of neutron stars in general relativity. For our purpose here, we choose two values for the gravitational mass, namely, $1.4 M_\odot$ and $1.78 M_\odot$, the former being the canonical mass for neutron stars (as inferred from binary X-ray pulsar data), while the latter is the estimated mass for the neutron star in Cygnus X-2 (Orosz & Kuulkers 1999), that we use in Chapter 4.

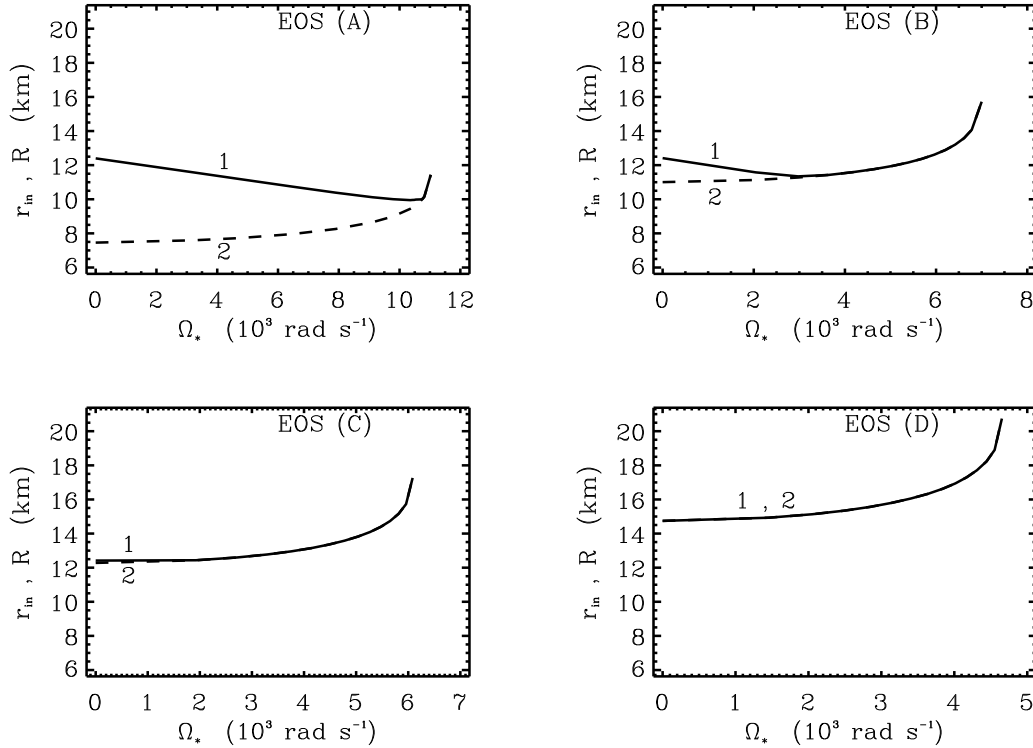


Figure 3.1: Disk inner edge radius (r_{in} ; curve 1) and neutron star radius (R ; curve 2), as functions of neutron star angular velocity (Ω_*) for various EOS models. The curves are for a fixed gravitational mass ($M = 1.4 M_\odot$) of the neutron star.

In Table 3.1, we list the values of the stellar rotation rate at centrifugal mass-shed limit (Ω_{ms}); the neutron star radius (R); the radius of the inner edge of the disk (r_{in}); E_{BL} , E_{D} and the ratio $E_{\text{BL}}/E_{\text{D}}$; $T_{\text{eff}}^{\text{max}}$ & $T_{\text{obs}}^{\text{max}}$ and $r_{\text{eff}}^{\text{max}}$ & $r_{\text{obs}}^{\text{max}}$ for the two mentioned values of M and for the different EOS models. The last nine computed quantities are given for two values of neutron star rotation rate, namely, the static limit ($\Omega_* = 0$) and the centrifugal mass-shed limit ($\Omega_* = \Omega_{\text{ms}}$). E_{D} and E_{BL} are in specific units (i.e. units of rest energy $m_0 c^2$, of the accreted particle). The temperatures are expressed in units of $\dot{M}_{17}^{1/4} \times 10^5$ K (where $\dot{M}_{17} = \dot{M}/10^{17} \text{ g s}^{-1}$). From this Table it may

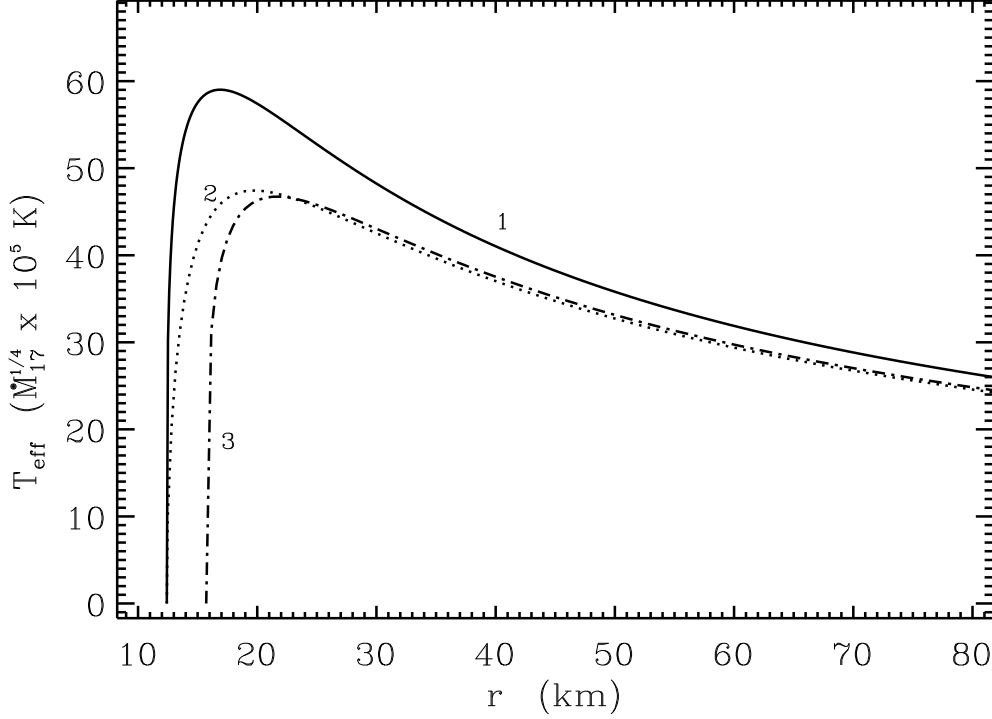


Figure 3.2: General relativistic corrections to Newtonian temperature profiles for EOS model (B) and the neutron star gravitational mass $M = 1.4 M_{\odot}$. Curve 1 corresponds to the Newtonian case, curve 2 to the Schwarzschild case and curve 3 to a neutron star rotating at the centrifugal mass-shed limit, calculated using the metric (2.3). For curve 1, it is assumed that, $r_{\text{in}} = 6GM/c^2$. In this and all subsequent figures (except Fig. 3.6) the temperature is expressed in units of $\dot{M}_{17}^{1/4} \times 10^5$ K, where \dot{M}_{17} is the steady state mass accretion rate in units of 10^{17}g s^{-1} .

be seen that for a given neutron star gravitational mass (M): (1) Ω_{ms} decreases for increasing stiffness of the EOS model. (2) R is greater for stiffer EOS. (3) The behavior of r_{in} depends on whether $r_{\text{ms}} > R$ or $r_{\text{ms}} < R$ and hence appears non-monotonic. (4) E_{BL} for the non-rotating configuration decreases with stiffness of the EOS. For a configuration rotating at the mass-shed limit, E_{BL} is insignificant. (5) In the non-rotating limit, E_{D} remains roughly constant for varying stiffness of the EOS model. However, for the rapidly rotating case, the value of E_{D} decreases with increasing stiffness. (6) The ratio $E_{\text{BL}}/E_{\text{D}}$ in static limit is highest for the softest EOS model. For the rapidly rotating case, this ratio is uniformly insignificant. (7) $T_{\text{eff}}^{\text{max}}$ and $T_{\text{obs}}^{\text{max}}$ decrease with increasing stiffness of the EOS models. However, these values exhibit non-monotonic variation with Ω_* (see Fig. 3.5 for the first parameter). (8) The rest of the parameters, namely, $r_{\text{eff}}^{\text{max}}$ and $r_{\text{obs}}^{\text{max}}$ are non-monotonic with respect to the EOS stiffness parameter.

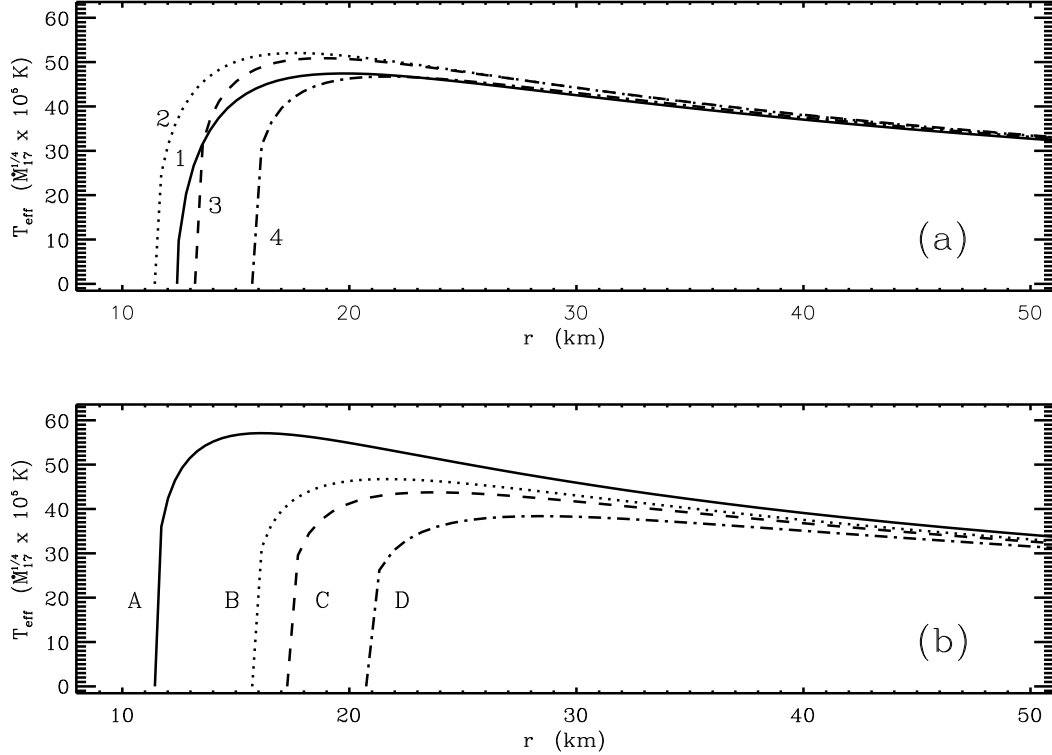


Figure 3.3: Temperature profiles incorporating the effects of rotation of the neutron star. The plots correspond to (a) For EOS model (B) and an assumed neutron star mass of $M = 1.4 M_{\odot}$ for rotation rates: $\Omega_* = 0$ (curve 1), $\Omega_* = 3.647 \times 10^3 \text{ rad s}^{-1}$ (curve 2), $\Omega_* = 6.420 \times 10^3 \text{ rad s}^{-1}$ (curve 3) & $\Omega_* = 7.001 \times 10^3 \text{ rad s}^{-1} = \Omega_{\text{ms}}$ (curve 4) and (b) For the same assumed mass and $\Omega_* = \Omega_{\text{ms}}$ for the EOS models A, B, C and D.

In Fig. 3.1, we display the variation of R (the dashed curve) and r_{in} (the continuous curve) with Ω_* for $M = 1.4 M_{\odot}$ for the four EOS models that we have chosen. From this figure it is seen that for a constant gravitational mass sequence, for both soft and intermediate EOS models, $r_{\text{in}} > R$ for slow rotation rates whereas, for rapid rotation rates $r_{\text{in}} = R$. In other words, for neutron stars spinning very rapidly, the inner edge of the disk will almost coincide with the stellar surface. It may be noted that for the stiff EOS models, this condition obtains even at slow rotation rates of the neutron star.

It is instructive to make a comparison of the temperature profiles calculated using a Newtonian prescription with that obtained in a relativistic description using Schwarzschild metric. This is shown in Fig. 3.2, for the EOS model (B) and $M = 1.4 M_{\odot}$ (the trend is similar for all the EOS). The vertical axis in this figure is T_{eff} (in this and all other figures, the temperatures are shown in units of $M_{17}^{1/4}$) and the horizontal axis, the radial distance in km. This figure underlines

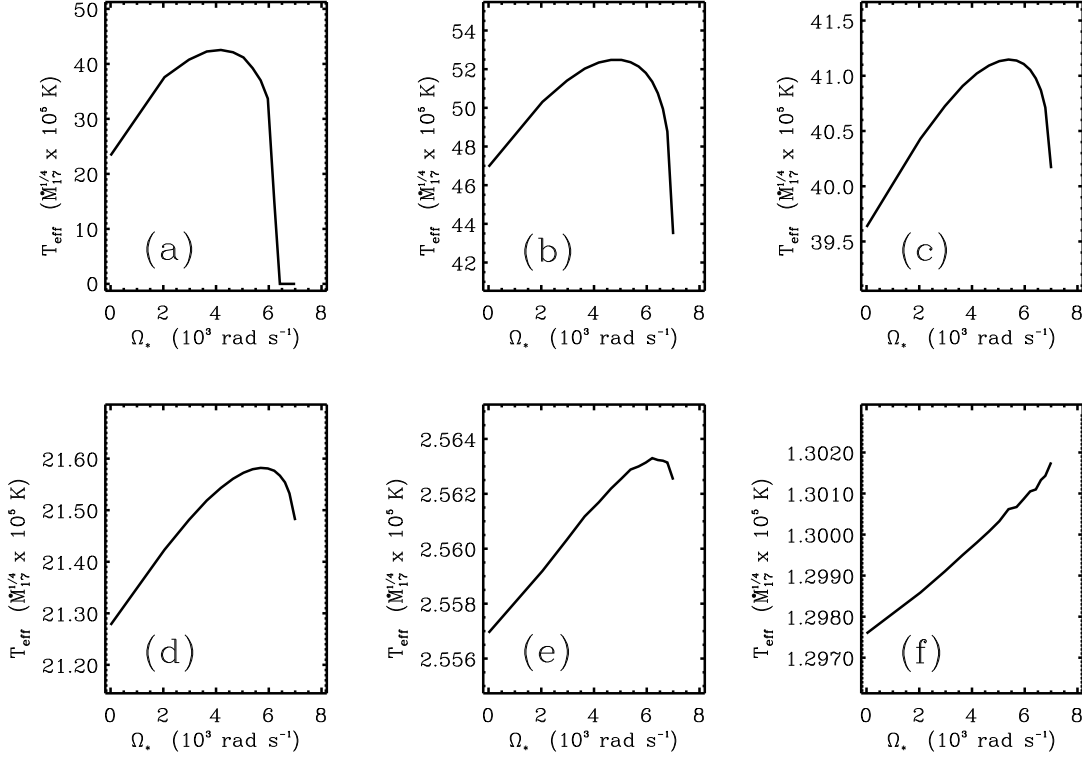


Figure 3.4: Plots of T_{eff} vs. Ω_* for chosen constant radial distances for fixed neutron star mass $M = 1.4 M_{\odot}$ and EOS model B. The plots correspond to (a) $r = 13$ km, (b) $r = 18$ km, (c) $r = 35$ km, (d) $r = 100$ km, (e) $r = 2000$ km and (f) $r = 5000$ km.

the importance of general relativity in determining the accretion disk temperature profiles; the Schwarzschild result for $T_{\text{eff}}^{\text{max}}$ is always less than the Newtonian result, and for the neutron star configuration considered here, the overestimate is almost 25%. For the sake of illustration, we also show the corresponding curve for a neutron star rotating at the mass-shed limit (curve 4, Fig. 3.3a). The disk inner edge is at the radius of the innermost stable circular orbit for all the cases. Note that the disk inner edge should be at R for Newtonian case; but we have taken $r_{\text{in}} = 6GM/c^2$ as assumed in Shapiro & Teukolsky (1983).

The effect of neutron star rotation on the accretion disk temperature, treated general relativistically, is illustrated in Fig. 3.3a and 3.3b. Fig. 3.3a corresponds to the EOS model (B). The qualitative features of this graph are similar for the other EOS models, and are not shown here. However, the temperature profiles exhibit a marked dependence on the EOS. This dependence is illustrated in Fig. 3.3b, which is done for a particular value of $\Omega_* = \Omega_{\text{ms}}$. All these temperature profiles have been calculated for a neutron star mass equal to $1.4 M_{\odot}$. The temperature profiles shown in Fig. 3.3a do not have a monotonic behavior with respect to Ω_* . This behavior is a

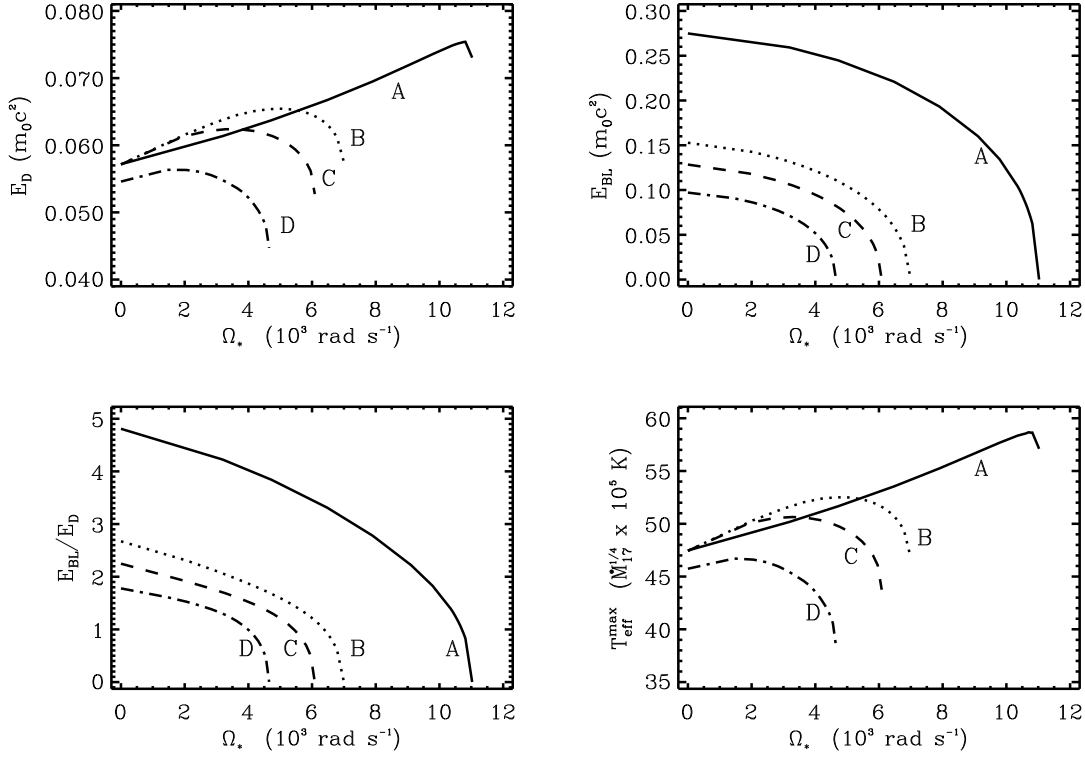


Figure 3.5: The variations of the E_D , E_{BL} , E_{BL}/E_D and $T_{\text{eff}}^{\text{max}}$, with Ω_* for a chosen neutron star mass value of $1.4 M_\odot$ for the four EOS models. The curves have the same significance as Fig. 3.3b.

composite of two underlying effects: (i) the energy flux emitted from the disk increases with Ω_* and (ii) the nature of the dependence of r_{in} (where T_{eff} vanishes : the boundary condition) on Ω_* (see Fig. 3.1). This is more clearly brought out in Fig. 3.4, where we have plotted of T_{eff} vs. Ω_* for selected constant radial distances (indicated in six different panels) and EOS (B). At large radial distances, the value T_{eff} is almost independent of the boundary condition; hence the temperature always increases with Ω_* in Fig. 3.4f.

The variations of E_D , E_{BL} , the ratio E_{BL}/E_D and $T_{\text{eff}}^{\text{max}}$ with Ω_* are displayed in Fig. 3.5 for all EOS models considered here. All the plots correspond to $M = 1.4 M_\odot$. Unlike constant central density neutron star sequences (Thampan & Datta 1998), for the constant gravitational mass sequences, E_D does not have a general monotonic behavior with Ω_* . $T_{\text{eff}}^{\text{max}}$ has a behavior akin to that of E_D (because of the reasons mentioned earlier). E_{BL} decreases with Ω_* , slowly at first but rapidly as Ω_* tends to Ω_{ms} . The variation of E_{BL}/E_D with respect to Ω_* is similar to that of E_{BL} .

We provide a comparison between the effective temperature (Eq. 3.1) and the irradiation

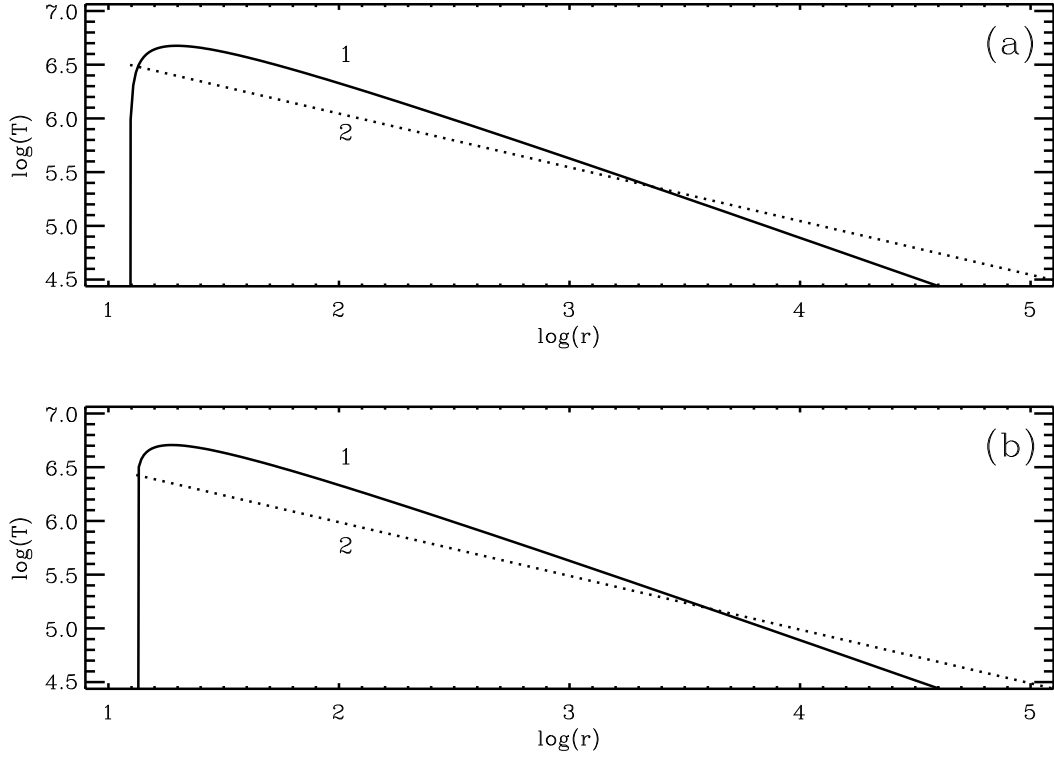


Figure 3.6: Comparison between the radial profiles of T_{eff} (curve 1) and T_{irr} (curve 2), calculated for $\eta = E_{\text{BL}} + E_{\text{D}}$, $\beta = 0.9$, $h/r = 0.2$ and $n = 9/7$ in Eq. (3.6) for two values of neutron star spin rates: (a) $\Omega_* = 0$ and (b) $\Omega_* = 6.420 \times 10^3 \text{ rad s}^{-1}$. The curves are for a neutron star configuration having $M = 1.4 M_{\odot}$, described by EOS model B. The temperatures are in units of $M_{17}^{1/4}$, and the radial extent is in km. For illustrative purposes, we have displayed this comparison in a log-log plot.

temperature (Eq. 3.6), in Fig. 3.6. We have taken $\eta = E_{\text{BL}} + E_{\text{D}}$. Fig. 3.6a is for $\Omega_* = 0$ while Fig. 3.6b is for a higher $\Omega_* = 6420 \text{ rad s}^{-1}$. The curves are for the gravitational mass corresponding to $1.4 M_{\odot}$ for the EOS model (B). The irradiation temperature becomes larger than the effective temperature at some large value of the radial distance, the ratio of the former to the latter becoming increasingly large beyond this distance. For E_{BL} small compared to E_{D} (as will be the case for a rapid neutron star spin rate), irradiation effects in the inner disk region will not be significant. Defining the radial point where the irradiation temperature profile crosses the effective temperature profile as $r = r_{\text{cross}}$ and the corresponding temperature as T_{cross} , we display plots of r_{cross} and T_{cross} with Ω_* respectively in Figs. 3.7a and 3.7b. It can be seen that r_{cross} increases with Ω_* , just as E_{S} does, and hence the irradiation effect decreases with increasing Ω_* . Therefore T_{cross} decreases with increasing Ω_* .

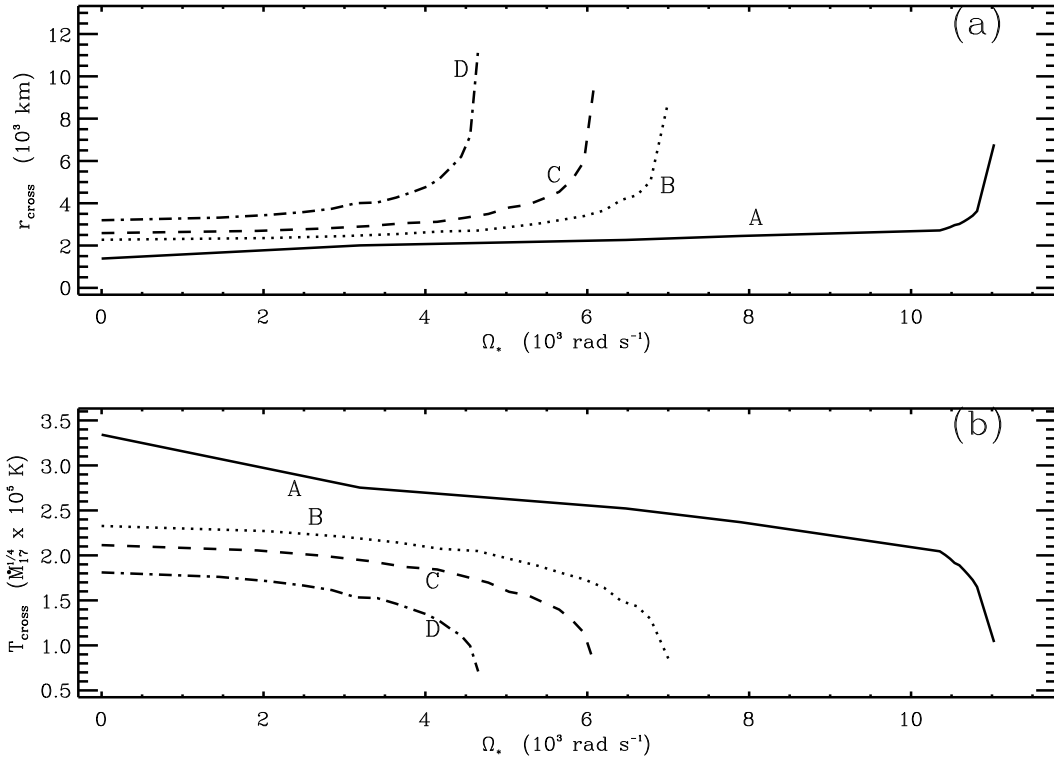


Figure 3.7: Plots: (a) r_{cross} vs. Ω_* and (b) T_{cross} vs. Ω_* . These are for a fixed neutron star gravitational mass of $M = 1.4 M_{\odot}$ and for the different EOS models as in Fig. 3.3b. Here T_{irr} is calculated for $\eta = E_{\text{BL}} + E_{\text{D}}$, $\beta = 0.9$, $h/r = 0.2$ and $n = 9/7$.

In Fig. 3.8, we illustrate the disk temperature (T_{disk}) profile for EOS model (B) corresponding to $M = 1.4 M_{\odot}$ for various values of Ω_* . We illustrate the variation of T_{disk} with Ω_* at fixed radial points in the disk in Fig. 3.9. The effect of T_{irr} on T_{disk} can be noted in Fig. 3.9f.

3.4 Summary and Discussion

In this chapter, we have calculated the temperature profiles of accretion disks around rapidly rotating and non-magnetized neutron stars, using a fully general relativistic formalism. The maximum temperature and its location in the disk are found to differ substantially from their values corresponding to the Schwarzschild space-time, depending on the rotation rate of the accreting neutron star. This shows the importance of the rapid-rotation-calculation.

A few comments regarding the validity of the Page & Thorne (1974) formalism for accreting neutron star binaries are in order here. Unlike for the case of black holes, neutron stars possess hard surface that could be located outside the marginally stable orbit. For neutron star binaries,

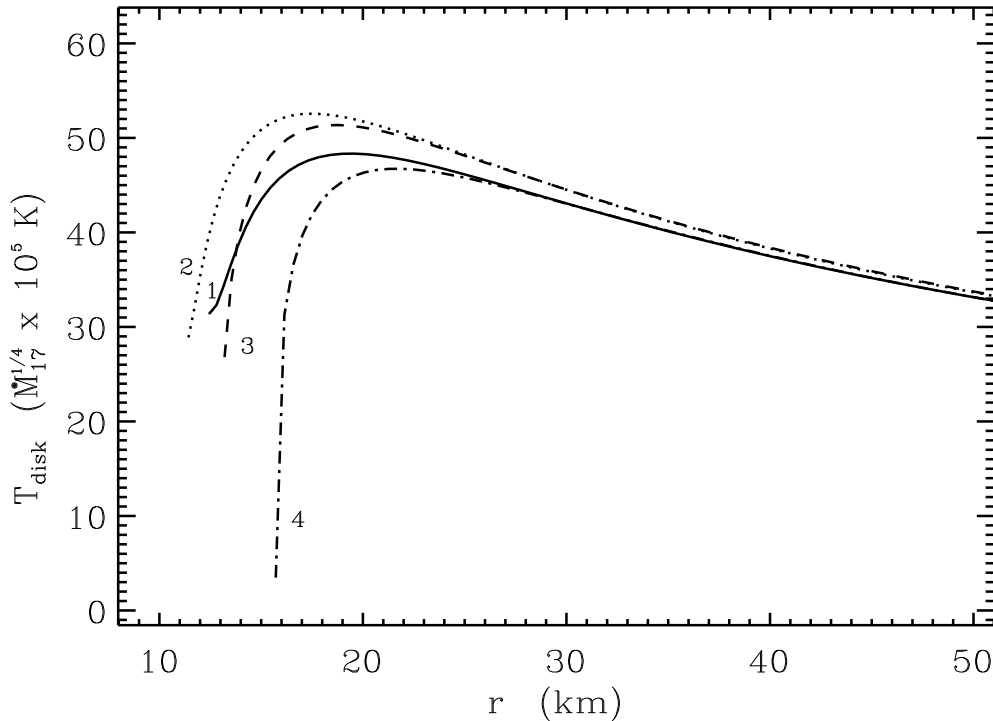


Figure 3.8: The disk temperature (T_{disk}) profiles for a $M = 1.4 M_{\odot}$ neutron star corresponding to EOS model (B), having various rotation rates as in Fig. 3.3a. These curves are obtained for $\eta = E_{\text{BL}}$, and the same values of β , h/r and n as in Fig. 3.6 are used.

this gives rise to a possibility of the disk inner edge coinciding with the neutron star surface. We have assumed that the torque (and hence the flux of energy) vanishes at the disk inner edge even in cases where the latter touches the neutron star surface. In the case of rapid spin of the neutron star, the angular velocity of a particle in Keplerian orbit at disk inner edge will be close to the rotation rate of the neutron star. Therefore, the torque between the neutron star surface and the inner edge of the disk is expected to be negligible. Independently of whether or not the neutron star spin is large, Page & Thorne (1974) argued that the error in the calculation of T_{eff} will not be substantial outside a radial distance r_o , where r_o is given by $r_o - r_{\text{in}} = 0.1r_{\text{in}}$. In our calculation, we find that $r_{\text{eff}}^{\text{max}}$ (which is the most important region for the generation of X-rays) is greater than r_o by several kilometers for all the cases considered.

Temperature profile is the main ingredient for the calculation of disk spectrum. As we have seen that both general relativity and rapid rotation have profound effect on the inner disk temperature profile, we expect the modeling of hard X-ray spectrum to be very much sensitive to them. This we will study in Chapters 5 & 6.

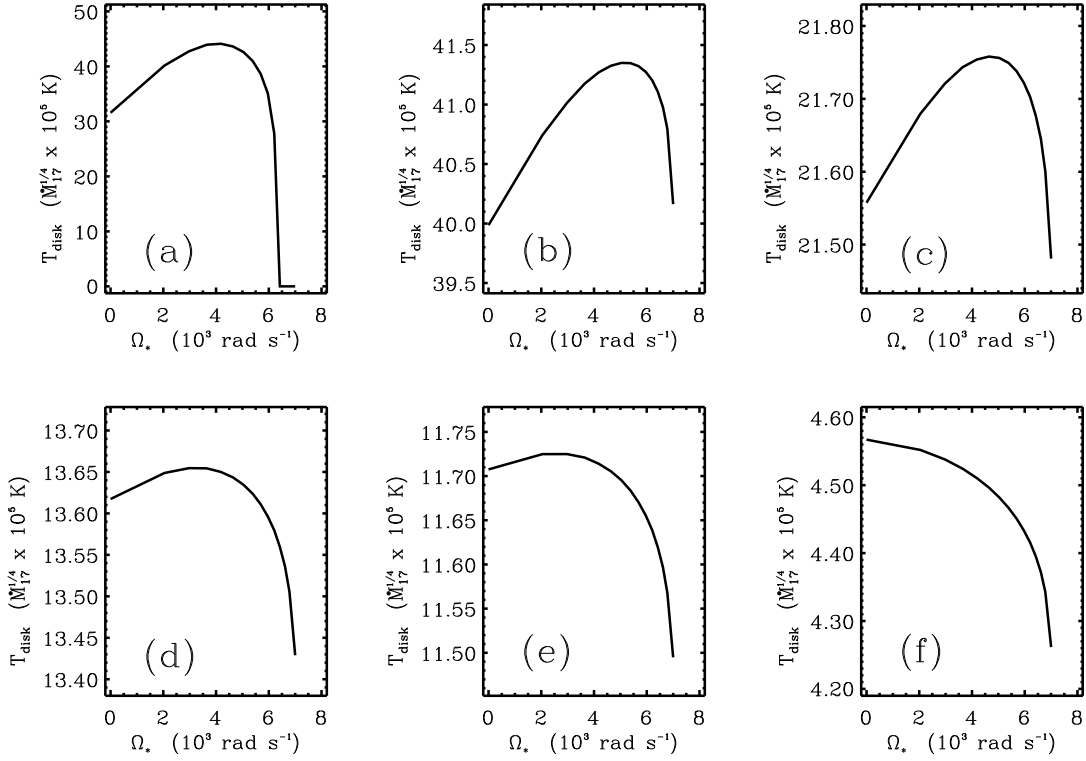


Figure 3.9: Plots of T_{disk} vs. Ω_* at various chosen radial distances: (a) $r = 13 \text{ km}$, (b) $r = 35 \text{ km}$, (c) $r = 100 \text{ km}$, (d) $r = 200 \text{ km}$, (e) $r = 250 \text{ km}$ and (f) $r = 1000 \text{ km}$. These are for EOS model (B), an assumed gravitational mass value of $1.4 M_{\odot}$. and the same values of η , β , h/r and n as in Fig. 3.8 are used.

Chapter 4

Disk Temperature Profile: Implications for Five LMXB Sources

4.1 Introduction

We have calculated the disk temperature profile for a rapidly rotating neutron star in the previous chapter. We have also computed the disk luminosity and the boundary layer luminosity. In this chapter, we compare our theoretical results with the *EXOSAT* data (analysed by White, Stella & Parmar 1988) to constrain different properties of five LMXB sources: Cygnus X-2, XB 1820-30, GX 17+2, GX 9+1 and GX 349+2.

XB 1820-30 is an atoll source which shows type I X-ray bursts. Cygnus X-2, GX 17+2 and GX 349+2 are Z sources, of which the first two show X-ray bursts. GX 9+1 is an atoll source. As all of them are LMXBs (van Paradijs 1995), the magnetic field of the neutron stars are believed to have decayed to low values ($\sim 10^8$ G; see Bhattacharya & Datta 1996 and Bhattacharya & van den Heuvel 1991). Therefore, we ignore the effect of the magnetic field on the accretion disk structure in our calculations.

In this chapter, we calculate the allowed ranges of several properties of these LMXBs and make general comments on the rotation rates of the neutron stars in these systems. We also discuss possible constraints on the neutron star equation of state.

In section 4.2, we describe the procedure of comparison of theoretical values of the parameters with the observed ones. We give the results in section 4.3 and the conclusions in section 4.4.

4.2 Procedure of Comparison with Observations

As mentioned in Chapter 3, the X-ray spectrum from an LMXB may have two contributions: one from the optically thick disk and the other from the boundary layer near the neutron star surface. The spectral shape of the disk emission depends on the accretion rate. For $\dot{M} \ll 10^{17} \text{ g s}^{-1}$, the opacity in the disk is dominated by free-free absorption and the spectrum will be a sum of blackbody spectra from different radii. The local spectrum (with respect to a co-moving observer) will be characterized by a temperature $T_{\text{eff}}(r)$ at that radius. The observer at a large distance will see a temperature $T_{\text{obs}}(r)$, which includes the effect of gravitational redshift and Doppler broadening, as mentioned in section 3.2.1. At higher accretion rates ($\dot{M} \approx 10^{17} \text{ g s}^{-1}$) the opacity will be dominated by Thomson scattering and the spectrum from the disk will be that of a modified blackbody (Shakura & Sunyaev 1973). However, for still higher accretion rates Comptonization in the upper layer of the disk becomes important leading to a saturation of the local spectrum forming a Wien peak. The emergent spectrum can then be described as a sum of blackbody emissions but at a temperature different from T_{obs} . The temperature inferred by a distant observer from the spectrum is the color temperature T_{col} . In general $T_{\text{col}} = f(r)T_{\text{obs}}$ where the function f is called the color factor (or the spectral hardening factor), and it depends on the vertical structure of the disk. Shimura & Takahara (1995) calculated the color factor for various accretion rates and masses of the accreting compact object (black hole) and found that $f \approx (1.8\text{--}2.0)$ is nearly independent of accretion rate and radial distance, for $\dot{M} \sim \dot{M}_e$, where $\dot{M}_e = 1.4 \times 10^{17} M/M_{\odot} \text{ g s}^{-1}$. These authors find that for accretion rate $\sim 10\%$ of \dot{M}_e , $f \approx 1.7$. More recently, however, from the analysis of high-energy radiation from GRO J1655-40, a black-hole transient source observed by RXTE, Borozdin et al. (1999) obtain a value of $f = 2.6$, which is higher than previous estimates used in the literature. With this approximation for T_{col} , the spectrum from optically thick disks with high accretion rates can be represented as a sum of diluted blackbodies. The local flux at each radius is

$$F_{\nu} = \frac{1}{f^4} \pi B_{\nu}(fT_{\text{eff}}) \quad (4.1)$$

where B_{ν} is the Planck function. For high accretion rates the boundary layer at the neutron star surface is expected to be optically thick and an additional single component blackbody spectrum should be observed.

White et al. (1988) have fitted the observed data for the said LMXB sources to several spectral models. One of the models is a blackbody emission upto the innermost stable circular orbit of the accretion disk and an additional blackbody spectrum to account for the boundary layer emission. The spectrum from such a disk is the sum of blackbody emission with a temperature profile

$$T \propto r^{-3/4} (1 - (r_{\text{in}}/r)^{1/2})^{1/4}. \quad (4.2)$$

White et al. (1988) have identified this temperature as the effective temperature which, as mentioned by them, is inconsistent since the accretion rates for these sources are high. However, as mentioned above, identifying this temperature profile as the color temperature makes the model consistent if the color factor is nearly independent of radius. Moreover, the inferred temperature profile (i.e., $T_{\text{obs}} = T_{\text{col}}/f$) is similar to the one developed in previous chapter. Therefore, in this chapter we assume that the maximum of the best-fit color temperature profile $T_{\text{col}}^{\text{max}}$ is related to the maximum temperature $T_{\text{obs}}^{\text{max}}$ computed in previous chapter by ($T_{\text{col}}^{\text{max}} \approx fT_{\text{obs}}^{\text{max}}$). Shimura & Takahara (1988) suggested a value of 1.85 for the factor f , for an assumed neutron star mass equal to $1.4 M_{\odot}$ and $\dot{M} = 10\dot{M}_e$.

We compare the best-fit values of the parameters maximum color temperature ($T_{\text{col}}^{\text{max}}$), disk luminosity (L_{D}) and boundary layer luminosity (L_{BL}) with their theoretical values for a given neutron star mass, accretion rate (\dot{M}), color factor f and equation of state. However, in order to make allowance for the uncertainties in the fitting procedure and in the value of z , and also those arising due to the simplicity of the model, we consider a range of acceptable values for $T_{\text{col}}^{\text{max}}$, L_{D} and L_{BL} . In particular, we allow for deviations in the best-fit values of $T_{\text{col}}^{\text{max}}$ and luminosities: we take two combinations of these, namely, (10%, 25%) and (20%, 50%), where the first number in parentheses corresponds to the error in $T_{\text{col}}^{\text{max}}$ and the second to the error in the best-fit luminosities. Note that we neglect the irradiation temperature here, as $T_{\text{disk}} \approx T_{\text{eff}}$ at the inner region of the disk (the region where the disk temperature reaches a maximum). We obtain a range of consistent values for \dot{M} , Ω_* and f (and hence, allowed ranges of different quantities). The procedure is as follows.

We can calculate the different quantities (E_{D} , E_{BL} , $T_{\text{obs}}^{\text{max}}$, R , r_{in} , etc.) as functions of Ω_* . Taking the observed (or fitted) values for $T_{\text{col}}^{\text{max}}$, L_{BL} and $(L_{\text{BL}} + L_{\text{D}})$ with the error bars, we have two limiting values for each of these quantities. We assume a particular value for each of f and \dot{M} , from which we obtain the corresponding fitted values of $T_{\text{obs}}^{\text{max}}$, E_{BL} and $(E_{\text{BL}} + E_{\text{D}})$ by the relations $E_{\text{BL}} = L_{\text{BL}}/\dot{M}$, $E_{\text{BL}} + E_{\text{D}} = (L_{\text{BL}} + L_{\text{D}})/\dot{M}$ and $T_{\text{obs}}^{\text{max}} = T_{\text{col}}^{\text{max}}/(f\dot{M}^{1/4})$ (because here $T_{\text{obs}}^{\text{max}}$ is in the unit of $\dot{M}^{1/4}$). By interpolation, we calculate two corresponding limiting Ω_* 's (i.e., the allowed range in Ω_*) for each fitted quantity. We take the common region of these three ranges, which is the net allowed range in Ω_* . We do this for \dot{M} 's in the range $10^{-13} M_{\odot}y^{-1}$ to $10^{-6} M_{\odot}y^{-1}$ (which is reasonable for LMXB's) with logarithmic interval 0.0001, for a particular value of f . If for some \dot{M} , there is no allowed Ω_* , then that value of \dot{M} is not allowed. Thus we get the allowed range of \dot{M} for a particular f . Next we repeat the whole procedure described above for various values of f , in the range 1 to 10. If for some f , there is no allowed \dot{M} , then that f is not allowed. Thus we get an allowed range of f . Taking the union of all the allowed ranges of \dot{M} , we get the net

allowed range of \dot{M} (and similarly the net allowed range of Ω_*) for a particular EOS, gravitational mass and a set of error bars. The allowed ranges of ν_{in} , R , $r_{\text{eff}}^{\text{max}}$ etc. then easily follow, since their general variations with respect to Ω_* are already known.

4.3 The Results

In this chapter, we calculate gravitational mass sequences for different EOS models (mentioned in Chapter 2) and constrain several properties of five LMXB sources. For the neutron star in each of the sources, we assume $M = 1.4 M_{\odot}$ (i.e., the canonical mass value for neutron stars). For Cygnus X-2, we assume an additional mass value (1.78), which is the estimated mass for the neutron star in Cygnus X-2 (Orosz & Kuulkers 1999). It may be noted with caution (Haberl & Titarchuk 1995), that this value is not confirmed from X-ray burst spectral analysis. We use the value of $M = 1.78 M_{\odot}$ for the illustration of our results, and leave the issue for future confirmation. We take $\cos i = 0.5$ (i is the inclination angle of the source) for Cygnus X-2 (Orosz & Kuulkers 1999), while for each of other four sources, we use two values for $\cos i$, namely, 0.2 and 0.8. These two widely different values ensure the sufficient generality of our results.

For the source Cygnus X-2, the best spectral fit to the data is when $T_{\text{col}}^{\text{max}} = 1.8 \times 10^7$ K, $L_{\text{D}} = 2.1 \times 10^{38}$ ergs s $^{-1}$ and $L_{\text{BL}} = 2.8 \times 10^{37}$ ergs s $^{-1}$ (White et al. 1988). For the other four sources, the best-fit values of the parameters $T_{\text{col}}^{\text{max}}$, L_{D} and L_{BL} are respectively as follow (White et al. 1988): (1) XB 1820-30: 1.59×10^7 K, (1.49×10^{38} ergs s $^{-1}$, 0.37×10^{38} ergs s $^{-1}$) and 2.56×10^{37} ergs s $^{-1}$; (2) GX 17+2: 1.76×10^7 K, (6.49×10^{38} ergs s $^{-1}$, 1.62×10^{38} ergs s $^{-1}$) and 7.10×10^{37} ergs s $^{-1}$; (3) GX 9+1: 2.25×10^7 K, (6.01×10^{38} ergs s $^{-1}$, 1.50×10^{38} ergs s $^{-1}$) and 2.50×10^{37} ergs s $^{-1}$; (4) GX 349+2: 2.07×10^7 K, (8.54×10^{38} ergs s $^{-1}$, 2.14×10^{38} ergs s $^{-1}$) and 4.80×10^{37} ergs s $^{-1}$. Here the first term in the bracket is L_{D} for $\cos i = 0.2$ and the second term is that for $\cos i = 0.8$.

We take the distance (D) of the source as 8 kpc (Orosz & Kuulkers 1999) for Cygnus X-2 and 6.4 kpc (Bloser et al. 2000) for XB 1820-30. We assume $D = 8$ kpc for both GX 17+2 and GX 9+1, as their locations are believed to be near the galactic center (Deutsch et al. 1999; Hertz et al. 1990) and distance of the galactic center is 7.9 ± 0.3 kpc, as concluded by McNamara et al. (2000). For GX 349+2, we take $D = 9$ kpc (Deutsch et al. 1999).

We display the constrained values with the help of five tables. In Table 4.1 (for Cygnus X-2), we have taken two values of M (but a fixed value for i), while in each of the other four tables, we use a fixed value for M (but two values of i). From these results, we notice that the accretion rates of all the sources are very high. It is to be noted that here \dot{M} is presented in unit of \dot{M}_e (defined in the

previous section). The Eddington accretion rate (\dot{M}_{Edd}) is \dot{M}_e/η , with $\eta = E_{\text{BL}} + E_{\text{D}}$. Therefore, as the actual value of η is much less than 1.0 (generally not greater than 0.3 and for rapidly rotating neutron star, typically less than 0.2), the value of (\dot{M}_{Edd}) is much higher than \dot{M}_e .

The EOS model A is the softest in the sample. The maximum mass of neutron stars (at $\Omega_* = \Omega_{\text{ms}}$) corresponding to this EOS is $1.63 M_{\odot}$. So the constraint results for Cygnus X-2, using this EOS are done only for $M = 1.4 M_{\odot}$.

We notice that the allowed ranges (combined for all the cases considered in each of the tables) of $\Omega_*/\Omega_{\text{ms}}$ are $0.97 - 1.00$, $0.93 - 1.00$ and $0.75 - 1.00$ for the three sources Cygnus X-2, GX 9+1 and GX 349+2 respectively (see Table 3.1 for the mass-shed limit values). Therefore the neutron stars in these three sources can be concluded to be rapidly rotating in general. In the next section, we will discuss the significance of the obtained results.

4.4 Summary and Discussion

In this chapter, we have constrained the values of several properties of five LMXB sources. For all of them, the accretion rates come out to be very high (always $\geq 0.5 \dot{M}_e$). This is in accord with the fact that these are very luminous sources.

From our results, it can be concluded that the neutron star in Cygnus X-2 is rotating very rapidly. The rotation rate of the neutron star in each of the other four sources is also very close to the mass-shed limit for $\cos i = 0.2$. This is because the values of $L_{\text{BL}}/L_{\text{D}}$ are very low for these cases (see Chapter 3). But, for $\cos i = 0.8$, rotation rate can not be constrained effectively for the sources XB 1820-30 and GX 17+2. Therefore, for these two sources, no general conclusion (about the values of Ω_*) can be drawn. However, as mentioned in the previous section, rotation rate can be concluded to be very rapid for the sources GX 9+1 and GX 349+2.

According to Shimura & Takahara (1988), the spectrum from the disk can be represented as a multi-color blackbody only if $\dot{M} > 0.1\dot{M}_e$, which always comes out to be the case for all the chosen LMXBs. Our calculated allowed ranges for f are in accord with the results ($f \sim 1.7 - 2.0$) obtained by Shimura & Takahara (1995). However, if we take the value of $f = 2.6$, as reported by Borozdin et al. (1999), then for Cygnus X-2, one would require an EOS model that is stiffer than the stiffest used here, or a mass greater than $M = 1.78 M_{\odot}$ (if one uses the narrower limits on the luminosity and color temperature). On the other hand, if one were to use the broader limits, the hardening factor $f = 2.6$ is disallowed only by the softest EOS model. For the other four sources, the assumption $f = 2.6$ would require a very stiff EOS model or a mass greater than $M = 1.4 M_{\odot}$ for most of the cases with $\cos i = 0.2$.

High frequency quasi periodic oscillations (kHz QPO) have been observed for four (Cygnus X-2, XB 1820-30, GX 17+2 and GX 349+2) of the chosen sources. The observed maximum kHz QPO frequencies are 1.005 kHz (Cygnus X-2), 1.100 kHz (XB 1820-30), 1.080 kHz (GX 17+2) and 1.020 kHz (GX 349+2) (van der Klis 2000). Now, the maximum possible frequency (i.e., the shortest time scale) of such a system should be given by the rotational frequency in innermost stable circular orbit (ISCO) (ν_{in} ; col. 5 of the tables), unless the model invoked to explain the temporal behavior predicts a substantial power in the second harmonic, i.e., $\nu_{\text{QPO}} \approx 2\nu_{\text{in}}$. Therefore, the stiffest EOS model D is unfavored for Cygnus X-2, as the maximum value of ν_{in} (= 0.938 kHz, Table 4.1) is less than the observed maximum kHz QPO frequency. For the same reason, EOS model D is unfavored for $\cos i = 0.2$ for the sources XB 1820-30 and GX 17+2. It can also be seen from Table 4.3 that if we use only the narrower limits on the luminosities and color temperature, EOS model D (for $\cos i = 0.8$) and EOS model C (for $\cos i = 0.2$) are not likely to be the correct EOS for GX 17+2. The same is true for model D for the source GX 349+2. As we also see from Table 4.4, EOS model C is unfavored for $\cos i = 0.2$ for this source. Further, the neutron star mass estimate in Cygnus X-2 ($\approx 1.78M_{\odot}$, Orosz & Kuulkers 1998) is not consistent with the soft EOS model A. Our analysis, therefore, favors neutron star EOS models which are intermediate in the stiffness parameter values.

We have ignored the magnetic fields of the neutron stars in our calculations. Therefore, the necessary condition for the validity of our results is that the Alfvén radius (r_A) be less than the radius of the inner edge of the disk. This condition will always be valid if $R > r_A$ holds. Here r_A is given by (Shapiro & Teukolsky 1983),

$$r_A = 2.9 \times 10^8 \left(\frac{\dot{M}}{\dot{M}_e} \right)^{-2/7} \mu_{30}^{4/7} \left(\frac{M}{M_{\odot}} \right)^{-3/7} \quad (4.3)$$

where M is the mass of the neutron star, μ_{30} is the magnetic moment in unit of 10^{30} G cm³ and r_A is in cm. With typical values of the parameters for the chosen sources ($R = 10$ km, $M = 1.4M_{\odot}$ and $\dot{M} = 10\dot{M}_e$), the upper limit of the neutron star surface magnetic field comes out to be about 2×10^8 G. Therefore, our results are in general valid for the neutron star magnetic field upto of the order of 10^8 G. This is a reasonable value for the magnetic field of neutron stars in LMXBs, as mentioned in section 4.1. However, this estimate of low magnetic field is based on the assumption of its dipolar form. If the magnetic field geometry contains higher order components, then the field-strength may be higher than the estimated value.

In our analysis, we have assumed that the boundary layer between the disk and the neutron star surface does not affect the inner regions of the disk. This will be a valid approximation when the boundary layer luminosity is smaller than the disk luminosity, and the boundary layer extent is

small compared to the radius of the star. The first part of this condition is true for all the chosen LMXBs, as we see from the previous section. We now show that the second part is also true for the source Cygnus X-2. The flux received at the earth from this region is

$$F_{\text{BL}} = \left(2\pi R \frac{\Delta R}{D^2} \right) \cos i \left(\frac{\sigma T_{\text{BL}}^4}{\pi} \right) \quad (4.4)$$

where ΔR is the width of the boundary layer, $D = 8 \text{ kpc}$ is the distance to the source, $i = 60^\circ$ is the inclination angle and T_{BL} is the effective temperature. Spectral fitting gives a best-fit value for $F_{\text{BL}} \approx 4 \times 10^{-9} \text{ ergs sec}^{-1} \text{ cm}^{-2}$ and $T_{\text{BL}} = T_{\text{col(BL)}}/f_{\text{BL}} = 2.88/f_{\text{BL}} \text{ keV}$, where f_{BL} is the color factor for the boundary layer and $T_{\text{col(BL)}}$ is the color temperature of the boundary layer. Using these values, we get $\Delta R \approx 0.2 f_{\text{BL}}^4 \text{ km}$, which is indeed smaller than R provided the boundary layer color factor f_{BL} is close to unity. This is supported by the work of London, Taam & Howard (1986) and Ebisuzaki (1987), who obtain $f_{\text{BL}} \approx 1.5$. The same conclusion can be drawn for other four chosen sources, as their parameter values are similar to those for Cygnus X-2.

We have not attempted to model the observed temporal behavior of the sources, and in particular, the QPO observations. Beat frequency model identifies the peak separation of the two observed kHz QPOs with the neutron star spin rate. For example, for Cygnus X-2 the observed peak separation is $\Delta\nu = 346 \pm 29 \text{ Hz}$ (Wijnands et al. 1998) which is smaller than the typical rotation frequencies calculated here. However, a pure beat-frequency model has been called into question due to several observations. For instance, $\Delta\nu$ has been observed to vary by about 40% for Sco X-1 (van der Klis et al. 1997) and the kHz QPO frequencies have been found to be correlated with the break frequency ($\approx 20 \text{ Hz}$) of the power spectrum density. Inclusion of an alternate model, where the QPOs are suggested to originate due to non-Keplerian motion of matter in the disk (Titarchuk & Osherovich 1999; Osherovich & Titarchuk 1999a; Osherovich & Titarchuk 1999b; Titarchuk, Osherovich & Kuznetsov 1999), into the framework of the calculations mentioned in this work require a new formulation within the space-time geometry chosen herein.

In this chapter, we have calculated the allowed ranges of several quantities for five LMXBs, which give valuable information about these systems. Such information will be helpful to understand their temporal behaviors. Besides, LMXBs are believed to be the progenitors of the millisecond pulsars. This is in accord with our result that the neutron stars in Cygnus X-2, GX 9+1 and GX 349+2 are rapidly rotating. However, the data from the present and the future generation X-ray satellites (*Chandra*, *XMM*, *Constellation-X* etc.) with better spectral resolutions (compared to those of earlier satellites) will make better use (i.e., to get best-fit values of Ω_* and to constrain EOS models) of the general relativistic model presented here.

EOS	M M_{\odot}	f	ν_* kHz	ν_{in} kHz	R km	$r_{\text{eff}}^{\text{max}}$ km	\dot{M} \dot{M}_e	
(A)	1.4	L	1.37[1.16]	1.753[1.743]	1.755[1.755]	11.3[10.7]	16.0[15.6]	11.2[5.8]
		U	1.99[2.56]	1.755[1.755]	1.787[1.944]	11.4[11.4]	16.1[16.1]	22.9[27.5]
(B)	1.4	L	1.53[1.29]	1.106[1.087]	1.132[1.123]	15.2[14.3]	21.0[20.0]	13.8[7.2]
		U	2.18[2.74]	1.112[1.113]	1.177[1.285]	15.6[15.6]	21.5[21.6]	27.0[33.5]
(C)	1.4	L	1.57[1.33]	0.964[0.945]	0.975[0.971]	16.8[15.6]	23.1[21.7]	14.9[7.7]
		U	2.24[2.81]	0.968[0.968]	1.015[1.134]	17.2[17.2]	23.6[23.7]	29.3[36.5]
(D)	1.4	L	1.67[1.42]	0.736[0.719]	0.745[0.742]	20.1[18.6]	27.6[25.7]	17.5[9.1]
		U	2.38[2.97]	0.740[0.740]	0.779[0.876]	20.7[20.7]	28.3[28.4]	34.6[42.4]
(B)	1.78	L	1.58[1.33]	1.303[1.292]	1.322[1.315]	14.8[14.2]	21.2[20.7]	8.9[4.7]
		U	2.28[2.91]	1.307[1.307]	1.361[1.462]	15.1[15.1]	21.4[21.4]	17.2[21.4]
(C)	1.78	L	1.65[1.39]	1.081[1.067]	1.086[1.085]	17.1[16.2]	23.8[23.0]	9.8[5.1]
		U	2.39[3.01]	1.083[1.083]	1.109[1.209]	17.3[17.3]	24.0[24.1]	19.3[24.0]
(D)	1.78	L	1.74[1.47]	0.806[0.791]	0.817[0.813]	20.6[19.2]	28.6[27.1]	11.4[6.0]
		U	2.50[3.15]	0.809[0.809]	0.848[0.938]	21.1[21.1]	29.1[29.2]	22.2[27.7]

Table 4.1: Observational constraints for various EOS models: (A), (B), (C), (D) for the source Cygnus X-2. L and U stand for lower and upper limits. The parameters are f (color factor), ν_* (rotational frequency of the neutron star), ν_{in} (rotational frequency in the ISCO), R (equatorial radius of the neutron star), $r_{\text{eff}}^{\text{max}}$ (radius where the effective temperature of the disk is maximum) and \dot{M} (the accretion rate). The limits are for 25% uncertainty in luminosities and 10% uncertainty in the color temperature. Values in brackets are for 50% uncertainty in luminosities and 20% uncertainty in the color temperature. For EOS model A, the mass of the neutron star cannot exceed $1.63 M_{\odot}$ hence the $1.78M_{\odot}$ solution is not presented. The accretion rate is given in unit of $\dot{M}_e = 1.4 \times 10^{17} M/M_{\odot} \text{ g s}^{-1}$, where M is the neutron star mass.

EOS	$\cos i$	f	ν_* kHz	ν_{in} kHz	R km	$r_{\text{eff}}^{\text{max}}$ km	\dot{M} \dot{M}_e	
(A)	0.2	L	1.31[1.10]	1.751[1.726]	1.756[1.756]	11.2[10.2]	18.6[18.1]	7.7[3.8]
		U	1.91[2.41]	1.755[1.755]	1.819[2.078]	11.4[11.4]	18.7[18.7]	16.1[20.3]
(B)	0.2	L	1.45[1.30]	1.103[1.059]	1.137[1.126]	15.0[13.7]	23.0[21.6]	9.7[4.5]
		U	2.07[2.61]	1.112[1.113]	1.197[1.372]	15.5[15.6]	23.5[23.6]	19.4[24.4]
(C)	0.2	L	1.49[1.30]	0.961[0.913]	0.979[0.973]	16.5[15.0]	24.8[23.1]	10.4[4.9]
		U	2.12[2.71]	0.968[0.968]	1.042[1.206]	17.2[17.2]	25.5[25.6]	21.2[26.7]
(D)	0.2	L	1.59[1.40]	0.735[0.687]	0.748[0.743]	19.9[17.7]	29.1[26.5]	12.2[5.6]
		U	2.25[2.81]	0.740[0.740]	0.795[0.941]	20.6[20.7]	30.0[30.1]	25.0[31.4]
(A)	0.8	L	1.79[1.50]	1.463[0.000]	1.822[1.571]	9.9[7.5]	18.1[18.1]	1.2[0.5]
		U	3.06[4.70]	1.751[1.754]	2.165[2.165]	11.2[11.4]	20.4[22.3]	4.5[6.4]
(B)	0.8	L	1.94[1.71]	0.498[0.000]	1.207[1.152]	11.3[11.0]	20.2[20.2]	1.4[0.9]
		U	3.22[4.20]	1.102[1.110]	1.782[1.782]	14.9[15.4]	22.9[23.4]	5.6[7.9]
(C)	0.8	L	1.99[1.70]	0.175[0.000]	1.046[0.991]	12.3[12.3]	21.5[21.0]	1.5[1.0]
		U	3.36[4.02]	0.960[0.966]	1.573[1.568]	16.5[17.0]	24.7[25.4]	6.1[8.5]
(D)	0.8	L	2.11[1.80]	0.000[0.000]	0.806[0.758]	14.7[14.7]	23.1[23.1]	1.8[1.2]
		U	3.30[3.90]	0.733[0.739]	1.212[1.212]	19.7[20.5]	28.9[29.8]	7.2[9.9]

Table 4.2: Observational constraints for various EOS models : (A), (B), (C), (D) for the source XB 1820-30. The mass of the neutron star is assumed to be $1.4 M_{\odot}$. Other specifications are same as in Table 4.1.

EOS	$\cos i$	f	ν_* kHz	ν_{in} kHz	R km	$r_{\text{eff}}^{\text{max}}$ km	\dot{M} \dot{M}_e	
(A)	0.2	L	1.01[1.00]	1.754[1.748]	1.756[1.756]	11.4[11.0]	18.7[18.5]	36.1[19.8]
		U	1.43[1.82]	1.755[1.755]	1.773[1.869]	11.4[11.4]	18.7[18.7]	68.7[82.6]
(B)	0.2	L	1.12[1.00]	1.108[1.097]	1.128[1.122]	15.3[14.7]	23.3[22.6]	44.4[24.4]
		U	1.57[1.96]	1.113[1.113]	1.163[1.236]	15.6[15.7]	23.6[23.6]	82.6[101.7]
(C)	0.2	L	1.15[1.00]	0.966[0.954]	0.974[0.971]	16.9[16.0]	25.2[24.2]	47.5[26.1]
		U	1.62[2.01]	0.968[0.968]	1.000[1.091]	17.2[17.2]	25.5[25.6]	88.5[111.5]
(D)	0.2	L	1.22[1.03]	0.738[0.728]	0.744[0.742]	20.3[19.2]	29.7[28.3]	55.9[30.7]
		U	1.72[2.13]	0.740[0.740]	0.766[0.849]	20.7[20.7]	30.1[30.1]	106.4[131.0]
(A)	0.8	L	1.39[1.20]	1.702[0.000]	1.782[1.571]	9.9[7.5]	18.1[18.1]	6.6[2.0]
		U	2.20[3.72]	1.754[1.755]	2.166[2.165]	11.3[11.4]	18.6[22.3]	18.5[25.5]
(B)	0.8	L	1.53[1.31]	1.009[0.000]	1.172[1.141]	13.1[11.0]	21.1[20.2]	7.7[3.2]
		U	2.31[3.35]	1.107[1.111]	1.463[1.782]	15.2[15.5]	23.2[23.5]	22.8[30.7]
(C)	0.8	L	1.61[1.30]	0.858[0.000]	1.010[0.983]	14.3[12.3]	22.4[21.0]	8.3[3.6]
		U	2.33[3.20]	0.965[0.967]	1.289[1.568]	16.8[17.1]	25.1[25.4]	25.0[32.9]
(D)	0.8	L	1.66[1.41]	0.631[0.000]	0.775[0.750]	16.8[14.7]	25.4[23.1]	9.5[4.4]
		U	2.47[3.10]	0.737[0.740]	1.011[1.212]	20.2[20.6]	29.5[30.0]	29.3[38.6]

Table 4.3: Observational constraints for various EOS models : (A), (B), (C), (D) for the source GX 17+2. Other specifications are same as in Table 4.2.

EOS	$\cos i$	f	ν_* kHz	ν_{in} kHz	R km	$r_{\text{eff}}^{\text{max}}$ km	\dot{M} \dot{M}_e	
(A)	0.2	L	1.33[1.13]	1.755[1.755]	1.756[1.756]	11.4[11.4]	18.7[18.7]	36.9[22.8]
		U	1.85[2.25]	1.755[1.755]	1.756[1.761]	11.4[11.4]	18.7[18.7]	59.9[72.0]
(B)	0.2	L	1.47[1.24]	1.112[1.110]	1.120[1.117]	15.6[15.4]	23.6[23.4]	43.4[27.4]
		U	2.04[2.49]	1.114[1.114]	1.130[1.147]	15.7[15.7]	23.6[23.7]	73.6[90.6]
(C)	0.2	L	1.51[1.28]	0.968[0.967]	0.970[0.970]	17.2[17.1]	25.5[25.4]	47.5[29.3]
		U	2.09[2.56]	0.968[0.968]	0.975[0.986]	17.3[17.3]	25.6[25.6]	80.7[99.3]
(D)	0.2	L	1.61[1.36]	0.740[0.739]	0.742[0.741]	20.7[20.5]	30.1[29.9]	55.9[34.4]
		U	2.24[2.74]	0.740[0.740]	0.745[0.754]	20.7[20.7]	30.1[30.1]	94.9[116.7]
(A)	0.8	L	1.84[1.61]	1.752[1.728]	1.756[1.756]	11.2[10.3]	18.6[18.1]	7.9[3.8]
		U	2.69[3.52]	1.755[1.755]	1.815[2.064]	11.4[11.4]	18.7[18.7]	16.5[20.3]
(B)	0.8	L	2.05[1.80]	1.103[1.064]	1.136[1.126]	15.0[13.8]	22.9[21.7]	9.7[4.6]
		U	2.92[3.72]	1.112[1.113]	1.200[1.361]	15.5[15.6]	23.5[23.6]	19.4[24.4]
(C)	0.8	L	2.10[1.80]	0.961[0.919]	0.978[0.972]	16.5[15.0]	24.8[23.2]	10.4[5.0]
		U	3.00[3.81]	0.968[0.968]	1.041[1.195]	17.2[17.2]	25.5[25.6]	21.2[26.7]
(D)	0.8	L	2.24[1.92]	0.734[0.692]	0.748[0.743]	19.8[17.8]	29.0[26.7]	12.2[5.7]
		U	3.19[4.00]	0.740[0.740]	0.802[0.932]	20.6[20.7]	30.0[30.1]	25.0[31.4]

Table 4.4: Observational constraints for various EOS models : (A), (B), (C), (D) for the source GX 9+1. Other specifications are same as in Table 4.2.

EOS	$\cos i$	f	ν_* kHz	ν_{in} kHz	R km	$r_{\text{eff}}^{\text{max}}$ km	\dot{M} \dot{M}_e	
(A)	0.2	L	1.12[1.00]	1.755[1.754]	1.756[1.756]	11.4[11.4]	18.7[18.7]	50.9[30.7]
		U	1.55[1.92]	1.755[1.755]	1.756[1.771]	11.4[11.4]	18.7[18.7]	86.4[103.9]
(B)	0.2	L	1.24[1.04]	1.112[1.109]	1.122[1.119]	15.5[15.3]	23.5[23.3]	61.2[37.7]
		U	1.72[2.11]	1.113[1.114]	1.137[1.159]	15.7[15.7]	23.6[23.7]	106.3[130.8]
(C)	0.2	L	1.27[1.08]	0.968[0.966]	0.971[0.970]	17.2[17.0]	25.5[25.3]	67.1[40.4]
		U	1.76[2.17]	0.968[0.968]	0.979[1.000]	17.2[17.3]	25.6[25.6]	116.6[140.1]
(D)	0.2	L	1.35[1.14]	0.740[0.738]	0.742[0.741]	20.6[20.4]	30.0[29.7]	78.8[47.5]
		U	1.88[2.31]	0.740[0.740]	0.748[0.765]	20.7[20.7]	30.1[30.1]	136.9[168.5]
(A)	0.8	L	1.55[1.34]	1.748[1.678]	1.760[1.756]	11.0[9.7]	18.4[18.1]	10.6[4.5]
		U	2.29[3.10]	1.755[1.755]	1.879[2.147]	11.4[11.4]	18.7[18.7]	23.3[30.0]
(B)	0.8	L	1.71[1.50]	1.096[0.955]	1.148[1.129]	14.6[12.7]	22.6[20.7]	13.1[5.2]
		U	2.47[3.22]	1.110[1.112]	1.244[1.532]	15.4[15.6]	23.4[23.6]	28.0[36.0]
(C)	0.8	L	1.76[1.53]	0.953[0.798]	0.984[0.974]	16.0[13.8]	24.2[21.9]	14.0[5.6]
		U	2.54[3.30]	0.967[0.968]	1.093[1.350]	17.1[17.2]	25.4[25.5]	30.7[38.6]
(D)	0.8	L	1.87[1.61]	0.727[0.557]	0.753[0.744]	19.1[16.2]	28.2[24.6]	16.5[6.3]
		U	2.69[3.40]	0.739[0.740]	0.845[1.069]	20.6[20.7]	29.9[30.1]	36.0[46.4]

Table 4.5: Observational constraints for various EOS models : (A), (B), (C), (D) for the source GX 349+2. Other specifications are same as in Table 4.2.

Chapter 5

General Relativistic Spectra of Accretion Disks around Rotating Neutron Stars

5.1 Introduction

Low Mass X-ray Binaries are believed to harbor black holes or weakly magnetized neutron stars with an accretion disk. The X-ray emission arises from the hot ($\approx 10^7$ K) innermost region of the disk. In the case of a neutron star there will be emission, in addition, from a boundary layer between the accretion disk and neutron star surface. Since the observed emission arises from regions close to a compact object, these sources are possible candidates for studying strong field gravity.

In the standard theory (Shakura & Sunyaev 1973), the accretion disk is assumed to be an optically thick Newtonian one. In this model, the local emergent flux (assumed to be a blackbody) is equated to the energy dissipation at a particular radial point in the disk. The observed spectrum is then a sum of black body components arising from different radial positions in the disk. General relativistic effects modify this Newtonian spectrum in two separate ways. First, the local energy dissipation at a radial point is different from the Newtonian disk, giving rise to a modified temperature profile. Second, the observed spectrum is no longer a sum of local spectra because of effects like Doppler Broadening, gravitational redshifts, and light-bending. Modified spectra, incorporating these effects, but with different approximations have been computed by several authors (e.g. Novikov & Thorne 1973; Asaoka 1989) for accretion disks around rotating (Kerr) black holes. These computations confirm the expected result, that the relativistic spectral shape differs from the Newtonian one by around 10%. Thus, for comparison with observed data with systematic and statistical errors larger than 10%, the Newtonian approximation is adequate. Ebisawa, Mitsuda

and Hanawa (1991) showed that for typical data from the *Ginga* satellite, the relativistic spectrum cannot be differentiated from the Newtonian disk spectrum. They also found that the relativistic spectrum is similar in shape (at the sensitivity level of *Ginga*) to the Comptonized model spectrum. Although, *Ginga* was not sensitive enough to distinguish between the different spectra, better estimates of fit parameters like accretion rate and mass of the compact object were obtained when the data was compared to relativistic spectra rather than the standard Newtonian one.

The present and next generation of satellites (e.g. *ASCA*, *RXTE*, *Chandra*, *XMM*, *Constellation-X*) with their higher sensitivity and/or larger effective area than *Ginga* are expected to differentiate between relativistic and Newtonian spectra from low mass X-ray binaries (LMXB) and black hole systems. However, as pointed out by Ebisawa, Mitsuda and Hanawa (1991), the presence of additional components (e.g. boundary layer emission from the neutron star surface) and smearing effects due to Comptonization may make the detection ambiguous. Nevertheless, the detection of strong gravity effects on the spectra from these sources will be limited by the accuracy of theoretical modeling of accretion disk spectra rather than limitations on the quality of the observed data. Thus, it is timely to develop accurate relativistically corrected spectra for comparison with present and future observations. Apart from the importance of detecting strong gravity effects in the spectra of these sources, such an analysis may also shed light on the geometry and dynamics of innermost regions of accretion disks.

Novikov & Thorne (1973) and Page & Thorne (1974) computed the spectra of accretion disks around rotating (Kerr) black holes. This formalism when directly applied to rotating neutron stars provides only a first order estimate: the absence of an internal solution in the case of Kerr geometry makes it difficult to obtain, in a straightforward manner, the coupling between the mass and the angular momentum of the central accretor. On one hand, this coupling depends on the equation of state of neutron star matter, and on the other hand, it depends on the proper treatment of rotation within general relativity. Equilibrium configurations of rapidly rotating neutron stars for realistic equations of state have been computed in Chapter 2. One crucial feature in all these calculations is that the space-time geometry is obtained by numerically and self-consistently solving the Einstein equations and the equations for hydrostatic equilibrium for a general axisymmetric metric. With the aim of modeling spectra of LMXBs, here we attempt to compute the spectrum of accretion disks around rotating neutron stars within such a space-time geometry. This is particularly important since LMXBs are old (population I) systems and the central accretor in these systems are expected to have large rotation rates (Bhattacharya & van den Heuvel 1991 and references therein).

In section 5.2, we describe the spectrum calculation method, without considering the light-bending effect. This effect is taken into account in section 5.3. We display the results in section

5.4 and draw conclusions in section 5.5.

5.2 Calculation of the Spectrum: Without Light-Bending Effect

The disk spectrum is expressed as:

$$F(E_{\text{ob}}) = (1/E_{\text{ob}}) \int I_{\text{ob}}(E_{\text{ob}}) d\Pi_{\text{ob}} \quad (5.1)$$

where the subscript ‘ob’ denotes the quantity in observer’s frame, the flux F is expressed in photons/sec/cm²/keV, E is photon energy in keV, I is specific intensity and Π is the solid angle subtended by the source at the observer.

As I/E^3 remains unchanged along the path of a photon (see for e.g., Misner et al. 1973), one can calculate I_{ob} , if I_{em} is known (hereafter, the subscript ‘em’ denotes the quantity in emitter’s frame). We assume the disk to emit like a diluted blackbody, so I_{em} is given by

$$I_{\text{em}} = (1/f^4)B(E_{\text{em}}, T_c) \quad (5.2)$$

where f is the color factor of the disk assumed to be independent of radius (e.g. Shimura & Takahara 1995). B is the Planck function and T_c (the temperature in the central plane of the disk) is related to the effective temperature T_{eff} through the relation $T_c = fT_{\text{eff}}$. The effective temperature, T_{eff} is a function of the radial coordinate r and for a rotating accretor is given by Eq. (3.1).

The quantities E_{ob} and E_{em} are related through the expression $E_{\text{em}} = E_{\text{ob}}(1+z)$, where $(1+z)$ contains the effects of both gravitational redshift and Doppler shift. For a general axisymmetric metric (representing the space–time geometry around a rotating neutron star), the factor $(1+z)$ is expressed as (see for example, Luminet 1979)

$$1+z = (1 + \Omega_K b \sin \alpha \sin i)(-g_{tt} - 2\Omega_K g_{t\phi} - \Omega_K^2 g_{\phi\phi})^{-1/2} \quad (5.3)$$

where the $g_{\mu\nu}$ ’s are the metric coefficients and t and ϕ are the time and azimuthal coordinates. In the above expression (which includes light–bending effects), i is the inclination angle of the source ($i = 0$ implies face–on), b the impact parameter of the photon relative to the line joining the source and the observer and α the polar angle of the position of the photon on the observer’s detector plane. For the sake of illustration and simplicity in calculations, here we neglect light-bending. We thus write $b \sin \alpha = r \sin \phi$ and

$$d\Pi_{\text{ob}} = \frac{r dr d\phi \cos i}{D^2} \quad (5.4)$$

where D is the distance of the source from the observer.

For our purpose here, we compute constant gravitational mass sequences (as described in Chapter 3) whose rotation rates vary from zero to the centrifugal mass shed limit (where gravitational forces balance centrifugal forces). For realistic neutron stars, the inner radius r_{in} may be located either at the marginally stable orbit or the surface of the neutron star depending on its central density and rotation rate (see Chapter 3), having important implications for the gravitational energy release as well as the temperature profiles of accretion disks. The procedure of calculating T_{eff} for rapidly rotating neutron stars considering the full effect of general relativity is given in Chapter 3. In Fig. 3.2, it is shown that the difference between Newtonian temperature profile and general relativistic temperature profile is substantial at the inner portion of the disk. As will be shown herein, it turns out that this is the major reason for the difference between Newtonian and general relativistic spectra at high energies.

To summarize this section, we calculate the accretion disk spectrum using Eq. (5.1), taking the radial integration limits as r_{in} and r_{out} and the azimuthal integration limits as 0 and 2π . We choose a very large value ($\approx 10^5$ Schwarzschild radius) for r_{out} .

5.3 Calculation of the Spectrum: With Light-Bending Effect

We describe the calculation of the spectrum, considering light bending effect, in a separate section, because it involves very time consuming numerical computations. Whether such computations are worthwhile to do, we will see that in the next section. Light-bending calculations use the Eqs. (5.1), (5.2) and (5.3). But the elementary solid angle will be given by

$$d\Pi_{\text{ob}} = \frac{b \, db \, d\alpha}{D^2} \quad (5.5)$$

where b , α and D are same parameters, as mentioned in section 2. As we consider the effect of gravity on photon's path, here we need to trace the photon's trajectory numerically. The procedure is described below.

For a configuration, described by M and Ω_* (and thus specified by a set of $g_{\mu\nu}$), we obtain Ω_K . To calculate the spectrum for a given value of i with light bending effects, we backtrack the photon's path from the observer to the disk, using standard ray tracing techniques (e.g. Chandrasekhar 1983) and the relevant boundary conditions. For convenience, we use μ ($= \cos \theta$) instead of θ and s ($= \bar{r}/(A + \bar{r})$) instead of r as the coordinates. Here \bar{r} is the quasi-isotropic radial coordinate. Consequently, the metric (2.3) becomes

$$\begin{aligned}
dS^2 &= -e^{\gamma+\rho} dt^2 + e^{2\alpha} (A^2/(1-s)^4) ds^2 \\
&\quad + A^2 (s/(1-s))^2 (1/(1-\mu^2)) d\mu^2 \\
&\quad + e^{\gamma-\rho} A^2 (s/(1-s))^2 (1-\mu^2) (d\phi - \omega dt)^2
\end{aligned} \tag{5.6}$$

Here, A is a known constant of the dimension of distance. Now it is quite straightforward to calculate the geodesic equations for photons, which are given below.

$$dt/d\lambda = e^{-(\gamma+\rho)} (1 - \omega L) \tag{5.7}$$

$$\begin{aligned}
d\phi/d\lambda &= e^{-(\gamma+\rho)} \omega (1 - \omega L) \\
&\quad + L / (e^{\gamma-\rho} A^2 (s/(1-s))^2 (1 - \mu^2))
\end{aligned} \tag{5.8}$$

$$\begin{aligned}
(ds/d\lambda)^2 &= e^{-2\alpha} ((1-s)^4/A^2) (e^{-(\gamma+\rho)} (1 - \omega L)^2 \\
&\quad - L^2 / (e^{\gamma-\rho} A^2 (s/(1-s))^2 (1 - \mu^2))) \\
&\quad - s^2 (1-s)^2 (1/(1 - \mu^2)) y^2
\end{aligned} \tag{5.9}$$

$$d\mu/d\lambda = y \tag{5.10}$$

$$\begin{aligned}
dy/d\lambda &= -2(\alpha_{,s} + (1/(s(1-s)))) y (ds/d\lambda) \\
&\quad + \alpha_{,\mu} (1/(s(1-s)))^2 (1 - \mu^2) (ds/d\lambda)^2 \\
&\quad - (\alpha_{,\mu} + (\mu/(1 - \mu^2))) y^2 \\
&\quad + ((1/2) e^{\gamma-\rho-2\alpha} (\gamma_{,\mu} - \rho_{,\mu}) (1 - \mu^2)^2 \omega^2 \\
&\quad - e^{\gamma-\rho-2\alpha} \mu (1 - \mu^2) \omega^2 \\
&\quad + e^{\gamma-\rho-2\alpha} (1 - \mu^2)^2 \omega \omega_{,\mu} \\
&\quad - (1/2) e^{\gamma+\rho-2\alpha} (\gamma_{,\mu} + \rho_{,\mu})
\end{aligned}$$

$$\begin{aligned}
 & ((1-s)/(As))^2(1-\mu^2)(dt/d\lambda)^2 \\
 & + e^{\gamma-\rho-2\alpha}(1-\mu^2)^2(-\omega_{,\mu} - \omega(\gamma_{,\mu} - \rho_{,\mu})) \\
 & + 2\omega(\mu/(1-\mu^2))(d\phi/d\lambda)(dt/d\lambda) \\
 & + e^{\gamma-\rho-2\alpha}(1-\mu^2)^2((1/2)(\gamma_{,\mu} - \rho_{,\mu}) \\
 & - \mu/(1-\mu^2))(d\phi/d\lambda)^2
 \end{aligned} \tag{5.11}$$

where, λ is the affine parameter, L is the negative of the ratio of the ϕ -component of the angular momentum and the t -component of the angular momentum of photon and a comma followed by a variable as subscript to a quantity, represents a derivative of the quantity with respect to the variable.

We cover the disk between radii r_{in} and $r_{\text{mid}} = 1000r_g$; r_{in} being the radius of the inner edge of the disk and r_g the Schwarzschild radius (increasing r_{mid} has no significant effect on the spectrum). Beyond r_{mid} , we ignore the effect of light-bending i.e., we take $b \sin \alpha = r \sin \phi$ (ϕ is the azimuthal angle on disk plane) and $d\Pi_{\text{ob}} = (r dr d\phi \cos i) / D^2$ (see section 5.2).

We have performed several consistency checks on our results: (1) by switching off the light-bending effect (i.e. by considering flat space-time while backtracking the photon's path), we see that the spectrum matches very well with that computed by ignoring light-bending effects (calculated by an independent code – section 5.2). Also, in this case, the analytically calculated values of several quantities on the disk plane (e.g. r , ϕ , $d\phi/dt$, $d\theta/dt$ etc.) are reproduced satisfactorily by our numerical method, (2) an increase in the number of grid points on the (b, α) plane do not have any significant effect on the computed spectrum, (3) the spectrum matches very well with the Newtonian spectrum (Mitsuda et al. 1984) at low energy limit. This would imply that for higher frequencies, our spectrum is correct to within 0.2% to 0.3%.

5.4 The Results

We calculate the general relativistic spectrum from the accretion disk around rapidly rotating neutron star, taking into account the light-bending effect. The spectrum is calculated as a function of 6 parameters : M , Ω_* , distance of the source (D), inclination angle (i) (for face-on, $i = 0^\circ$), accretion rate (\dot{M}) and color factor f , for each of the chosen EOS. Our results are displayed in Figs. 5.1 to 5.5. In all the displayed spectra, we have assumed $M = 1.4M_\odot$ (canonical mass for neutron stars), $D = 5$ kpc and $f = 2.0$.

In Fig. 5.1, we have plotted the Newtonian spectrum and GR spectra with (LBGR) and without (NLBGR) light-bending effect, keeping the values of all the parameters same. At 10 keV,

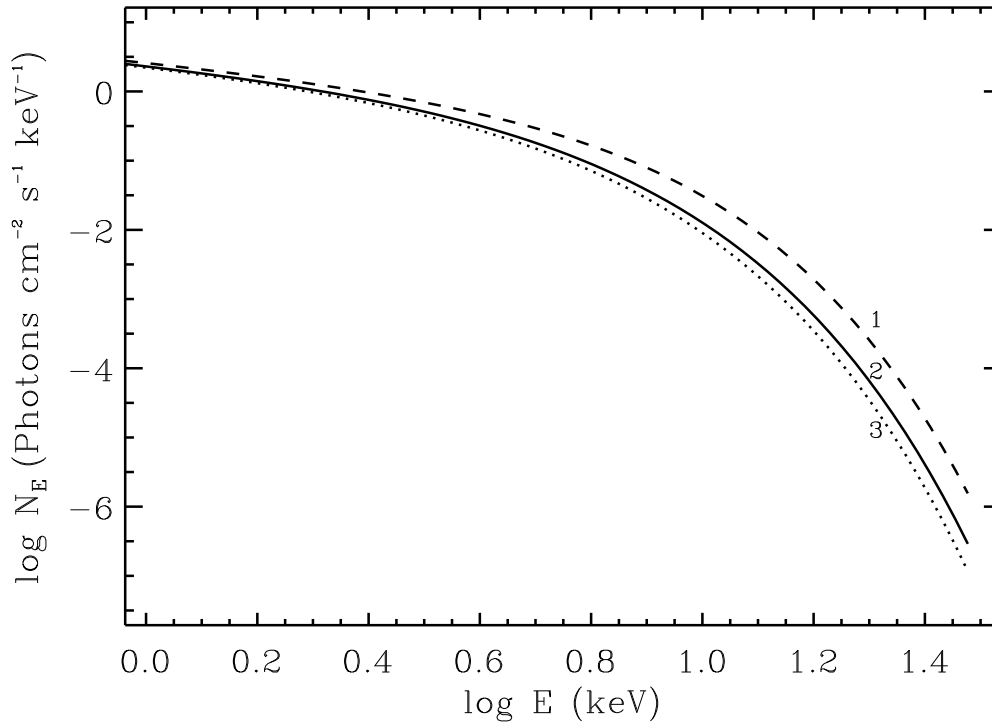


Figure 5.1: Effect of general relativity: spectra from accretion disk around a neutron star of mass $1.4M_{\odot}$. All the curves are for EOS model (B), $\Omega_* = 0$, $D = 5$ kpc, $i = 60^\circ$, $\dot{M} = 10^{18}$ g/sec and $f = 2$. Curve (1) corresponds to the Newtonian case, curve (2) to the general relativistic case including the effect of light-bending and curve (3) to the general relativistic case without considering the effect of light-bending.

the Newtonian flux is almost 2.5 times the LBGR flux. This is quite expected, because in the inner parts of the disk, Newtonian temperature is considerably higher than the GR temperature (see Fig. 3.2). LBGR flux is about 50% higher than NLBGR flux at 10 keV. This is because light-bending causes the disk to subtend a larger solid angle at the observer than otherwise. Thus the general effect of light-bending is to increase the observed flux.

According to Shimura & Takahara (1995), the thin blackbody description of the accretion disk, as adopted in this paper, is valid for $0.1\dot{M}_e < \dot{M} < \dot{M}_{\text{Edd}}$, where $\dot{M}_e \equiv L_{\text{Edd}}/c^2$. Here L_{Edd} is the Eddington luminosity and \dot{M}_{Edd} is the Eddington accretion rate (see Chapter 4 for description). For the purpose of demonstration, we have taken three different values of \dot{M} in this range (for the mass-shed configuration) and plotted the corresponding spectra in Fig. 5.2. As is expected, we see that the high energy part of the spectrum is more sensitive to the value of \dot{M} . It is seen that the spectra for different values of \dot{M} are easily distinguishable.

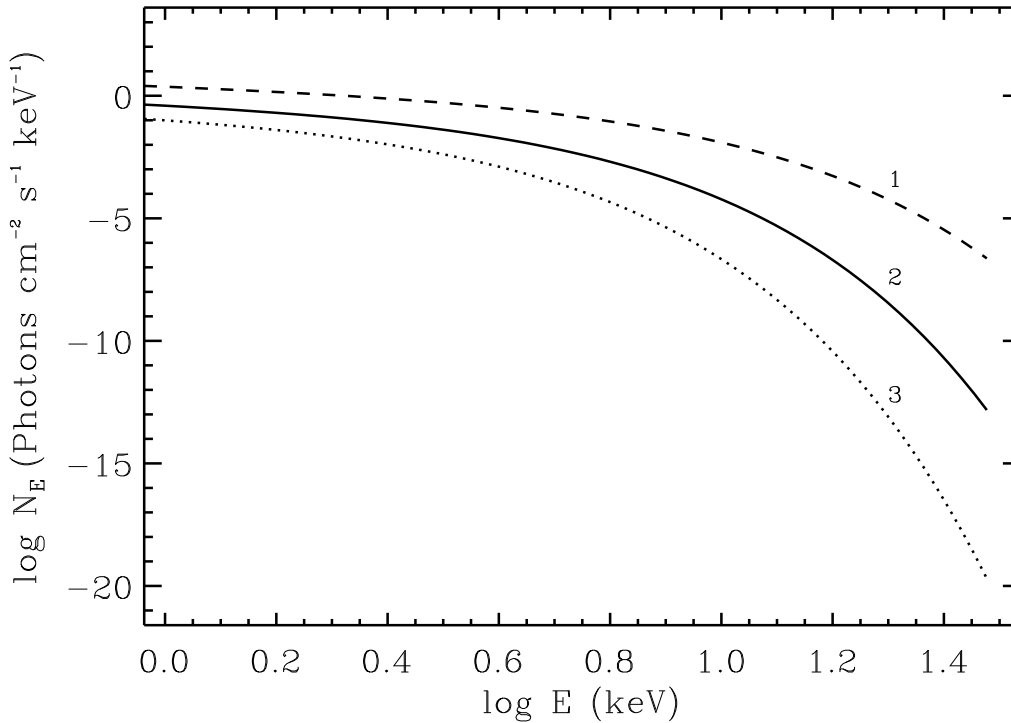


Figure 5.2: Accretion rate dependence: general relativistic spectra including light-bending effects from accretion disk around a neutron star of mass-shed limit configuration ($\Omega_* = 7001$ rad/s). Curve (1) corresponds to $\dot{M} = 10^{18}$ g/sec, curve (2) to $\dot{M} = 10^{17}$ g/sec and curve (3) to $\dot{M} = 2 \times 10^{16}$ g/sec. The values of all the other parameters are as in Fig. 5.1.

The inclination angle i is a very important parameter in determining the shape of the spectrum and its overall normalisation. In Fig. 5.3, we have plotted the spectra for four inclination angles, for the mass-shed configuration. We see that the observed flux at low energies is higher for lower values of i . This is simply due to the projection effect (proportional to $\cos i$). But at higher energies (> 10 keV) this trend is reversed mainly because Doppler effect becomes important. The most energetic photons mainly come from the inner portion of the disk, where the linear speed of accreted matter is comparable to the speed of light. The net effect of Doppler broadening is a net blue shift of the spectrum, as a larger amount of flux comes from the blue-shifted regions than from the red-shifted regions. This is a monotonic trend, but it will be noticed from Fig. 5.3 that the curve for $i = 85^\circ$ overcomes that for $i = 60^\circ$ only at the edge of the figure, i.e., at energies ≥ 30 keV. This is due to the fact that between these two inclinations the difference in the $\cos i$ factor is severe, and the blueshift overcomes this only at high energies.

In Fig. 5.4, we have four panels for four inclination angles. In each panel, we have shown spectra

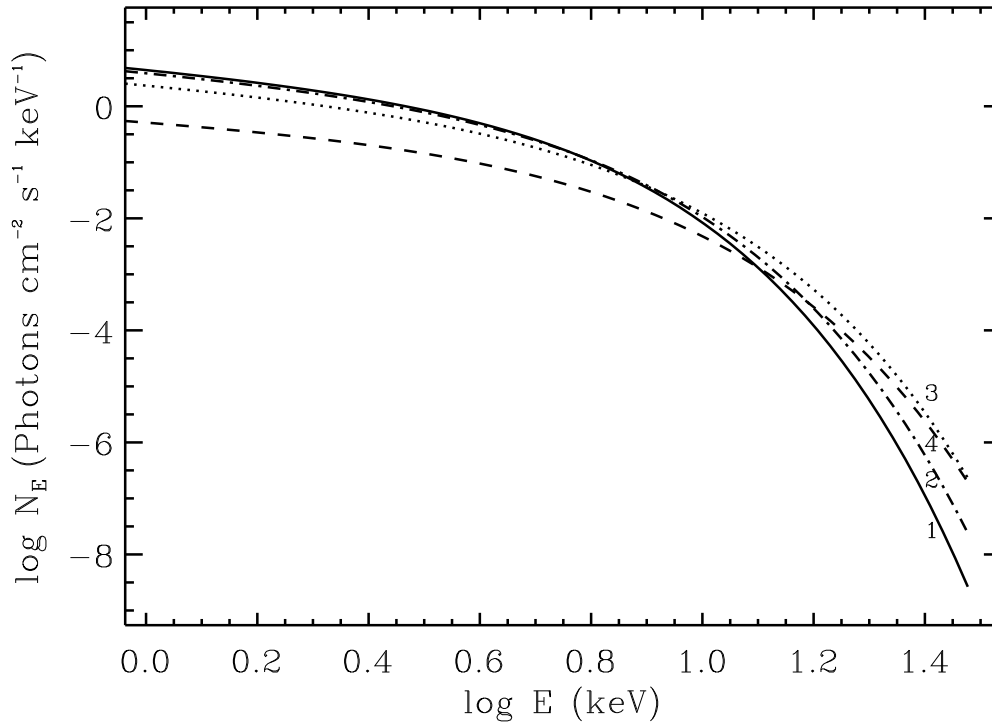


Figure 5.3: Inclination angle dependence: general relativistic spectra including light-bending effects from accretion disk around a neutron star of mass-shed limit configuration ($\Omega_* = 7001$ rad/s). Curve (1) corresponds to $i = 0^\circ$, curve (2) to $i = 30^\circ$, curve (3) to $i = 60^\circ$ and curve (4) to $i = 85^\circ$. The values of all the other parameters are as in Fig. 5.1.

for 3 different Ω_* (corresponding to non-rotating, intermediate and the mass-shed configurations). With the increase of Ω_* , disk temperature profile does not vary monotonically (see Fig. 3.3a). Hence the behavior of the spectrum is also non-monotonic with Ω_* . For non-rotating and mass-shed configurations (for the assumed values of other parameters) the temperature profiles are very similar. As a result, the plotted spectra for these two cases lie almost on top of each other. However, for $i = 0^\circ$ the flux corresponding to the mass-shed configuration is slightly higher than that for $\Omega_* = 0$, while the case is opposite at higher inclinations. This is a result of the inclination dependence of the $(1+z)$ factor given in Eq. 5.3.

In Fig. 5.5, we have compared the spectra for the four EOS models adopted by us, for configurations at the respective mass-shed limits (which correspond to different values of Ω_* because of the EOS dependence of the stellar structure). The values of all other parameters have been kept the same. We see that the total flux received varies monotonically with the stiffness parameter, and is higher for the softer EOS. This effect has been mentioned in Chapter 3. We see that at high ener-

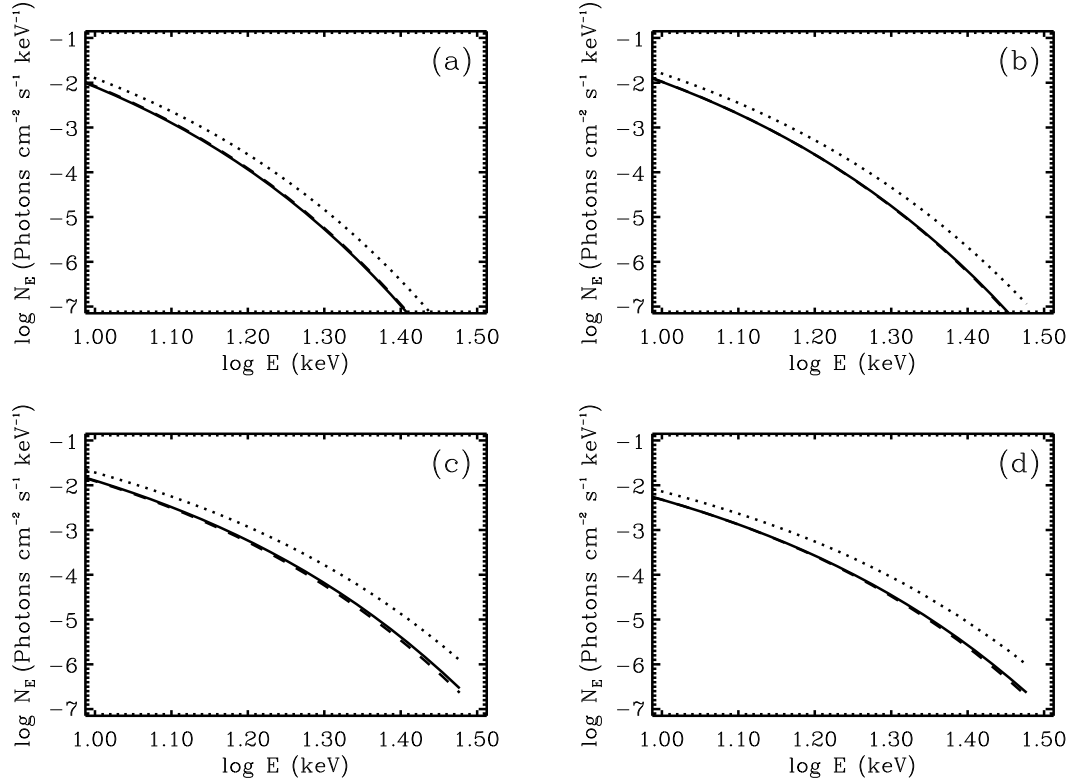


Figure 5.4: Rotation rate dependence: general relativistic spectra including light-bending effects from accretion disk around a neutron star. Panel (a) corresponds to $i = 0^\circ$, panel (b) to $i = 30^\circ$, panel (c) to $i = 60^\circ$ and panel (d) to $i = 85^\circ$. In each panel, the solid curve corresponds to $\Omega_* = 0$ rad/s, the adjacent dashed curve corresponds to $\Omega_* = 7001$ rad/s (the mass-shed limit) and the dotted curve corresponds to $\Omega_* = 3647$ rad/s. The values of all the other parameters are as in Fig. 5.1.

gies the fluxes for different EOS are considerably different. Therefore, fitting the observed spectra of LMXBs with our model spectra, particularly in hard X-rays, may provide a way to constrain neutron star EOS. However one must remember that these computations have been made assuming that the magnetic field of the compact object does not limit the inner boundary of the accretion disk. In the presence of a magnetic field strong enough to do so, appropriate modifications must be taken into account for the expected flux at high energies.

5.5 Conclusion

In this chapter we have computed the observed radiation spectrum from accretion disks around rapidly rotating neutron stars using fully general relativistic disk models. This is the first time such a calculation has been made in an exact way, without making any approximation in the

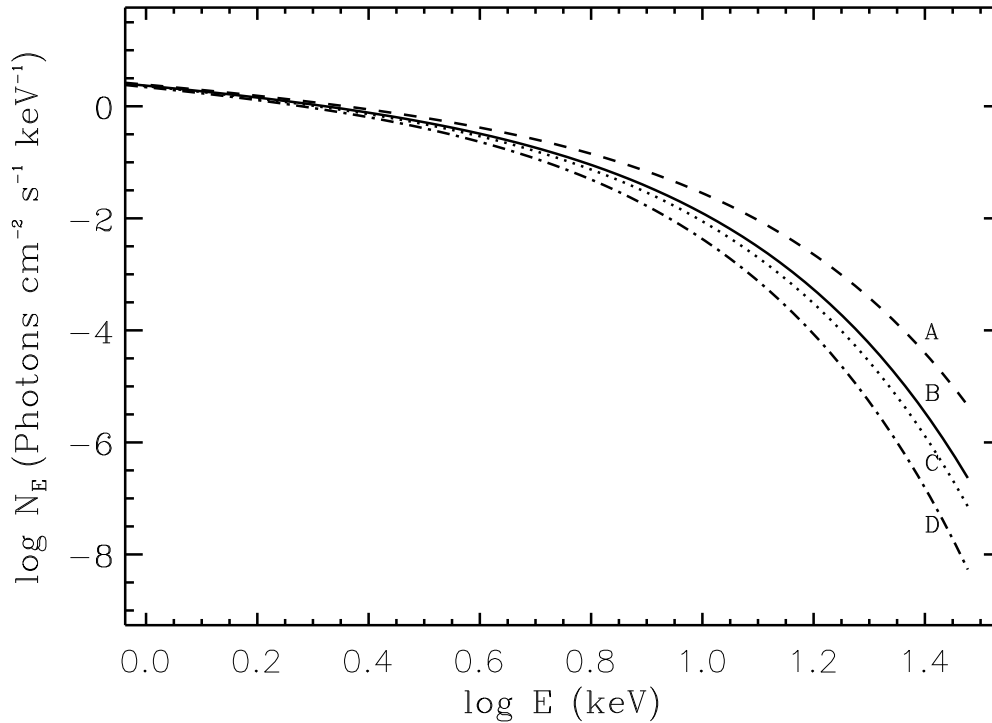


Figure 5.5: EOS model dependence: general relativistic spectra including light-bending effects from accretion disk around a neutron star of mass-shed configuration. EOS model (A) is for $\Omega_* = 11026$ rad/s, model (B) is for $\Omega_* = 7001$ rad/s, model (C) is for $\Omega_* = 6085$ rad/s and model (D) is for $\Omega_* = 4652$ rad/s. The values of all the other parameters are as in Fig. 5.1.

treatment of either rotation or general relativity. In computing the observed spectrum from the disk, we explicitly include the effects of Doppler shift, gravitational redshift and light-bending for an appropriate metric describing space-time around rapidly rotating neutron stars. We find that the effect of light-bending is most important in the high-energy (> 3 keV) part of the observed spectrum. Photons at these high energies originate close to the central star, and hence their trajectories are most affected by the light-bending effect. Depending on the viewing angle, this can enhance the observed flux at ~ 10 keV by as much as 250% compared to that expected if light-bending effects are neglected.

It is to be noted that in this work we have neglected the effect of irradiation of the disk. Miller & Lamb (1996) have discussed such effects on a test particle moving towards a slowly rotating neutron star. A strongly irradiated disk may not remain thin and the radiation force may relocate the position of inner edge of the disk. In addition to that, fractions of angular momentum and energy of the accreted matter may be transferred to the irradiating photons, resulting in a redistribution

of emitted flux in the disk. These effects will change our calculated spectrum to some extent. Therefore, we aim to modify our calculation in the direction of the work of Miller & Lamb (1996). However, it is to be noted that for rapidly rotating neutron stars, boundary layer emission is small and hence the effect of irradiation may not be important.

The calculations presented here deal only with the multicolor blackbody disk. In reality, there will be additional contributions to the observed spectrum from the boundary layer as well as a possible accretion disk corona, both of which are likely to add a power-law component at high energies (Popham & Sunyaev 2000, Dove et al. 1997). On the other hand, the spectra presented in Figs 5.2, 5.3 and 5.5 should remain essentially unaffected by boundary layer contribution, as these are for neutron stars rotating near the mass-shed limit for which the boundary layer luminosity will be negligible. For slowly rotating neutron stars, the disk component of the spectrum can be obtained by fitting and removing the contribution of the boundary layer, provided a good model for the boundary layer spectrum is available. Popham & Sunyaev (2000) have made an attempt to compute the boundary layer spectrum in the Newtonian approximation. General Relativistic modifications need to be included in these calculations to get a realistic estimate of the spectrum of the boundary layer. We plan to address this issue in a future work. In the slow rotation case, the spectrum of the disk itself may be somewhat modified by the presence of a boundary layer if it extends beyond the disk inner radius assumed in our computations here, thus curtailing the inner edge of the disk.

In addition to the contribution of the boundary layer, the possible contribution of an accretion disk corona to the emergent spectrum could also be significant. To be able to constrain the EOS models of Neutron Stars using the observed spectrum, this contribution must also be accurately estimated. We have not attempted to estimate this in the present work, where we restrict ourselves to thin blackbody and non-magnetic accretion disks in order to understand the effect of the EOS models describing neutron stars on the spectrum of the accretion disk alone. We view this as the first step in accurately modeling of the spectra of accreting neutron stars including the effects of general relativity and rotation. We may mention that the radiation originating in the accretion disk corona would also be modified by the gravitational redshift and light-bending effects, and the technique presented by us here will be useful also in that context.

The comparison of the non-rotating limit of our results with those of the fitting routine *GRAD* in the X-ray spectral reduction package *XSPEC* (Ebisawa et al. 1991), shows that the latter model overpredicts the high-energy component of the flux by a large factor. With the help of K. Ebisawa & T. Hanawa we have been able to trace this disagreement to certain simplifying approximations made in the *GRAD* code, as well as a couple of incorrect expressions being used there. Conclusions

based on the use of the *GRAD* routine may therefore need to be revised in the light of the new calculations presented here.

The computation of the complete spectrum in the manner presented here is rather time-consuming and therefore not quite suited to routine use. Therefore, in order to make our results available for routine spectral fitting work, we need to present a series of approximate parametric fits to our computed spectra. We do it to some extent in the next chapter.

The spectra presented here will find use in constraining the combined parameter set of the mass, the rotation speed and, possibly, the EOS, particularly of weakly magnetised, rapidly rotating neutron stars. The relevant signatures are most prominent in hard X-rays, above ~ 10 keV. Sensitive observations of hard X-ray spectra of LMXBs, therefore, are needed to fully utilise the potential of these results.

Chapter 6

Functional Approximation of Disk Spectra

6.1 Introduction

The observed spectrum for luminous LMXBs can be well-fitted by the sum of a multi-color blackbody spectrum (presumably from the accretion disk) and a single temperature blackbody spectrum (presumably from the boundary layer) (see Mitsuda et al. 1984). The multi-color spectrum can be calculated if the temperature profile of the accretion disk is known. Such a calculation should include the general relativistic effect, as near the surface of the neutron star, accretion flow is governed by the strong gravity. As is argued in Chapter 2, the effect of rapid rotation should also be taken into account. We have calculated such a spectrum for thin accretion disk in Chapter 5. The computation has been done both ignoring and considering the light-bending effect.

Our model spectra, when fitted to the observational data, can in principle constrain EOS and the values of the source parameters. However, computation of the spectra is numerically time consuming and hence direct fitting to the observational data is impractical. For the sake of ease in modeling, we present in this chapter, a simple empirical analytical expression that describes the numerically computed spectra. As shown later, the same expression (which has three parameters including normalization) can also describe the Newtonian spectra. In particular, the value of one of the parameters (called β -parameter here) determines whether the spectrum is relativistically corrected or not. This will facilitate comparison with observational data since only this β -parameter has to be constrained to indicate the effect of strong gravity in the observed spectrum.

Here, for fitting, we consider spectra, without light-bending effect, as the light-bending-calculation takes a huge amount of time. However, we fit the analytical function to a few light-bending-spectra, and show that the general conclusion remains the same, if the inclination angle (i) is not too large.

In section 6.2, we describe the method of functional approximation of the computed spectra. We display the results in section 6.3 and give a conclusive discussion in section 6.4.

6.2 Functional Approximation Method

In order to facilitate comparison with observations, we introduce a simple analytical expression which empirically describes the computed relativistic (and Newtonian) spectra.

$$S_f(E) = S_o E_a^{-2/3} \left(\frac{E}{E_a} \right)^\gamma \exp \left(- \frac{E}{E_a} \right) \quad (6.1)$$

where, $\gamma = -(2/3)(1 + E\beta/E_a)$, E_a , β and S_o are parameters and E is the energy of the photons in keV. $S_f(E)$ is in units of photons/sec/cm²/keV. To compare this empirical function with the computed spectra, we use a reduced χ^2 technique. In particular, we define a function

$$\chi^2 = \frac{1}{N} \sum_{i=1}^N \left[\frac{S_c(E_i) - S_f(E_i)}{0.1 S_c(E_i)} \right]^2 \quad (6.2)$$

where $S_c(E)$ is the computed spectra. The spectra are divided into N logarithmic energy bins. We have chosen the range of energy used in calculating χ^2 to be dependent on the location of the maximum of the energy spectrum ($ES_c(E)$) which is typically at 2 keV. The minimum energy is set to be one hundredth of this value (typically 0.02 keV) while the maximum is set at ten times (typically 20 keV). χ^2 is fairly insensitive to the number of energy bins; we take $N = 200$. For each $S_c(E)$ the best-fit parameters (E_a , β and S_o) are obtained by minimizing χ^2 .

The S_o parameter in Eq. (6.1), is the normalization factor and is independent of the relativistic effects. It depends only on the mass of the star (M), accretion rate (\dot{M}), distance to the source (D), color factor (f) and inclination angle (i) i.e $S_o \propto \dot{M}^{2/3} f^{-4/3} M^{1/2} D^{-2} \cos i$. The E_a parameter (which is in units of keV) describes the high energy cutoff of the spectrum. Its dependence on the space-time metric and inclination angle is complicated but it scales as $E_a \propto \dot{M}^{1/4} f$. The β -parameter depends only on the space-time metric (and the inclination angle), but not on accretion rate, distance to the source or color factor. This makes the β -parameter useful as a probe into the underlying space-time metric.

6.3 The Results

To illustrate the differences between the relativistic and Newtonian spectra, we show in Fig. 6.1, the computed relativistic spectrum (solid line) and the Newtonian spectrum (dashed line) for the same parameters. It is to be noted that, here we plot energy flux ($ES_c[E]$), instead of photon flux

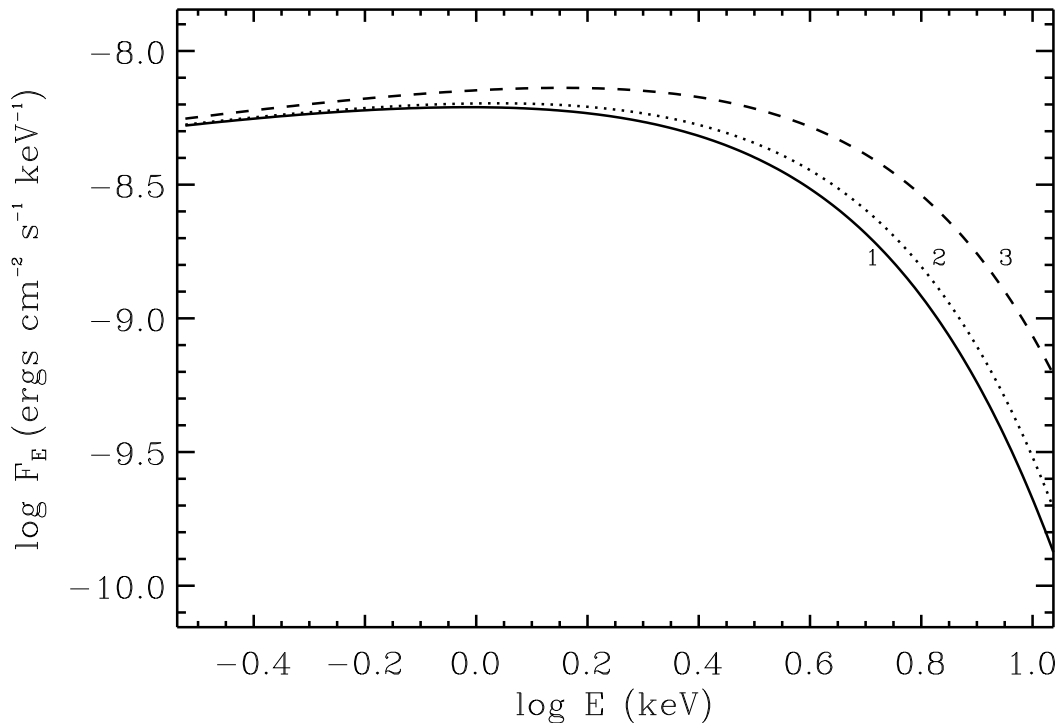


Figure 6.1: General relativistic spectrum (solid line) for a neutron star configuration with mass $M = 1.4M_{\odot}$, spin rate $\Omega_* = 0$, distance to the source $D = 5$ kpc, inclination angle $i = 30^\circ$, accretion rate $\dot{M} = 10^{18} \text{ g s}^{-1}$ and color factor $f = 2$. Dashed line: the spectrum expected from a source with the same disk parameters but without the relativistic effects (Newtonian spectrum). Dotted line: The spectrum for the same disk parameters but without the effect of Doppler and gravitational red-shifts (i.e. z is set to zero). The EOS model (B) is used here.

($S_c[E]$) (as is the case in Fig. 5.1). This is, because, $ES_c[E]$ is used to choose the energy range for fitting. However, as mentioned in the previous section, we fit $S_c[E]$ by the analytical function. The Newtonian spectrum is the spectrum expected from a standard non-relativistic disk (Shakura & Sunyaev 1973) but with the specific intensity and the effective temperature modified by the color factor (Eqs. 3.1 and 5.2). In order to isolate the different contributions, we have also plotted in Fig. 6.1, the theoretical spectrum arising from relativistic temperature profile but without the effect of Doppler/gravitational red-shift (dotted line). The relativistic spectrum is under-luminous compared to the Newtonian one at high energies – this is primarily because of the difference in the radial temperature profile (see Chapter 3). The difference between the two spectra is nearly 50% at 2 keV. We emphasize here, that such high difference is only true when both the spectra are calculated for the same disk parameters. If the Newtonian spectra is calculated for slightly different

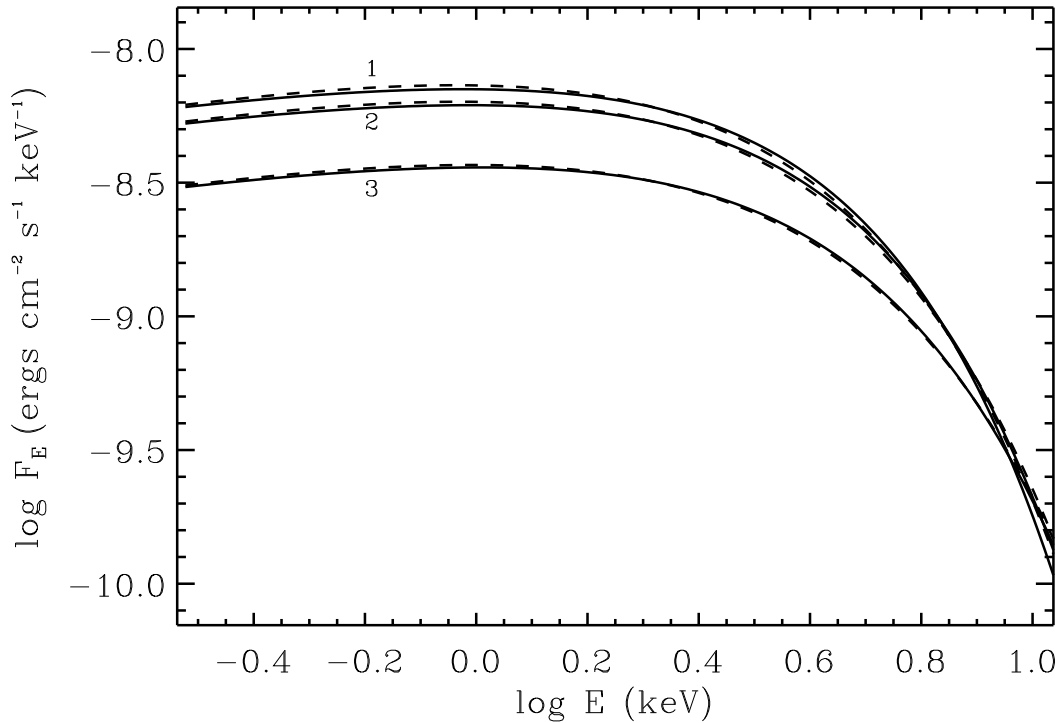


Figure 6.2: Relativistic spectra for three different inclination angles ($i = 0^\circ, 30^\circ, 60^\circ$) with rest of the parameters same as in Fig. 6.1 (solid lines). Dashed lines: empirical fit to the relativistic spectra using Eq. (6.1). The minimum $\chi^2 = 0.073, 0.049$ and 0.026 for $i = 0^\circ, 30^\circ$ and 60° respectively.

values of disk parameters (e.g. accretion rate, inclination angle, distance to the source) the average discrepancy between the two spectra will be less (Ebisawa, Mitsuda and Hanawa 1991).

Fig. 6.2 shows the relativistic spectra for three different inclination angles (solid lines) and the corresponding empirical fits using Eq. 6.1 (dashed lines). The minimum χ^2 obtained while fitting these spectra was < 0.1 , which means that the average discrepancy is less than 3%. This is also true for other disk parameters and EOS models considered in this work. Thus the empirical function (Eq. 6.1) is a reasonable approximation to the computed relativistic spectra. It also describes the Newtonian spectra to a similar degree of accuracy.

We show in Fig. 6.3, the variation of minimum χ^2 (i.e. minimized w.r.t. to parameters E_a and S_o only) as a function of the β -parameter for the three spectra shown in Fig. 6.2 and for the Newtonian one. For the Newtonian case the minimum χ^2 occurs for $\beta \approx 0.4$ while it is lower for the relativistic cases. For example, consider the relativistic spectrum for parameters listed in Fig. 6.1 and for $i = 30^\circ$ (line marked as 3 in Fig. 6.3). If this spectrum is fitted with the empirical

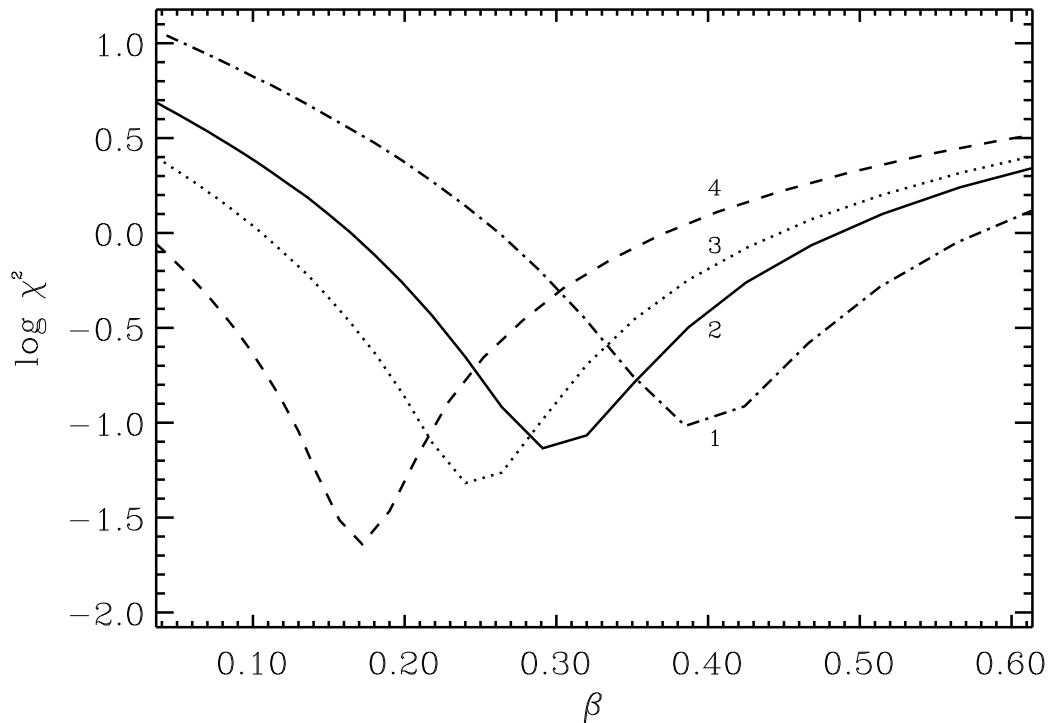


Figure 6.3: Variation of minimum χ^2 (i.e. minimized with respect to parameters E_a and S_o) with parameter β . Curves marked 2, 3 and 4 correspond to the spectra shown in Fig. 3 for $i = 0^\circ, 30^\circ$ and 60° respectively. Curve marked 1 is for the Newtonian spectra shown in Fig. 6.1.

function the minimum $\chi^2 = 0.05$ (corresponding to an average discrepancy of 2%) and the best-fit β -parameter is $\beta \approx 0.25$. For a Newtonian β -parameter value of ≈ 0.4 , the minimum χ^2 increases to 0.1, corresponding to an average discrepancy of more than 3%. Thus the empirical function can resolve the difference between the Newtonian and the relativistic one at the 10% level. For an observed spectrum fitted using the empirical function, if the best-fit range of β -parameter excludes the Newtonian value of 0.4, that would strongly indicate that the spectrum has been modified by strong gravitational effects. To show the robustness of this result we display in Figs. 6.4, 6.5 and 6.6, the variation of the best-fit β -parameter with i , for different EOS models, masses and spin rates of the central object respectively. For all these cases the best-fit β -parameter is less than 0.4. However, for very high value of i ($i \gtrsim 85^\circ$), fitting to the light-bending-spectra gives $\beta > 0.4$. Therefore, for $i \gtrsim 85^\circ$, Newtonian and general relativistic spectra can not be distinguished by this method. But for upto moderately high values of i (for which light-bending-spectra still gives $\beta < 0.4$), this method is very effective. Parameter E_a is useful to determine the accretion rate. However, it also depends on the metric and inclination angle. We show this dependence in Fig.

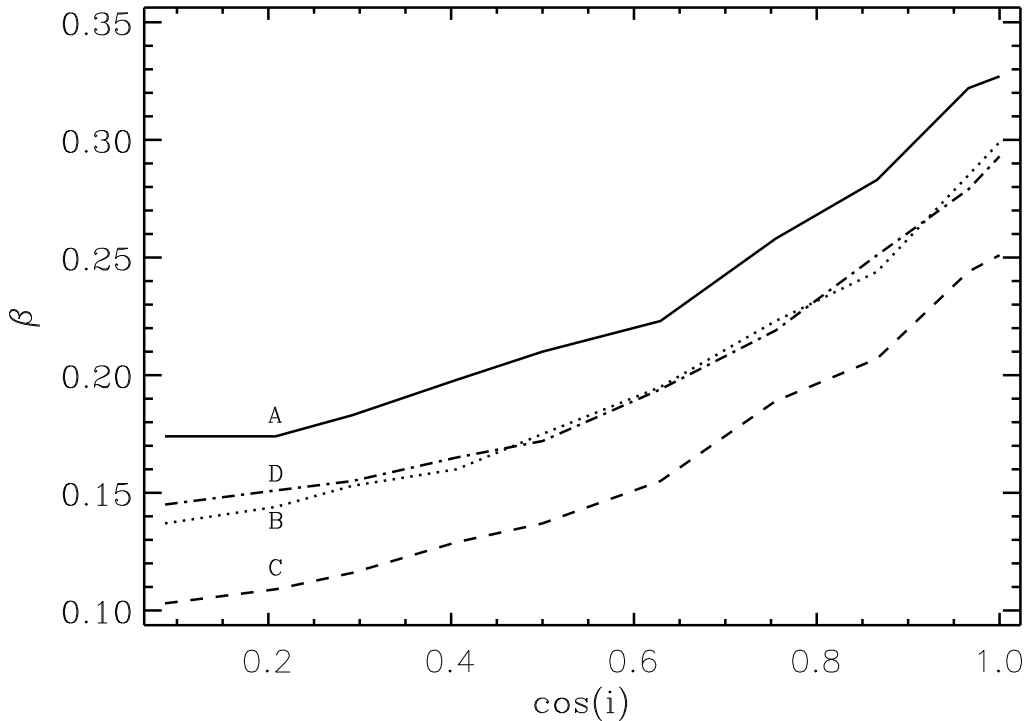


Figure 6.4: Variation of the best-fit β -parameter with inclination angle for different equations of states (each curve is marked by the corresponding EOS model). The values of the other parameters are as in Fig. 6.1.

6.7.

6.4 Summary and Discussion

In this chapter, a simple empirical function has been presented which describes the numerically computed relativistic spectra well. This will facilitate direct comparison with observations. The empirical function (Eq. 6.1) has three parameters including normalization. Another important advantage of this function is that it also describes the Newtonian spectrum adequately, and the value of one of the parameters (β -parameter) distinguishes between the two. In particular, the best-fit β -parameter ≈ 0.4 for the Newtonian case, while it ranges from 0.1 to 0.35 for relativistic case depending upon the inclination angle, EOS, spin rate and mass of the neutron stars. However, as mentioned in section 6.3, this method is effective for upto moderately high values of i .

In principle, for sufficiently high quality data, the effects of strong gravity on the disk spectrum can be detected using this empirical function as a fitting routine and constraining the β -parameter.

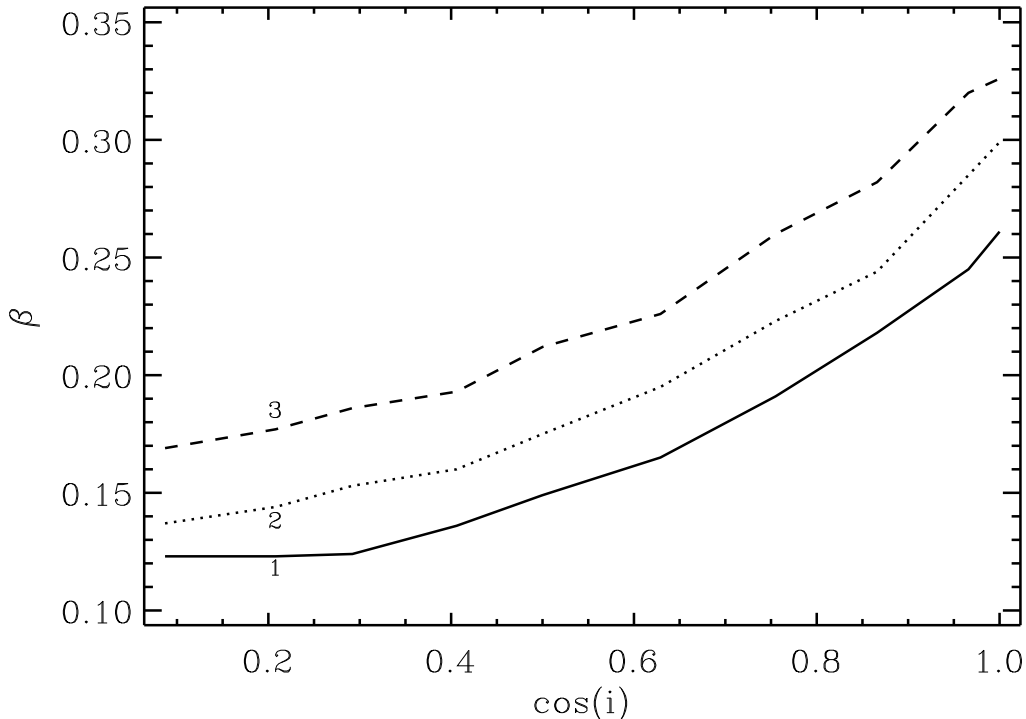


Figure 6.5: Variation of the best-fit β -parameter with inclination angle for different neutron star masses. Curve 1: $M = 1.0M_{\odot}$, curve 2: $M = 1.4M_{\odot}$, curve 3: $M = 1.788M_{\odot}$. The values of the other parameters are as in Fig. 6.1.

However, it must be emphasized that there are several reasons why this may not be possible. There could be systems which have additional components in the X-ray spectra; for example boundary layer emission from the neutron star surface. Uncertainties in modeling these additional components may lead to a wider range in the best-fit β -parameter. Thus accurate spectra of the boundary layer (with relativistic corrections) is also needed for modeling these systems. Moreover, X-rays could be emitted from hotter regions (e.g an innermost hot disk or a corona) giving rise to a Comptonized spectra instead of the sum of local emission assumed here. In this case, the empirical fit will probably not describe the observational data well. It has been assumed here that the color factor is independent of radius. Shimura and Takahara (1995) have shown from numerical computation that this could be the case for an accretion disk in a Schwarzschild metric. Apart from the fact that this was done for Schwarzschild metric, their numerical computation depends on the vertical structure of the disk which in turn depends on the unknown viscosity mechanism in the disk. If the color factor has a radial dependence, the spectral shape might change, which may be confused to be a relativistic effect.

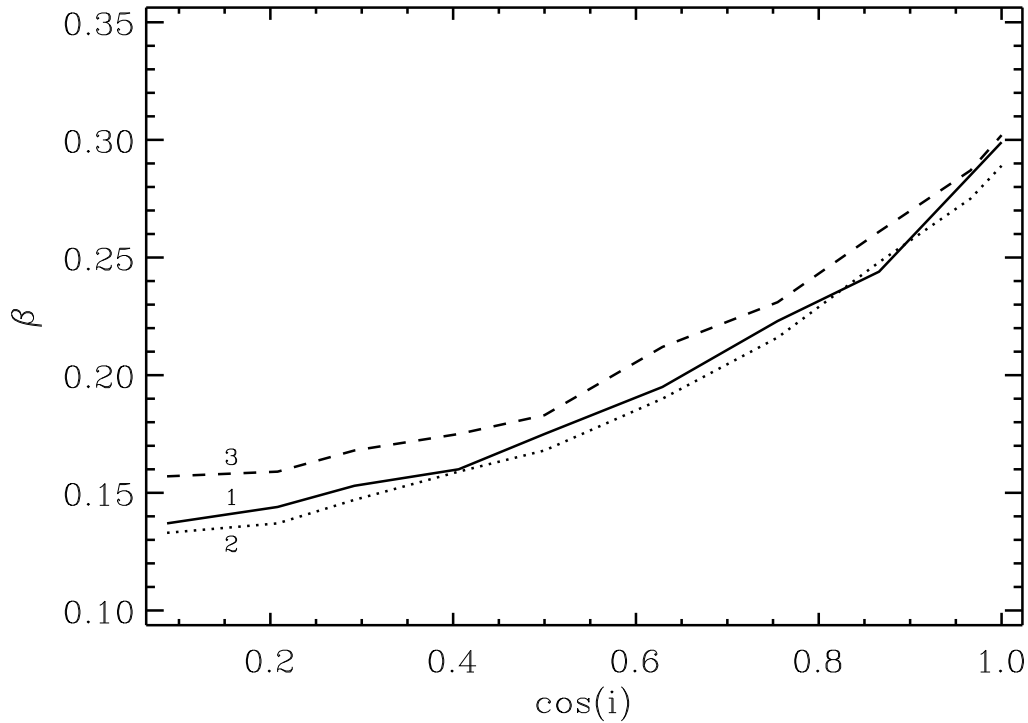


Figure 6.6: Variation of the best-fit β -parameter with inclination angle for different neutron star spin rates. Curve 1: $\Omega_* = 0$ radians s^{-1} , curve 2: $\Omega_* = 2044$ radians s^{-1} , curve 3: $\Omega_* = 7001$ radians s^{-1} (mass-shed limit). The values of the other parameters are as in Fig. 6.1.

Despite these caveats the method described in this chapter will be a step forward in the detection of strong gravity effects in the spectra of X-ray binaries. Future comparison with high quality observational data, will highlight the theoretical requirements that have to be met, before concrete evidence for strong gravity are detected in these systems and the enigmatic region around compact objects is probed.

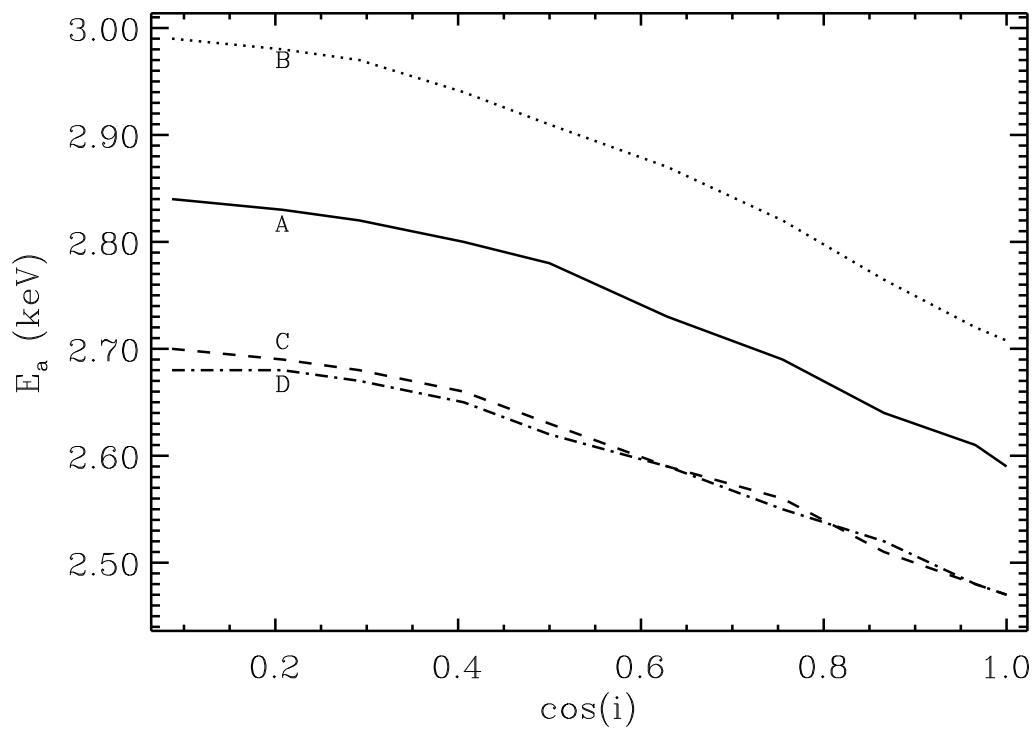


Figure 6.7: Variation of the best-fit E_a -parameter with inclination angle for different equations of state. The curves correspond to the same equation of states as listed in Fig. 6.4. The values of the other parameters are as in Fig. 6.1.

Chapter 7

Disk Temperature Profiles for Strange Stars: A Comparison With Neutron Stars

7.1 Introduction

We have mentioned in the earlier chapters that low mass X-ray binaries (LMXBs) are believed to contain either neutron stars (NSs) or black holes accreting from an evolved or main sequence dwarf companion that fills its Roche-lobe. The proximity of the companion in these systems cause matter to spiral in, forming an accretion disk around the central accretor. Observations of LMXBs can provide vital clues of the structure parameters of the accretors and, in particular for NSs, this can lead to constraining the property of the high density matter composing their interiors. Therefore, the estimation of the radius of the central accretor in SAX J1808.4-3658 and 4U 1728-34 (Li et al. 1999a; Li et al. 1999b; Burderi & King 1998; Psaltis & Chakrabarty 1999) indicating the object to be more compact than stars composed of high density nuclear matter, acquires significance. These results moot alternate suggestion about the nature of the central accretors in at least some of the LMXBs.

In this regard, the *strange matter hypothesis*, formulated by Bodmer (1971) and Witten (1984) (see also Itoh 1970; Terazawa 1979), has received much attention recently. The hypothesis suggests strange quark matter (SQM, made up of u, d and s quarks), in equilibrium with weak interactions, to be the actual ground state of strongly interacting matter rather than ^{56}Fe . If this were true, under appropriate conditions, a phase transition within a neutron star (e.g. Olinto 1987; Cheng & Dai 1996; Bombaci & Datta 2000) could convert the entire system instantaneously into a conglomeration of strange matter or, as is commonly referred to in literature, strange stars (SSs). Here we consider

only *bare* strange stars, i.e., we neglect the possible presence of a crust of normal (confined) matter above the deconfined quark matter core (see e.g. Alcock, Farhi & Olinto 1986).

It is of fundamental interest - both for particle physics and astrophysics - to know whether strange quark matter exists. Answering this question requires the ability to distinguish between SSs and NSs, both observationally as well as theoretically and this has been the motivation of several recent calculations (Xu et al. 2001; Gondek-Rosinska et al. 2000; Bombaci et al 2000; Zdunik 2000; Zdunik et al 2000a; Zdunik et al 2000b; Datta et al 2000; Stergioulas et al 1999; Gourgoulhon et al 1999; Xu et al 1999; Gondek & Zdunik 1999; Bulik et al. 1999; Lu 1998; Madsen 1998). One of the most basic difference between SSs and NSs is the mass–radius relationship (Alcock, Farhi & Olinto 1986): while for NSs, this is an inverse relationship (radius decreasing for increasing mass), for SSs there exist a positive relationship (radius increases with increasing mass). In addition to this difference, due to SSs being self–bound objects, there also exists the possibility of having configurations with arbitrarily small masses; NSs on the other hand, have a minimum allowed mass (e.g. Shapiro & Teukolsky 1983; Glendenning 1997; and more recently, Gondek et al. 1997; Gondek et al. 1998; Goussard et al. 1998; Strobel et al 1999; Strobel & Weigel 2001). Nevertheless, it must be remarked that for a value of gravitational mass equal to $1.4 M_{\odot}$ (the canonical mass for compact star candidates), the difference between the predicted radii of nonrotating configurations of SS and NS amounts, at most, only to about 5 km; a value that cannot be directly observed. There arises, therefore, a necessity to heavily rely on models of astrophysical phenomena associated with systems containing a compact star to estimate the radius: for isolated pulsars, models of glitches (e.g. Datta & Alpar 1993; Link et al. 1992) have been used in the past for making estimates of the structure parameters and for compact stars in binaries, such estimates have been made by appropriately modeling photospheric expansion in X–ray bursts (van Paradijs 1979; Goldman 1979) and more recently by constraining the inner–edge of accretion disks and demanding that the radius of the compact star be located inside this inner–edge (Li et al. 1999a; Li et al. 1999b; Burderi & King 1998; Psaltis & Chakrabarty 1999). In particular, the work by Li et al. (1999a; 1999b) suggest strange stars as possible accretors. However, these calculations did not include the full effect of general relativity. Even on inclusion of these effects (Bombaci et al 2000), the results for at least one source: 4U 1728-34, remain unchanged. There have also been contradictory reports on the existence of strange stars: for example, calculations of magnetic field evolution of SSs over dynamical timescales, make it difficult to explain the observed magnetic field strengths of isolated pulsars (Konar 2000). On the other hand, Xu & Busse (2001) show that SSs may possess magnetic fields, having the observed strengths. These magnetic fields, these authors argue, originate due to dynamo effects. In our analysis here, we ignore the effects of magnetic field.

In this chapter, we calculate constant gravitational mass equilibrium sequences of rotating SSs, considering the full effect of general relativity. We solve Einstein field equations and the equation for hydrostatic equilibrium simultaneously for different SS equations of state (EOS) models, using the same procedure as described in Chapter 2. We compare our theoretical results with those obtained for NSs (Chapter 3). In addition, we calculate the radial profiles of effective temperature in accretion disks around SSs (same procedure as described in Chapter 3). These profiles are important inputs in accretion disk spectrum calculations, crucially depending on the radius of the inner edge of the accretion disk. This radius is determined by the location of r_{orb} with respect to that of the surface (R) of the star, both of which are sensitive to the EOS, through the rotation of the central object. In particular, we notice that r_{orb} increases with stellar angular momentum (J) beyond a certain critical value (a property not seen in either rotating black holes or neutron stars). We trace this behavior to the dependence of dr_{orb}/dJ on the rate of change of the radial gradient of the Keplerian angular velocity at r_{orb} with respect to J . The prospect of using the temperature profiles for calculation of accretion disk spectrum and subsequent comparison with observational data, therefore, gives rise to the possibility of constraining SS EOS, and eventually to distinguish between SSs and NSs.

In section 7.2, we discuss the equations of state used in this chapter. We display the results in section 7.3 and give a summary of the chapter in section 7.4.

7.2 Equation of State

For strange quark matter we use two phenomenological models for the EOS. The first one is a simple EOS (Farhi & Jaffe 1984) based on the MIT bag model for hadrons. We begin with the case of massless, non-interacting (*i.e.* QCD structure constant $\alpha_c = 0$) quarks and with a bag constant $B = 60 \text{ MeV/fm}^3$ (hereafter EOS H). Next, we consider a finite value for the mass of the strange quark within the same MIT bag model EOS. We take $m_s = 200 \text{ MeV}$ and $m_u = m_d = 0$, $B = 60 \text{ MeV/fm}^3$, and $\alpha_c = 0$ (EOS G). To investigate the effect of the bag constant, we take (almost) the largest possible value of B for which SQM is still the ground state of strongly interacting matter, according to the strange matter hypothesis. For massless non-interacting quarks this gives $B = 90 \text{ MeV/fm}^3$ (EOS F). The second model for SQM is the EOS given by Dey et al. (1998), which is based on a different quark model than the MIT bag model. This EOS has asymptotic freedom built in, shows confinement at zero baryon density, deconfinement at high density, and, for an appropriate choice of the EOS parameters entering the model, gives absolutely stable SQM according to the strange matter hypothesis. In the model by Dey et al. (1998), the quark interaction

86 Chapter 7. Disk Temperature Profiles for Strange Stars: A Comparison With Neutron Stars

is described by a screened inter-quark vector potential originating from gluon exchange, and by a density-dependent scalar potential which restores chiral symmetry at high density (in the limit of massless quarks). The density-dependent scalar potential arises from the density dependence of the in-medium effective quark masses M_q , which are taken to depend upon the baryon number density n_B according to $M_q = m_q + 310\text{MeV} \times \text{sech}(\nu \frac{n_B}{n_0})$, where n_0 is the normal nuclear matter density, $q(= u, d, s)$ is the flavor index, and ν is a parameter. The effective quark mass $M_q(n_B)$ goes from its constituent masses at zero density, to its current mass m_q , as n_B goes to infinity. Here we consider a parameterization of the EOS by Dey et al. (1998), which corresponds to the choice $\nu = 0.333$ for the parameter entering in the effective quark mass, and we denote this model as EOS E.

For NSs, we use three representative equations of state which span a wide range of *stiffness*. These are EOS models A, B and D, as mentioned in section 2.4.

A list of the designation along with the salient features of the EOS models used here is provided in Table 7.1.

EOS label	compact star	EOS model
E	SS	Dey et al. (1998), their model SS1
F	SS	Farhi and Jaffe (1984), $B = 90 \text{ MeV}/\text{fm}^3$, $m_s = 0$
G	SS	Farhi and Jaffe (1984), $B = 60 \text{ MeV}/\text{fm}^3$, $m_s = 200 \text{ MeV}$
H	SS	Farhi and Jaffe (1984), $B = 60 \text{ MeV}/\text{fm}^3$, $m_s = 0$
A	NS	Pandharipande (1971), hyperonic matter
B	NS	Baldo et al. (1997), nuclear matter
D	NS	Sahu et al. (1993), nuclear matter

Table 7.1: The list of EOS models used in this chapter.

We also display the qualitative variations in these EOS models in a log-log plot of Fig. 7.1. The differences between SS and NS EOS are plainly evident, especially at lower pressures.

7.3 The Results

We have calculated the structure parameters and the disk temperature profiles for rapidly rotating, constant gravitational mass sequences of SSs in general relativity. The results for SS are compared

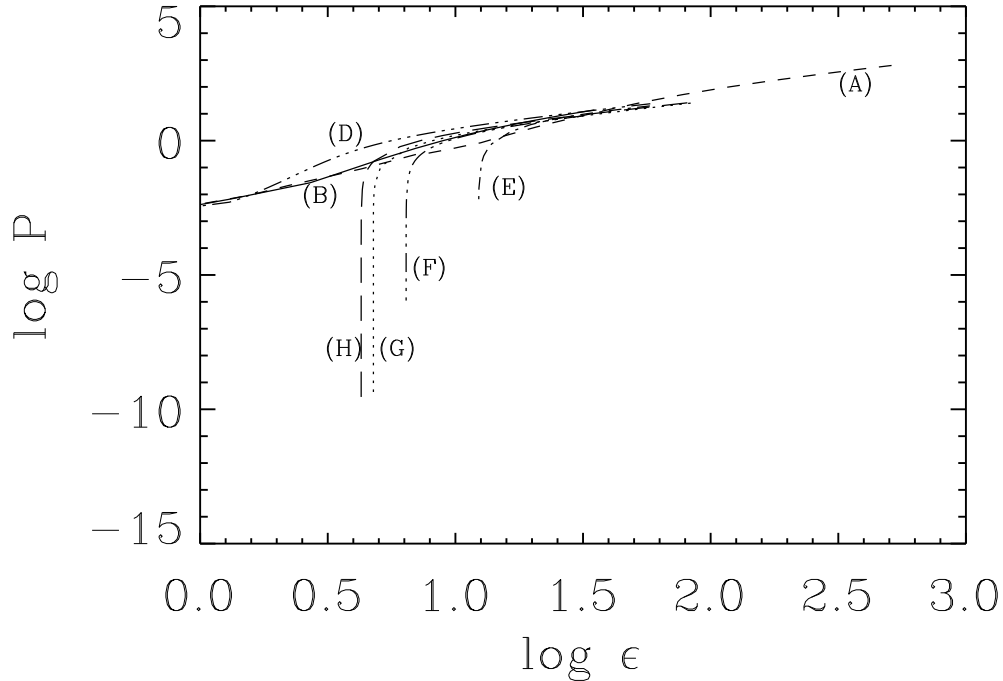


Figure 7.1: Logarithmic plot of pressure vs. matter density for the EOS models used here. The density and pressure are in units of $1.0 \times 10^{14} \text{ g cm}^{-3}$ and $(1.0 \times 10^{14}) c^2 \text{ cgs}$ respectively.

with those for NS. For illustrative purposes here, we have chosen the value of gravitational mass to be $1.4 M_{\odot}$.

Fig. 7.2 depicts the variation of Ω_* with the total angular momentum (J) for constant gravitational mass and for the four SS EOS. The curves extend from the static limit to the mass-shed limit. The striking feature here is that, although J increases monotonically from slow rotation to mass-shed limit, Ω_* shows a non-monotonic behavior: maximum value of Ω_* (i.e. Ω_*^{\max}) occurs at a value of J lower than that for mass-shed limit. Although this seems to be a generic feature for SS EOS, Ω_* is always a monotonic function of J for constant gravitational mass NS sequences and hence constitutes an essential difference between SS and NS (see section 7.4 for discussions). Our calculations show that at maximum Ω_* , the ratio of rotational kinetic energy to total gravitational energy: T/W approaches the value of 0.2 (see next paragraph). It has been pointed out by Gourgoulhon et al., 1999 that such high values of T/W make the configurations unstable to triaxial instability. It can also be noticed that for stiffer EOS, the star possesses a higher value of J at mass-shed limit (Ω_*^{\max} also occurs proportionately at higher J).

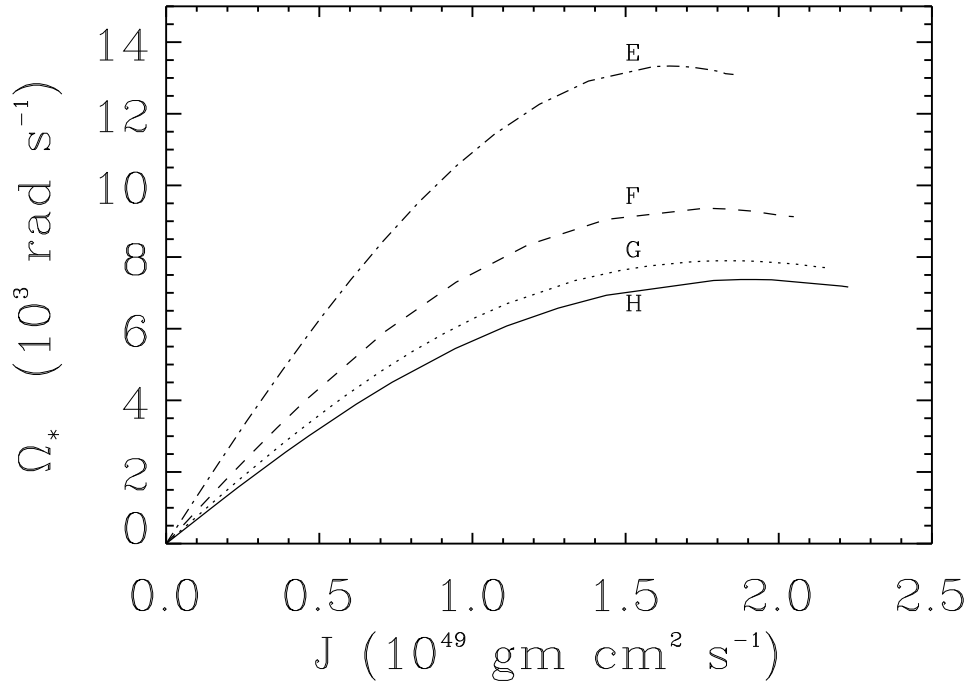


Figure 7.2: Angular speed (Ω_*) as a function of total angular momentum (J) for strange star. The curves are labelled by the nomenclature of Table 7.1 and are for a fixed gravitational mass ($M = 1.4 M_\odot$) of the strange star.

In order to expand upon the results of Fig. 7.2, we plot Ω_* vs. T/W for various SS EOS in Fig. 7.3. It is seen that for all SS EOSs, T/W becomes greater than 0.25 at mass-shed limit, while for NS EOSs it is usually between 0.1 and 0.14 (Cook et al. 1994). Interestingly, for all SS EOSs, Ω_*^{\max} occurs at about the same value of T/W (≈ 0.2).

Fig. 7.4 displays Ω_* and Ω_{in} (i.e. the Keplerian angular speed of a test particle at r_{in}) against J . The four panels are for the four SS EOS we use. We notice the interesting behavior that Ω_* and Ω_{in} curves cross each other at a point near Ω_*^{\max} . For rotating NS configurations, since the equality $r_{\text{in}} = R$ is almost always (except for very soft EOS models: Fig. 3.1) achieved for rotation rates well below that at mass-shed limit (for $M = 1.4 M_\odot$), always $\Omega_* \leq \Omega_{\text{in}}$ (the equality is achieved only at mass-shed limit). On the other hand, for SSs, r_{orb} is almost always greater than R (as explained in the next paragraph) and when the star approaches Keplerian angular speed at the equator, Ω_* becomes greater than Ω_{in} .

Fig. 7.5 is a plot of the variation of r_{in} and R with Ω_* for four SS EOSs. We see that the

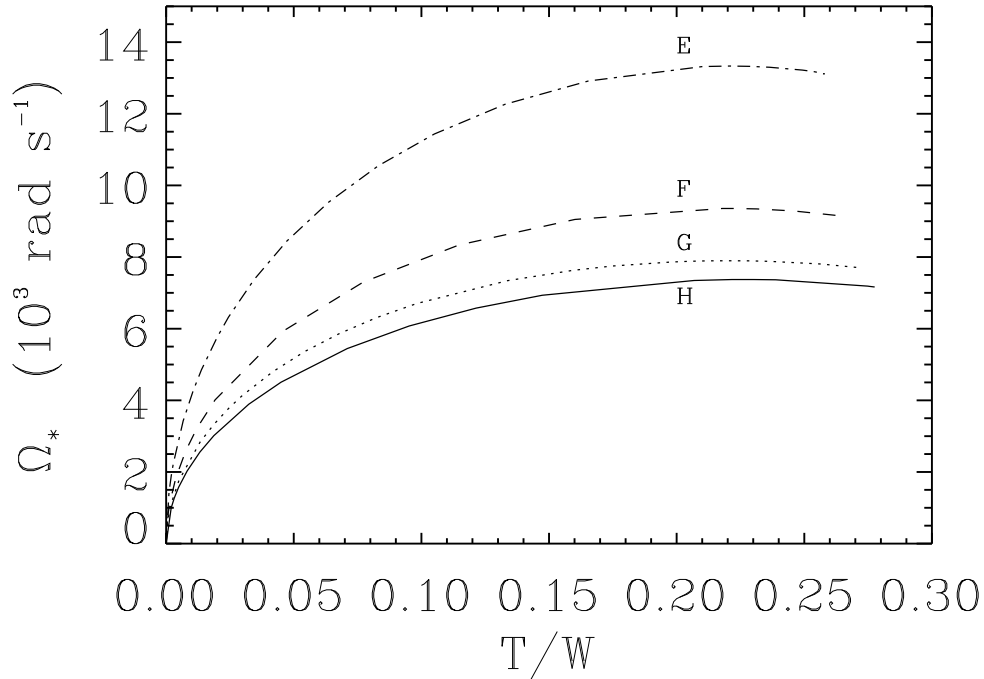


Figure 7.3: Angular speed (Ω_*) as a function of the ratio of rotational kinetic energy and gravitational binding energy (T/W) for strange star. Curve labels have the same meaning as in Fig. 7.2.

behavior of R is monotonic from slow rotation to the mass-shed limit, even though that of Ω_* is not. As mentioned earlier for all Ω_* from static limit upto mass-shed limit, $r_{\text{in}} > R$ for 3 SS EOSs. Only for the stiffest SS EOS, that we have chosen, does the disk touch the star (for an intermediate value of Ω_*). This is distinct from the case of NS (see Fig. 3.1). The reason for such a behavior is the non-monotonic variation of r_{orb} with J for SSs (contrary to the case of NSs and black holes); this is discussed further in the next section.

In Fig. 7.6, we plot the variation of r_{in} with Ω_* for three SS EOSs and two NS EOSs: for each case, our softest EOS and our stiffest EOS have been chosen. In addition, we display the corresponding results for EOS model F too. It is clear that in the $r_{\text{in}}-\Omega_*$ space, there exists a region that is spanned by both NS and SS configurations. Interestingly, however, there also exists certain regions occupied exclusively by either SS or NS configurations. The possible observational consequences of this result is discussed in the next section.

Fig. 7.7 displays the radial profiles of temperature: (i) assuming a purely Newtonian accretion

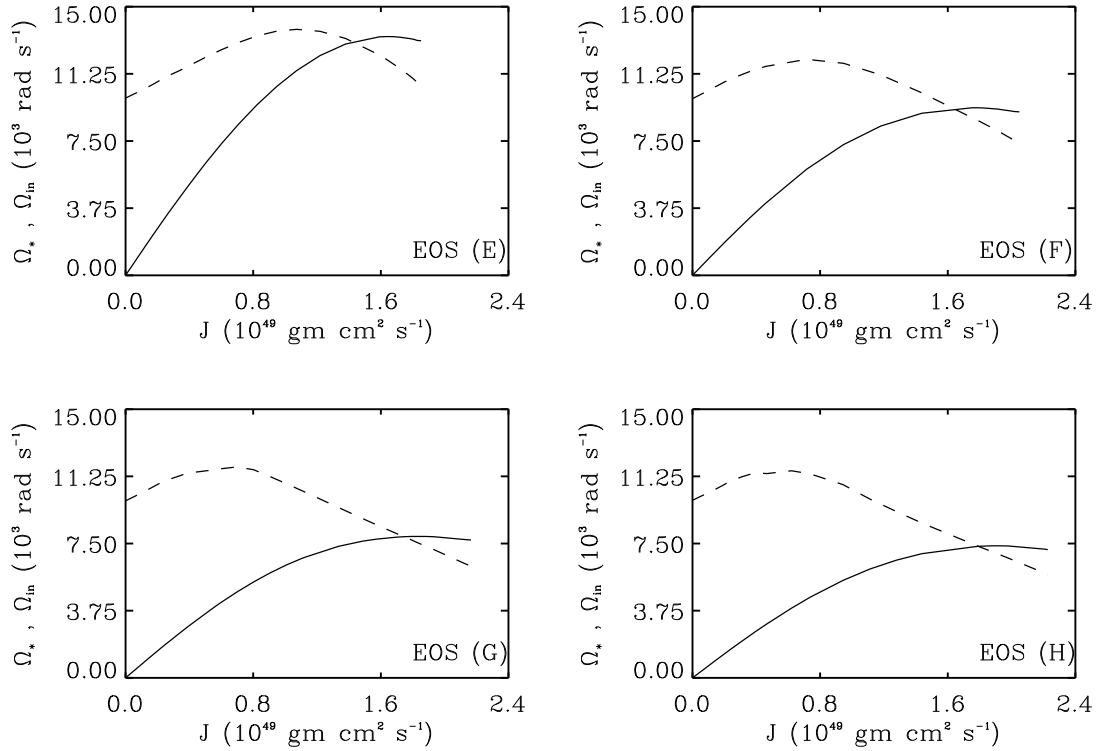


Figure 7.4: Angular speed (Ω_*) of the strange star (solid curve) and the Keplerian angular speed (Ω_{in}) of a test particle at the inner edge of the disk (dashed curve) as functions of total angular momentum (J) of strange star. The curves are for a fixed gravitational mass ($M = 1.4 M_\odot$) of the strange star. Different panels are for different SS EOS models.

disk and (ii) considering general relativistic accretion disks for (a) SS (EOS H) and (b) NS (EOS B), each represented by two configurations: the non-rotating and mass shed for $M = 1.4 M_\odot$. We also display the temperature profile (curve 5) for a SS configuration of $M = 1 M_\odot$, described by EOS (A) (the constraints obtained by Li et al. 1999a; 1999b) and having a period $P = 2.75$ ms (the mass and period corresponding to that inferred for the source 4U 1728-34: Méndez & van der Klis 1999). It must be remembered that in this figure (and the next), curve 5 represents the temperature profile for a different M value than the rest of the curves and is displayed in the same figure, only for illustrative purposes. From this figure we see that for $M = 1.4 M_\odot$, the Newtonian value of temperature is about 25% higher than the general relativistic value near the inner edge of the disk. This shows the importance of general relativity and rotation near the surface of the star. The difference between the effects of SS EOS and NS EOS on temperature profiles (at the inner portion of the disk) is also prominent at mass-shed limit (due to the difference in rotation rates for these two configurations). Such differences in temperature profiles are also expected to show up in

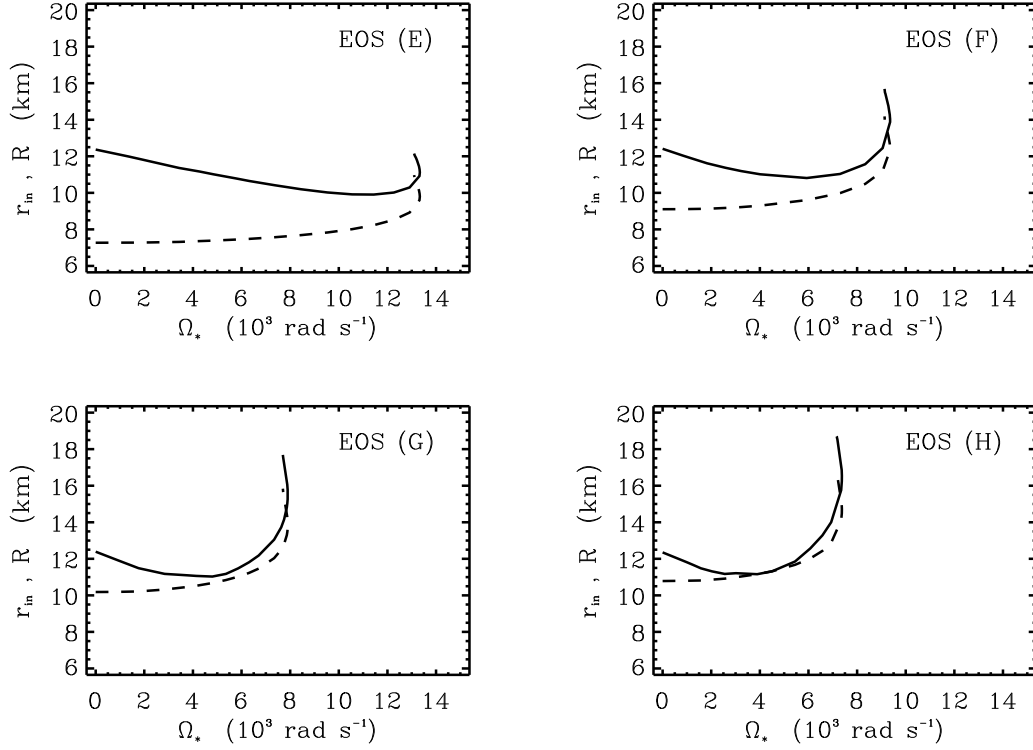


Figure 7.5: Disk inner edge radius (r_{in} , solid curve) and strange star radius (R , dashed curve), as functions of angular speed Ω_* for various EOS models. The curves are for a fixed gravitational mass ($M = 1.4 M_{\odot}$) of the strange star.

the calculations of spectra at higher energies.

In the panel (a) of Fig. 7.8, we display the temperature profiles for configurations (as in Fig. 7.7) composed of SS EOS (H) (curves 1–4), represented by different Ω_* (corresponding to $\Omega_* = 0$, for minimum r_{in} , $\Omega_* = \Omega_*^{\text{max}}$ and mass-shed limit); curve (5) is the same as in Fig. 7.7. The behavior of temperature profiles is non-monotonic with Ω_* . The panel (b) shows the temperature profiles at mass-shed for various SS EOS along with curve (5). Here the temperature profiles show monotonic behavior with the stiffness of EOS. The behavior of the temperature profiles in both the panels are similar to those calculated for NSs (Chapter 3). Notice the substantial difference in the maximum temperature; sufficiently sensitive observations are, therefore, expected to complement the findings of Li et al. (1999a; 1999b).

The variations of E_{D} , E_{BL} , the ratio $E_{\text{BL}}/E_{\text{D}}$ and $T_{\text{eff}}^{\text{max}}$ with Ω_* are displayed in Fig. 7.9. Each plot contains curves corresponding to all the SS EOS models considered here. The behavior of all the curves are similar to those for any NS EOS (see Fig. 3.5). The only difference being that due

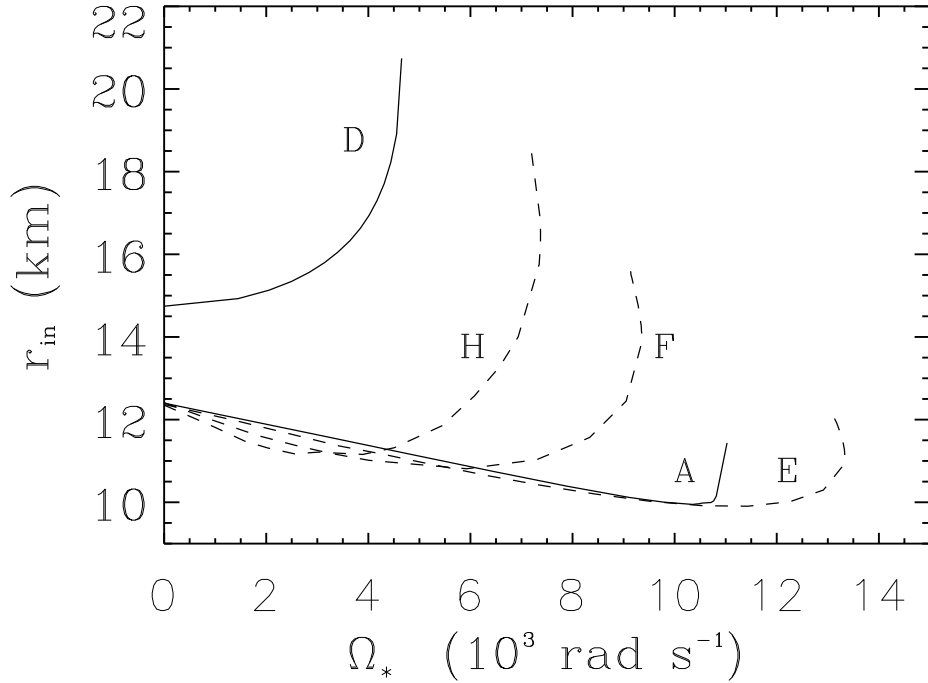


Figure 7.6: Disk inner edge radius (r_{in}) as a function of angular speed Ω_* of the compact star. The curves have their usual meaning.

to the non-monotonic behavior of Ω_* from slow rotation to mass-shed limit for SS EOSs, making the curves turn inward at the terminal (mass-shed) rotation rate.

In Fig. 7.10, we make a comparison between SSs and NSs for the same quantities displayed in Fig. 7.9. We have used three SS EOSs and two NS EOSs models (the softest and the stiffest for each case and the EOS model F). In all the panels, SS and NS both are seen to have their own exclusive regions in the high and low Ω_* parameter space respectively. This is especially prominent for E_{BL} and $E_{\text{BL}}/E_{\text{D}}$. We also notice that for SS, at $\Omega_* = \Omega_*^{\text{max}}$, the values of $E_{\text{BL}} \approx 0.05$ and $E_{\text{BL}}/E_{\text{D}} \approx 1.0$ for all EOS. On the contrary, for neutron stars, both E_{BL} and $E_{\text{BL}}/E_{\text{D}}$ become ≈ 0 at Ω_*^{max} ($= \Omega_{\text{ms}}$).

7.4 Summary and Discussion

In this chapter we have calculated the structure parameters and the disk temperature profiles for rapidly rotating SSs (for constant gravitational mass sequence with $M = 1.4 M_{\odot}$) and compared

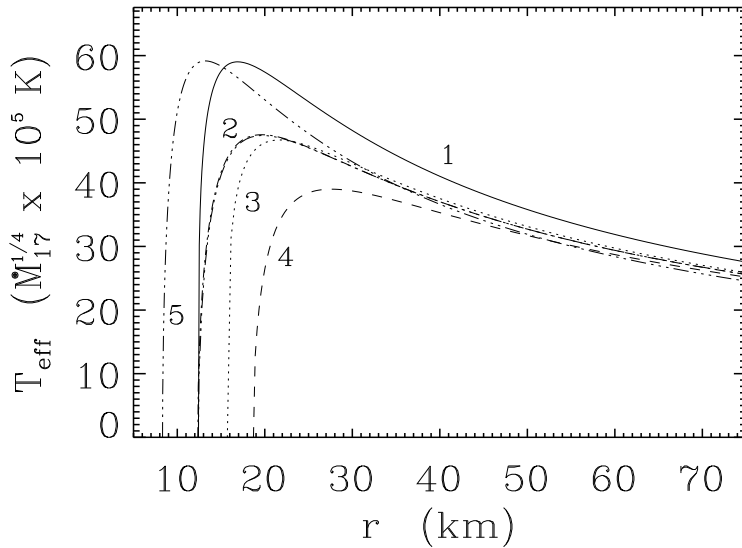


Figure 7.7: Accretion disk temperature profiles: Curve (1) corresponds to the Newtonian case, curve (2) to the Schwarzschild case (coincident curves for NS EOS model B and SS EOS model H), curve (3) to a neutron star (EOS model B) rotating at the centrifugal mass-shed limit and curve (4) to a strange star (EOS model H) rotating at the centrifugal mass-shed limit. For curve (1) it is assumed that, $r_{\text{in}} = 6GM/c^2$. The curves (1–4) are for a fixed gravitational mass ($M = 1.4 M_{\odot}$) of the compact star. Curve (5) corresponds to a configuration that has $M = 1 M_{\odot}$ and Ω_* corresponding to a period $P = 2.75$ ms (inferred for 4U 1728-34; see text) and described by EOS model E. In this and all subsequent figures, the temperature is expressed in units of $\dot{M}_{17}^{1/4} \times 10^5$ K, where \dot{M}_{17} is the steady state mass accretion rate in units of 10^{17} g s $^{-1}$.

them with those for NSs with the aim of finding possible ways to distinguish between the two. For the sake of completeness, we have compared the properties of these two types of stars all the way from slow rotation to mass-shed limit.

The striking feature of SSs is the non-monotonic behavior of Ω_* with J such that Ω_*^{max} occurs at lower value of J than that of the mass-shed limit. Hence the other SS structure parameters become non-monotonic functions of Ω_* . This behavior is observed even for the constant rest mass sequences of SSs (e.g. Gourgoulhon et al 1999; Bombaci et al. 2000). In contrast, for NSs, the structure parameters are all monotonic functions of Ω_* . An implication of the non-monotonic behavior of Ω_* with J is that if an isolated sub-millisecond pulsar is observed to be spinning up, it is likely to be an SS rather than an NS.

Because of higher values of T/W ($\gtrsim 0.2$), SSs are more prone to secular instabilities compared to NSs at rapid rotation (Gourgoulhon et al. 1999). Our calculations show that at Ω_*^{max} , $T/W > 0.2$.

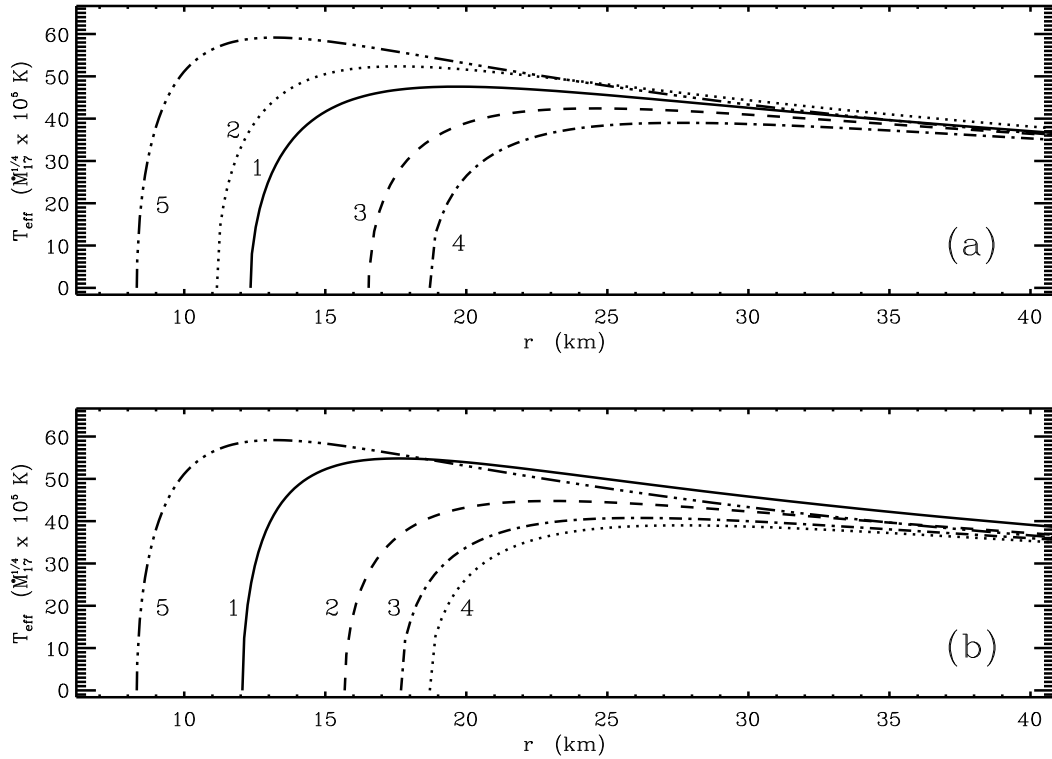


Figure 7.8: Temperature profiles incorporating the effects of rotation of the strange star. The plots correspond to (a) EOS model H and an assumed strange star mass of $M = 1.4 M_{\odot}$ (curves 1–4) for rotation rates: $\Omega_* = 0$ (curve 1), $\Omega_* = 3.891 \times 10^3 \text{ rad s}^{-1}$ (curve 2), $\Omega_* = 7.373 \times 10^3 \text{ rad s}^{-1}$ (curve 3), $\Omega_* = 7.163 \times 10^3 \text{ rad s}^{-1} = \Omega_{\text{ms}}$ (curve 4), (b) the same assumed mass and $\Omega_* = \Omega_{\text{ms}}$ for the four EOS models (E):curve 1, (F):curve 2, (G):curve 3 and (H):curve 4. In both panels, curve (5) is the same as that in Fig. 7.7.

Another important feature of SS gravitational mass sequence (in contrast to the corresponding NS sequences) is the crossing point in Ω_* and Ω_{in} . This feature has important implication in models of kHz QPOs: for example if Ω_* is greater than Ω_{in} , the beat-frequency models ascribing higher frequency to Keplerian frequencies will not be viable.

It can be noted from Fig. 7.4, that with the increase in stiffness of the EOS models, J_{cross} increases and $\Omega_{*,\text{cross}}$ (the subscript “cross” corresponds to the point $\Omega_{\text{in}} = \Omega_*$) decreases monotonically. It is also seen that in general all the quantities vary monotonically with the stiffness for both SS and NS EOSs (see Chapter 3).

For SSs, the inner-edge of the accretion disk rarely touches the surface of the star (even for maximum rotation rates), while for rapidly rotating NSs, the accretion disk extends upto the stellar surface for almost all rotation rates. Since the inner accretion disk boundary condition is different

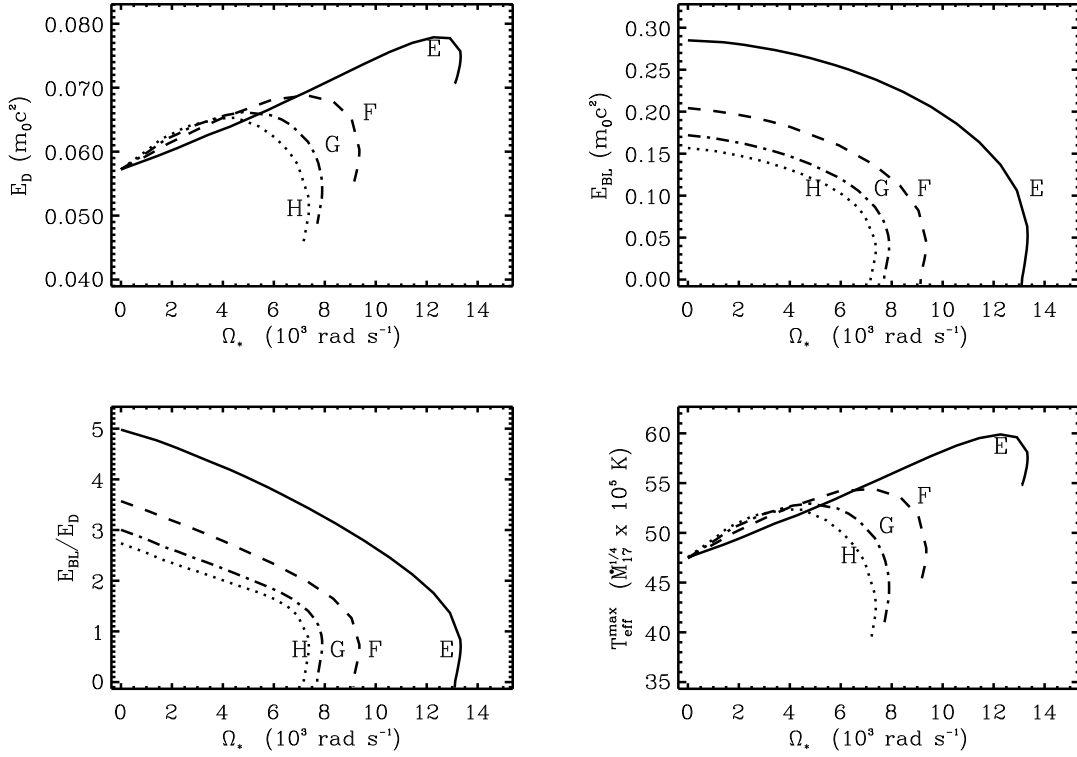


Figure 7.9: The variations of the E_D , E_{BL} , E_{BL}/E_D and $T_{\text{eff}}^{\text{max}}$ with Ω_* for a chosen strange star mass value of $1.4 M_\odot$ for the four SS EOS models. The curves have the same significance as Fig. 7.3.

for both these cases, we expect important observable differences (both temporal and spectral) in X-ray emission (from the boundary layer and the inner accretion disk) from SSs and NSs.

A brief note on the variation of r_{orb} with specific angular momentum is in order here. As mentioned earlier, beyond a certain value of the angular momentum, the radius of the ISCO increases with increasing angular momentum – a property not seen either in the case of NSs or black holes. The reason for this can be traced to the radial gradient of the angular velocity of the particles at the marginally stable orbit and the analysis is described as follows:

For the metric described by Eq. (2.3), the second derivative of the effective potential is given by Eq. (2.47). Simplification of this, using the other equations of motion (Bardeen 1970), yield

$$r^2(1 - \tilde{v}^2)\tilde{V}_{,rr} = -X \left[\frac{r\Omega_{,r}}{\Omega - \omega} + \frac{1 - \tilde{v}^2}{2\tilde{v}^2}X \right] \quad (7.1)$$

where Ω is the angular speed of the particle and $X = \tilde{v}^2(2 + r\gamma_{,r} - r\rho_{,r}) + r(\gamma_{,r} + \rho_{,r})$. The marginal stability criterion, therefore, yields the rate of change of the marginal stable orbit, with respect to

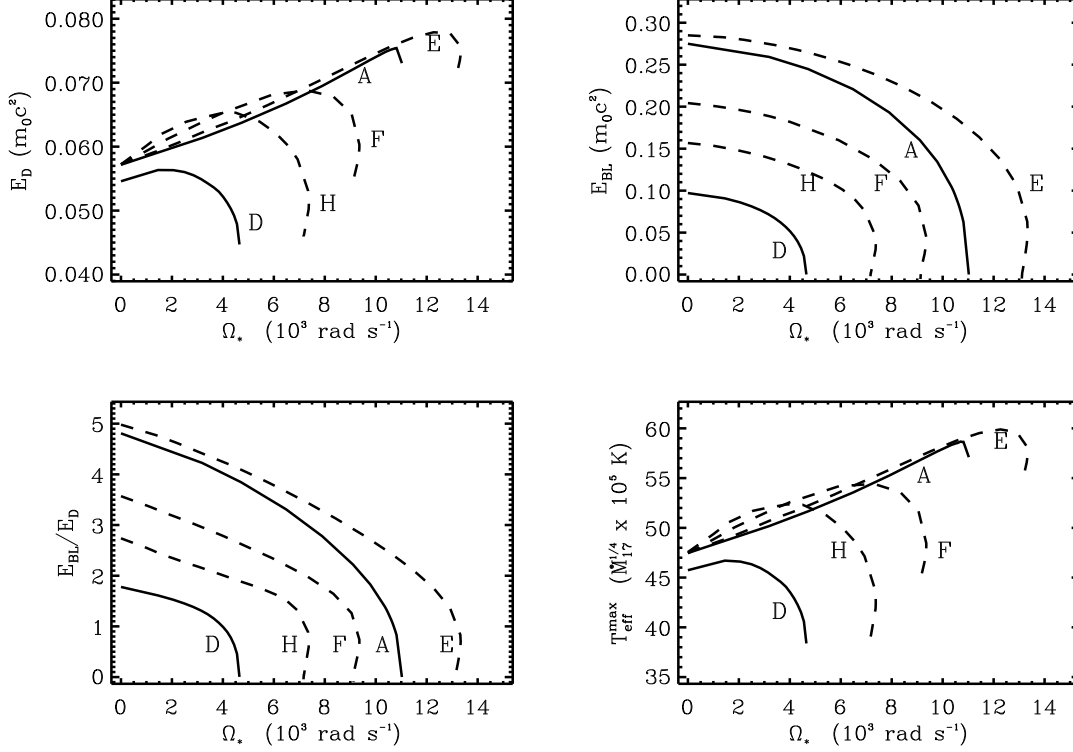


Figure 7.10: Same as Fig. 7.9, except the fact that here two NS EOS models and three SS EOS models are used. The curves have the same significance as Fig. 7.6.

j ($= J/M^2$) as:

$$r_{\text{orb},j} = r_{\text{orb}} \left\{ \frac{(\Omega - \omega)_{,j}}{\Omega - \omega} - \frac{\Omega_{,rj}}{\Omega_{,r}} + 2 \frac{\tilde{v}_{,j}}{\tilde{v}(\tilde{v}^2 - 1)} + \frac{X_{,j}}{X} \right\} \quad (7.2)$$

where the terms in the bracket are to be evaluated at r_{orb} . We calculate the four terms in the bracket in Eq. (7.2) and find that the second term dominates the net rate of change of r_{orb} with j . This implies that at the value of j where $r_{\text{orb},j}$ changes sign, although the first three terms are observed to change sign, the net sign is only dependent on that of $\Omega_{,rj}$ at ISCO.

From Fig. 7.6 we see that for Ω_* in the range $(0, 4028)$ rad s^{-1} (the second quantity in the range is the rotation rate of PSR 1937+21: Backer et al. 1982, the fastest rotating pulsar observed so far), a major portion of the $r_{\text{in}}-\Omega_*$ space is occupied exclusively by NS. So if r_{in} can be determined independently from observations (for example, by fitting the soft component of the observed spectrum by the XSPEC model “diskbb” available in XANADU: see for example Kubota et al 1998, or, from the observed kHz QPO frequencies), there is a fair chance of inferring the central accretor to be an NS rather than an SS (provided the mass of the central accretor is known by other means). This is also applicable to E_{BL} and $E_{\text{BL}}/E_{\text{D}}$ (Fig. 7.10). It is also to be noted

that Li et al. (1999 a; 1999b) did a similar search in the $M - R$ parameter space and concluded the millisecond X-ray pulsar SAX J1808.4-3658 and the central accretor in 4U 1728-34 to be likely SSs. If, indeed this is true, then it is possible to constrain the *stiffness* of the equation of state of SQM (Bombaci 2000), and to exclude EOS models (like EOS G and EOS H) stiffer than our EOS model F.

Calculation of the accretion disk spectrum involves the temperature profiles as inputs. The spectra of accretion disks, incorporating the full effects of general relativity for NSs (Chapters 5, 6) show sensitive dependence on the EOS of high density matter. However, the similarity in the values of the maximum disk temperature implies an indistinguishability between the spectra of SSs and those of NSs in general. Nevertheless, just as E_{BL} and other quantities show that NS exclusively occupy certain regions in the relevant parameter space, we expect that it will be possible to make a differentiation between these two compact objects by modeling the boundary layer emission. If as mentioned in previous paragraph, we exclude EOS models stiffer than F, then from Fig. 7.10, we see that a fairly accurate measurement of E_{BL} ($L_{\text{BL}}/\dot{M}c^2$) and Ω_* can indicate whether the central accretor is an NS or an SS if the corresponding point falls outside the strip defined by curves F and A.

The current uncertainties in theoretical models of boundary layer emission and the variety of cases presented by models of rotating compact objects, calls into order a detailed investigation into these aspects of LMXBs – especially with the launch of new generation X-ray satellites (having better sensitivities and larger collecting areas) on the anvil.

Chapter 8

Summary and Conclusion

8.1 Introduction

The X-ray binary systems consist of two stars, rotating around each other. One of them (primary) is a compact star (neutron star, strange star or black hole) and the other one (secondary companion) is a main-sequence star or an evolved star (red sub-giant, blue super-giant or white dwarf). When the companion star fills its Roche-lobe, matter from its surface flows towards the compact star. Due to initial angular momentum, this matter can not fall radially; rather it follows a spiral path and forms a disk. Such a disk is called an accretion disk. Due to viscous dissipation, energy is radiated from the disk. As the temperature of the inner portion of the disk is very high ($\sim 10^6$ K), X-rays are generated in this region. If the compact star has a hard surface (i.e., if it is not a black hole), the inflowing matter hits this surface and another component of X-ray is produced in a thin layer, called the boundary layer. However, it is to be remembered that the disk accretion is not the only mechanism for accretion process. Such a process can also happen from the wind of the companion star.

There are two classes of X-ray binary systems: HMXBs and LMXBs. The secondary companion in an HMXB is a high mass star (generally, O or B type). As mentioned in Chapter 1, the age of such a system is rather low ($\sim 10^7$ yrs). Most of the energy coming out of such systems is in the visible range. On the other hand, an LMXB consists of a low mass ($\lesssim 1M_{\odot}$) companion star, with the age typically $\sim 10^9$ yrs and most of its radiated energy is in X-rays.

For our work, we have chosen LMXB systems with neutron stars or strange stars as the central accretors. These systems offer several advantages over the HMXBs in understanding the properties of the compact stars. For example, most of the energy (in X-rays) from such systems come from the inner regions of accretion disks. The motion of matter in these regions is expected to be influenced

by the mass–radius relation and the total angular momentum of the compact star. Therefore, the analysis of X–ray spectra from these systems may shed light on the properties of the compact stars. Moreover, the accretion disks of such systems may extend very close to the stellar surface, as the magnetic fields of the primary stars in LMXBs are expected to be decayed to lower values ($\sim 10^8$ G; see Bhattacharya & Datta 1996 and Bhattacharya & van den Heuvel 1991). This ensures that the observed spectra can actually reflect some properties of the compact stars. Besides, accretion via wind is negligible in LMXBs, which may make the spectral calculation for such systems simpler than that for HMXBs.

LMXBs exhibit many complex spectral and temporal behavior. It is a challenge to explain these phenomena using theoretical models. However, most of the existing models for spectral fitting are Newtonian. But near the surface of a compact star, the accretion flow is expected to be governed by the laws of general relativity due to the presence of strong gravity. Therefore general relativistic models should be used for the purpose of fitting to get the correct best-fit values of the parameters. Besides, the principal motivation behind the study of the spectral and temporal behaviors of compact star LMXBs is to understand the properties of very high ($\sim 10^{15}$ g cm $^{-3}$) density matter at the compact star core (van der Klis 2000). This is a fundamental problem of physics, which can not be addressed by any kind of laboratory experiment. The only way to answer this question is to assume an equation of state (EOS) model for the compact star core, to calculate the structure parameters of the compact star and then to calculate an appropriate spectral model. By fitting such models (for different chosen EOSs) to the observational data, one can hope to constrain the existing EOS models and hence to understand the properties of high density matter. However, general relativistic calculation is essential to calculate the structure parameters of a compact star and therefore to constrain the EOS models.

It is expected that the compact stars in LMXBs are rapidly rotating due to accretion-induced angular momentum transfer. LMXBs are thought to be the progenitors of milli-second (ms) radio pulsars (Bhattacharya & van den Heuvel 1991) like PSR 1937+21 with $P \sim 1.56$ ms (Backer et al. 1982). The recent discovery of ms ($P \sim 2.49$ ms) X–ray pulsations in XTE J1808-369 (Wijnands & van der Klis 1998) has strengthened this hypothesis. Therefore it is necessary to calculate the structure of a rotating compact star considering the full effect of general relativity. This was done by Cook et al. (1994) and the same procedure was used by Thampan & Datta (1998) to calculate the luminosities of the disk and the boundary layer.

In our work, we have calculated the structure parameters of a rapidly rotating neutron star and the metric coefficients in and around it. Then we have computed disk temperature profiles and disk spectra for various EOS models and many (M, Ω_*) combinations. We have considered

the accretion disk to be geometrically thin and radiating locally like a blackbody. This may be the true case for luminous LMXBs, as shown by Mitsuda et al. (1984). These authors showed that the observed spectra of Sco X-1, 1608-52, GX 349+2 and GX 5-1, obtained with the *Tenma* satellite, can be well-fitted with the sum of a multicolor blackbody spectrum (possibly from the accretion disk) and a single temperature blackbody spectrum (believed to come from the boundary layer). Apart from the temperature profile, we have also calculated the disk luminosity and the boundary layer luminosity. Comparing the theoretical values of the luminosities and the disk temperature with the fitted values (fitted to *EXOSAT* data), we have constrained several properties of five LMXB sources: Cygnus X-2, XB 1820-30, GX 17+2, GX 9+1 and GX 349+2. We have also fitted the calculated spectra with an analytical function and tried to distinguish between Newtonian and general relativistic spectra.

It has been known for many years that the neutron star may in fact be a ‘hybrid star’ consisting of ordinary nuclear matter in the outer parts and quark matter in the central regions. This will be the case if *strange quark matter* (SQM; see Chapter 7 for discussion) is metastable at zero pressure, being stabilized relative to hadronic matter by the high pressure within a neutron star (Baym & Chin 1976; Chapline & Nauenberg 1976; Freedman & McLerran 1978). If SQM is absolutely stable at the zero pressure, an even more intriguing possibility opens up, namely the existence of strange stars consisting completely of SQM (Witten 1984; Haensel, Zdunik & Schaeffer 1986; Alcock, Farhi & Olinto 1986).

The identification of a strange star will prove that the so called *strange matter hypothesis* is true. According to this hypothesis, strange quark matter, in equilibrium with respect to the weak interactions, could be the actual ground state of strongly interacting matter rather than ^{56}Fe . This is a fundamental problem of physics, which may be solved only if it is possible to distinguish between a neutron star and a strange star.

Strange stars are expected to behave quite differently from neutron stars due to an unusual equation of state. But, even then, it is very difficult to distinguish between them. For example, more massive neutron stars have the lower values of radii, while this relationship is opposite for strange stars. Nevertheless, for a value of gravitational mass equal to $1.4M_{\odot}$ (the canonical mass for compact star candidates), the difference between the predicted radii of nonrotating configurations of a strange star and a neutron star comes out to be, at most, only about 5 km. It is very difficult to observe such a small value directly. Another distinction between strange stars and neutron stars was for a long time believed to be a much more rapid cooling of SQM due to neutrino emitting weak interactions involving the quarks (Alcock et al. 1986). Thus a strange star was presumed to be much colder than a neutron star of similar age, a signature potentially observable from X-ray

satellites. But recently the story has been complicated considerably by the finding that ordinary neutron β -decay may be energetically allowed in nuclear matter (Lattimer et al. 1991), so that the cooling rate may be comparable to that of SQM. There are other possible ways (for example, study of pulsar glitches, oscillation and maximum rotation rate of the stars) to distinguish between these two kinds of stars (see Madsen 1998 for discussions).

In Chapter 7, we have computed the structure parameters of a strange star and calculated the corresponding disk temperature profiles and luminosities. We have then compared these values with those for a neutron star and tried to distinguish between them.

In sections 8.2 and 8.3, we discuss the conclusions from the calculations of disk temperature profile and spectrum respectively. We give the summary of the work with strange stars in section 8.4. In section 8.5, we discuss the future prospects and in section 8.6, we give the final conclusion.

8.2 Disk Temperature Profile

We have calculated (in Chapter 3) the temperature profiles of (thin) accretion disks around rapidly rotating neutron stars (with low surface magnetic fields), taking into account the full effects of general relativity. We have also computed the corresponding disk luminosities and boundary layer luminosities. All of these have been calculated as functions of M and Ω_* for various EOS models.

It is important to notice (as shown in Fig. 3.3a) that the disk temperature profiles do not have a monotonic behavior with respect to Ω_* . This is a result of two mutually opposing effects: (1) the energy flux emitted from the disk increases with Ω_* and (2) the nonmonotonic nature of the dependence of r_{in} on Ω_* (see Fig. 3.1). Such a behavior of temperature profiles is reflected on disk spectra and one has to be careful when trying to constrain Ω_* by spectral fitting.

We have then considered a model (in Chapter 4) for the spectrum of the X-ray emission from the disk, parameterized by the mass accretion rate, the color temperature and the rotation rate of the neutron star. We derive constraints on these parameters for the LMXB sources: Cygnus X-2, XB 1820-30, GX 17+2, GX 9+1 and GX 349+2, using the estimates of the maximum temperature in the disk along with the disk and boundary layer luminosities, taking the spectrum inferred from the *EXOSAT* data.

Our calculations suggest that the neutron stars in Cygnus X-2 and GX 9+1 rotate close to the centrifugal mass-shed limit. The LMXB source GX 349+2 also contains a rapidly rotating neutron star. This is in accord with the belief that LMXBs are the progenitors of milli-second radio pulsars. Such a result also shows that the inclusion of rapid rotation in the neutron star structure-parameter-calculation is very important. However at this point it should be mentioned that using a scalar

theory of gravitation, Papaloizou & Pringle (1978) have concluded that a neutron star rotating with a frequency close to 1 kHz may be unstable to the radiation of gravitational waves by non-radial stellar modes.

We have also discussed the possible constraints on the neutron star equation of state. We could not actually rule out any EOS model, but looking at the QPO frequencies, gravitational masses (M) and color factors (f) for the sources, we have tried to conclude what kind EOS models could best represent the true EOS of a neutron star (see Chapter 4). According to our results, soft and stiff EOS models are unfavored, i.e., the EOS models with intermediate stiffnesses are supported.

In our work, we have not tried to model the observational temporal behaviors of the sources, and in particular, the QPO observations. Our results do not tally with the simple beat-frequency model. However, a pure beat-frequency model has been called into question because of several observations (see section 4.4 for a brief discussion).

In our analysis, we have assumed that the boundary layer does not affect the inner region of the disk. This approximation will be valid when the boundary layer luminosity is smaller than the disk luminosity and the boundary layer extent is small compared to the radius of the star. This has been shown to be true for the chosen LMXB sources (see section 4.4).

It is to be remembered that in our calculations, we have neglected the effect of neutron star's magnetic field on the accretion flows. Therefore, our results are valid if the Alfvén radius is less than the radius of the inner edge of the accretion disk. As we have seen in Chapter 4, this requires the upper limit of the surface magnetic field of the neutron star to be $\sim 10^8$ G, which is a reasonable value for LMXBs.

8.3 Disk Spectrum

We have computed X-ray spectra (in Chapter 5), as seen by a distant observer, from the accretion disk around a rapidly rotating neutron star. Our calculations have been carried out in a fully general relativistic framework, with exact treatment of rotation. We have taken into account the Doppler shift, gravitational redshift and light bending effects in order to compute the observational spectrum. For this purpose, we have computed the differential equations of motion for photons (Eqs. 5.7 - 5.11) in a space-time specified by the metric given by Eq. (2.3). Then the paths of the photons have been backtracked for the calculation of the disk spectrum (see section 5.3 for the description of the procedure). We have calculated the spectrum as a function of M and Ω_* for various EOS models.

We have found that light-bending significantly modifies the high-energy part of the spectrum.

It can be seen (see Fig. 5.1) that the inclusion of light-bending effect enhances the predicted flux from the disk. This is because, due to light-bending, the disk subtends a larger solid angle to the observer than it otherwise would. We also see (from Fig. 5.2) that the spectrum, specially the high energy part, is very sensitive to the accretion rate. This may be useful for constraining the accretion rate by fitting the observational data with our model.

The inclination angle i is a very important parameter in determining the shape of the spectrum. For lower energies, the observed flux is higher for lower values of i , while this effect is opposite at higher energies due to Doppler blue shift. We can also notice (from Fig. 5.4) that the behavior of the disk spectrum is not monotonic with Ω_* . This is expected from the non-monotonic behavior of the disk temperature profile. We can also expect to constrain EOS models by spectral fitting, as the disk spectrum is fairly sensitive to the chosen EOSs. However, as the spectrum is a function of a large number of free parameters, it is very difficult to constrain the equations of state in a decisive way. But, it may actually be possible with the data of new generation X-ray satellites with very good spectral resolution.

The calculations presented here deal only with the thin Keplerian blackbody disk. In reality, there may be other X-ray emitting components (boundary layer, accretion disk corona etc.) present in the LMXB source. In addition to that the disk may not be thin, Keplerian or a blackbody. Our results will change for such cases. For example, our temperature profile and hence the spectrum will not be valid for a non-Keplerian disk. The effect of such uncertainty of the nature of the source may be more important than the effect of general relativity and rapid rotation. However, there is no competition between these two kinds of effects. General relativistic modifications should be considered to calculate the spectra from all the X-ray emitting components to have the full general relativistic spectrum of a source. However, as this is a first step for this kind of work, we choose the simplest system, i.e., a thin blackbody disk.

As mentioned in section 5.5, our results for non-rotating neutron stars did not match with those of the spectral fitting routine *GRAD*. With the help of Ebisawa & Hanawa (*private communication*) we traced this mismatch to certain simplifying approximations, as well as a couple of errors made in the *GRAD* code.

The computation of our model spectrum is rather time-consuming and therefore not quite suited to routine use. To facilitate direct comparison with observations, we have presented a simple empirical function which describes the numerically computed relativistic spectra well. This empirical function (which has three parameters including normalization) also describes the Newtonian spectrum adequately. Thus the function can in principle be used to distinguish between the two. In particular, the best-fit value of one of the parameters (β -parameter) is ≈ 0.4 for the Newtonian

case, while it ranges from 0.1 to 0.35 for relativistic case depending upon the inclination angle (if i is not too high), EOS, spin rate and mass of the neutron star. Constraining this parameter by fits to future observational data of X-ray binaries may, therefore, indicate the effect of strong gravity in the observational spectrum.

8.4 Strange Star

We have computed the temperature profiles of accretion disks around rapidly rotating strange stars, using constant gravitational mass equilibrium sequences of these objects, considering the full effect of general relativity. We have also calculated the corresponding disk luminosity, the boundary layer luminosity and the bulk structure parameters for the strange stars. These results have been compared with those for neutron stars.

The striking feature of strange stars is the non-monotonic behavior of Ω_* with J such that Ω_*^{\max} occurs at a lower value of J than that of the mass-shed limit. For neutron stars, such a thing never occurs. Therefore, if an isolated sub-millisecond pulsar is observed to be spinning up, it is likely to be a strange star rather than a neutron star.

Because of higher values of T/W ($\gtrsim 0.2$), the tendency of strange stars to be unstable to triaxial instability is larger than neutron stars in rapid rotation. Another interesting aspect of strange stars is that their gravitational mass sequences (in contrast to the corresponding neutron star sequences) for Ω_* and Ω_{in} (see Chapter 7 for the meanings of the symbols used) cross at some point. This may have importance in kHz QPO modeling, as mentioned in Chapter 7. It can also be noticed that for strange stars, the accretion disk seldom touches the surface of the star (even for very high rotation rates), while for rapidly rotating neutron stars, the disk almost always extends upto the stellar surface. This may have important observational effects as mentioned in Chapter 7.

Beyond a certain critical value of stellar angular momentum (J), we observe the radius (r_{orb}) of the innermost stable circular orbit (ISCO) to increase with J (a property seen neither in rotating black holes nor in rotating neutron stars). The reason for this is traced to the crucial dependence of dr_{orb}/dJ on the rate of change of the radial gradient of the Keplerian angular velocity at r_{orb} with respect to J .

The temperature profiles obtained are compared with those of neutron stars, as an attempt to provide signatures for distinguishing between the two. We show that when the full gamut of strange star equation of state models, with varying degrees of stiffness are considered, there exists a substantial overlap in properties of both neutron stars and strange stars. However, we also notice that neutron stars and strange stars exclusively occupy certain parameter spaces. This result

implies the possibility of distinguishing these objects from each other by sensitive observations through future X-ray detectors.

8.5 Future Prospects

Our work may be considered as a first step in understanding the effect of both general relativity and rapid rotation on the properties of accretion disk. For the sake of simplicity, we have assumed the accretion disk to be thin and a blackbody. Now, as a future project, this work may be extended to the other kinds of disks (optically thin, geometrically thick, non-Keplerian etc.). The effect of rapid rotation can also be estimated for the other possible X-ray emitting regions, such as, boundary layer, disk corona etc., following the same procedure mentioned here.

We observe broadened iron lines from LMXBs such as Cygnus X-2, GX 349+2 etc. An intrinsically narrow iron line emitted by an accretion disk around a compact star is believed to be broadened and skewed by Doppler effect and gravitational redshift. As a result, the fitting of the line components of the observed spectra by proper theoretical model should reveal the nature of the flow of matter near the compact star's surface and help us to constrain the equation of state of the compact star. It is, therefore, very important to calculate the structure of the broadened line as a function of the compact star's angular speed and other parameters for various EOS models, using the metric given by Eq. (2.3).

So far we have not considered the effect of the magnetic field (of the compact star) on the accretion disk, assuming that it has been decayed to a very small value ($\approx 10^8$ G). But the magnetic field may play some role in determining the flow of the accreted matter near the surface of the compact star. It is, therefore, instructive to look into this problem and include the effect of magnetic field in calculating the accretion disk spectrum.

In order to calculate the full spectrum of an LMXB source, it is necessary to compute the spectrum of the boundary layer. One should model this spectrum (specially during the Type I Burst) using the metric coefficients suitable for a rapidly rotating compact star. Addition of this spectrum to the accretion disk spectrum (we have already calculated) may give the full spectrum from LMXBs.

For a compact star which is not rotating close to the mass-shed limit, the boundary layer luminosity is fairly high. The inner region of the disk around such a compact star may, therefore, be radiation pressure dominated. It is necessary to calculate the spectrum from such a disk for the space-time geometry appropriate for a rapidly rotating compact star.

Once the spectrum of an LMXB is calculated considering all the major effects described above,

one can, in principle, fit the observational data by this model spectrum and constrain the equation of state and the parameters of the source effectively. However, computation of such a general relativistic spectrum is time-consuming and rather unsuitable for the fitting procedure. Therefore, it is important to do a series of parametric fits to this spectrum for making it available for routine spectral fitting work.

8.6 Final Conclusion

The main purpose of the study of the properties of an LMXB with a neutron star or a strange star as the central accretor is to understand the properties of very high density matter and to address the question of the existence of strange quark matter. These can be achieved only by fitting the observed spectral and temporal behavior of such sources with appropriate theoretical models. It is not possible to incorporate all the important factors in such a model in a single work and one should proceed step by step. In our work, we have included two major factors, namely, the effects of general relativity (essential for constraining EOS) and rapid rotation, which we think is a step forward towards our aim.

Bibliography

- Alcock, C., Farhi, E., Olinto, A. 1986, ApJ, 310, 261
- Alpar, M.A., & Shaham, J. 1985, Nature, 316, 239
- Asaoka, I. 1989, PASJ, 41, 763
- Backer, D.C., Kulkarni, S.R., Heiles, C., Davis, M.M., & Goss, W.M. 1982, Nature, 300, 615
- Baldo, M., Bombaci, I., & Burgio, G.F. 1997, A&A, 328, 274
- Bardeen, J.M. 1970, ApJ, 162, 71
- Bardeen, J.M., & Wagoner, R.V. 1971, ApJ, 167, 359
- Baym, G., & Chin, S.A. 1976, Nucl. Phys. A 262, 527
- Baym, G., & Pethick, C. 1975, Ann. Rev. Nucl. Sci., 25, 27
- Baym, G., & Pethick, C., & Sutherland, P.G. 1972, ApJ, 170, 299
- Belian, R.D., Conner, J.P., & Evans, W.D. 1976, ApJ Lett., 206, 135
- Bhattacharya, D., & Datta, B. 1996, MNRAS, 282, 1059
- Bhattacharya, D., & van den Heuvel, E.P.J. 1991, Phys. Repts., 203, 1
- Blosler, P.F., Grindlay, J.E., Kaaret, P., Zhang, W., Smale, A.P., & Barret, D. 2000, ApJ, 542, 1000
- Bodmer, A.R. 1971, Phys. Rev. D, 4, 1601
- Borozdin, K., Revnivtsev, M., Trudolyubov, S., Shrader, C., & Titarchuk, L. 1999, ApJ, 517, 367
- Bulik, T., Gondek-Rosinska, D., & Kluźniak, W. 1999, A&A, 344, L71

-
- Bombaci, I., & Datta, B. 2000, *ApJ*, 530, L69
 - Bombaci, I., Thampan, A.V., & Datta, B. 2000, *ApJ*, 541, L71
 - Bonazzola, S.,ourgoulhon, E., Salgado, M., & Marck, J.A. 1993, *A&A*, 278, 421
 - Bonazzola, S., Schneider, J. 1974, *ApJ*, 191, 273
 - Burderi, L., & King, A.R. 1998, *ApJ*, 505, L135
 - Butterworth, E.M. 1976, *ApJ*, 204, 561
 - Butterworth, E.M. & Ipser, J.R. 1976, *ApJ*, 204, 200
 - Campana, S., Colpi, M., Mereghetti, S., Stella, L., & Tavani, M. 1998, *A&A, Rev.*, 8, 279
 - Canuto, V. 1974, *Ann. Rev. Astr. Astrophys.*, 12, 167
 - Canuto, V. 1975, *Ann. Rev. Astr. Astrophys.*, 13, 335
 - Chakrabarti, S.K., & Titarchuk, L.G. 1995, *ApJ*, 455, 623
 - Chandrasekhar, S. 1983, in “The Mathematical Theory of Black Holes” (Oxford University Press, London)
 - Chapline, G. & Nauenberg, M. 1976, *Nature*, 264, 23
 - Cheng, K. S., Dai, Z. G. 1996, *Phys. Rev. Lett.*, 77, 1210
 - Cook, G.B., Shapiro, S.L., & Teukolsky, S.A. 1994, *ApJ*, 424, 823
 - Czerny, B., Czerny, M., & Grindlay, J.E. 1986, *ApJ*, 311, 241
 - Datta, B. 1988, *Fund. Cosmic Phys.*, 12, 151
 - Datta, B., & Alpar, M.A. 1993, *A&A*, 275, 210
 - Datta, B., & Ray, A. 1983, *MNRAS*, 204, 75
 - Datta, B., Thampan, A.V., & Bombaci, I. 1998, *A&A*, 334, 943
 - Datta, B., Thampan, A.V., & Bombaci, I. 2000, *A&A*, 355, L19
 - Datta, B., Thampan, A.V., & Wiita, P. 1995, *J. Ap. Astr.*, 16, 357
 - Deutsch, E.W., Margon, B., Anderson, S.F., Wachter, S., & Goss, W.M. 1999, *ApJ*, 524, 406

-
- Dey, M., Bombaci, I., Dey, J., Ray, S., & Samanta, B.C. 1998, *Phys. Lett. B*, 438, 123; erratum *Phys. Lett. B*, 467, 303
 - Dove, J.B., Wilms, J., & Begelman, M.C. 1997, *ApJ*, 487, 747
 - Ebisawa, K., Mitsuda, K., & Hanawa, T. 1991, *ApJ*, 367, 213
 - Ebisuzaki, T. 1987, *PASJ*, 39, 287
 - Farhi, E., & Jaffe, R.L. 1984, *Phys. Rev. D*, 30, 2379
 - Feynman, R.P., Metropolis, N., & Teller, E. 1949, *Phys. Rev.*, 75, 1561
 - Frank, J., King, A.R., & Raine, D.J. 1992, in *Accretion Power in Astrophysics* (Cambridge Univ. Press)
 - Freedman, B. & McLerran, L. 1978, *Phys. Rev. D*, 17, 1109
 - Friedman, J.L., Ipser, J.R., & Parker, L. 1986, *ApJ*, 304, 115
 - Giacconi, R., Gursky, H., Paolini, F.R., & Rossi, B.B. 1962, *Phys. Rev. Lett.*, 9, 439
 - Glendenning, N.K. 1997, in *Compact Stars: Nuclear Physics, Particle Physics and General Relativity* (New York: Springer-Verlag)
 - Goldman, I. 1979, *A&A*, 78, L15
 - Gondek-Rosinska, D., Bulik, T., Zdunik, L., Gourgoulhon, E., Ray, S., Dey, J., & Dey, M. 2000, *A&A*, 363, 1005
 - Gondek, D., Haensel, P., & Zdunik, J. L. 1998, in *ASP Conf. Ser. 138, 1997, Pacific Rim Conference on Stellar Astrophysics*, ed. K. L Chan, K. S. Cheng, H. P. Singh, 131
 - Gondek, D., Haensel, P., & Zdunik, J.L. 1997, *A&A*, 325, 217
 - Gondek, D. & Zdunik, L. 1999, *A&A*, 344, 117
 - Gourgoulhon, E., Haensel, P., Livine, R., Paluch, E. et al. 1999, *A&A*, 349, 851
 - Goussard, J. O., Haensel, P., & Zdunik, J. L. 1998, *A&A*, 330, 1005
 - Grindlay, J., Gursky, H., Schnopper, H., Parsignault, D. et al. 1976, *ApJ Lett.*, 205, 127
 - Haensel, P., Zdunik, J.L., & Schaeffer, R. 1986, *A&A*, 160, 121

-
- Haberl, F., & Titarchuk, L. 1995, *A&A*, 299, 414
 - Hanawa, T. 1989, *ApJ*, 341, 948
 - Hartle, J.B., & Thorne, K.S. 1968, *ApJ*, 153, 807
 - Hertz, P., Norris, J.P., Wood, K.S., Vaughan, B.A. & Michelson, P.F. 1990, *ApJ*, 354, 267
 - Itoh, N., 1970, *Prog. Theor. Phys.*, 44, 291
 - Jastrow, R. 1955, *Phys. Rev.*, 98, 1479
 - Jones, C. 1977, *ApJ*, 214, 856
 - Joss, P.C. 1978, *ApJ*, 225, 123
 - King, A.R., Kolb, U., & Burderi, L. 1996, *ApJ*, 464, L127
 - Kluźniak, W., & Wagoner, R.V. 1985, *ApJ*, 297, 548
 - Knigge, C. 1999, *MNRAS*, 309, 409
 - Komatsu, H., Eriguchi, Y., & Hachisu, I. 1989, *MNRAS*, 237, 355
 - Konar, S. 2000, *Bull. Astr. Soc. India*, 28, 343
 - Kopal, Z. 1959, in *Close Binary Systems* (Chapman and Hall, London)
 - Kubota A., Tanaka Y., Makishima K., et al. 1998, *PASJ*, 50, 667
 - Landau, L.D., & Lifshitz, E.M. 1987, in “*Fluid Mechanics*” (Second Edition, Oxford: Pergamon Press)
 - Lattimer, J.M., Pethick, C.J., Prakash, M., & Haensel, P. 1991, *Phys. Rev. Lett.*, 66, 2701
 - Lewin, W.H.G, Doty, J., Clark, J.W., Rappaport, S.A. et al. 1976, *ApJ*, 207, 95
 - Li, X.-D., Bombaci, I., Dey, M., Dey, J., & van den Heuvel, E.P.J. 1999a, *Phys. Rev. Lett.*, 83, 3776
 - Li, X.-D., Ray, S., Dey, J., Dey, M., & Bombaci, I. 1999b, *ApJ*, 527, L51
 - Link, B., Epstein, R.I., & van Riper, K.A. 1992, *Nature*, 359, 616
 - London, R.A., Taam, R.E., & Howard, W.M. 1986, *ApJ*, 306, 170

- Lu, T. 1998, in ASP Conf. Ser. 138, 1997, Pacific Rim Conference on Stellar Astrophysics, ed. K.L Chan, K.S. Cheng, H.P. Singh, 215, [astro-ph/9807052](#)
- Luminet, J.P. 1979, *A&A*, 75, 228
- Madsen, J. 1998, *Phys. Rev. Lett.*, 81, 3311
- McNamara, D.H., Madsen, J.B., Barnes, J., & Ericksen, B.F. 2000, *PASP*, 112, 202
- Méndez, M., & van der Klis, M. 1999, *ApJ*, 517, L51
- Miller, M.C., & Lamb, F.K. 1996, *ApJ*, 470, 1033
- Misner, C.W., Thorne, K.S., & Wheeler, A.J. 1973, *Gravitation* (San Francisco: Freeman)
- Mitsuda, K., Inoue, H., Koyama, K., Makishima, K. et al. 1984, *PASJ*, 36, 741
- Negele, J.W., & Vautherin, D. 1973, *Nucl. Phys.*, A207, 298
- Novikov, I.D., & Thorne, K.S. 1973, in *Black Holes*, ed. Dewitt, C. & Dewitt, B.S. (New York: Gordon and Breach), 343
- Olinto, A. 1987, *Phys. Lett. B*, 192, 71
- Oppenheimer, J.R., & Volkoff, G.M. 1939, *Phys. Rev.*, 55, 374
- Orosz, J.A., & Kuulkers, E. 1999, *MNRAS*, 305, 132
- Osherovich, V.A. & Titarchuk, L.G. 1999a, *ApJ*, 522, L113
- ———. 1999b, *ApJ*, 523, L73
- Page, D.N., & Thorne, K.S. 1974, *ApJ*, 191, 499
- Pandharipande, V.R. 1971, *Nucl. Phys.* A178, 123
- Papaloizou, J., & Pringle, J.E. 1978, *MNRAS*, 184, 501
- Popham, R., & Sunyaev, R.A. 2000, [astro-ph/0004017](#)
- Psaltis, D., & Chakrabarty, D. 1999, *ApJ*, 521, 332
- Rappaport, S.A. & Joss, P.C. 1983, in *Accretion Driven Stellar X-ray Sources*, ed. Lewin, W.H.G. & van den Heuvel, E.P.J. (Cambridge Univ. Press), 1
- Rappaport, S.A. & Joss, P.C. 1984, *Ann. Rev. Astr. Astrophys.*, 22, 537

-
- Sahu, P.K., Basu, R., & Datta, B. 1993, *ApJ*, 416, 267
 - Salgado, M., Bonazzola, S., Gourgoulhon, E., & Haense, P. 1994a, *A&A*, 291, 155
 - ———. 1994b, *A&AS*, 108, 455
 - Schreir, E., Levinson, R., Gursky, H., Kellogg, E., Tananbaum, H., & Giacconi, R. 1972, *ApJ Lett.*, 172, 79; Errata: 173, 51
 - Shakura, N.I., & Sunyaev, R.A. 1973, *A&A*, 24, 337
 - Shapiro, S.L., & Teukolsky, S.A. 1983, in *Black Holes, White Dwarfs, and Neutron Stars* (New York : John Wiley & Sons)
 - Shimura, T., & Takahara, F. 1995, *ApJ*, 445, 780
 - Stergioulas, N. 1998, in “Living Reviews in Relativity”, Vol. 1
 - Stergioulas, N., Kluźniak, W., & Bulik, T. 1999, *A&A*, 352, L116
 - Strobel, K., & Weigel, M.K. 2001, *A&A* 367, 582
 - Strobel, K., Schaab, C., & Weigel, M. K. 1999, *A&A*, 350, 497
 - Sunyaev, R.A., & Shakura, N.I. 1986, *Sov. Astrn. Lett.*, 12, 117
 - Taam, R.E. & van den Heuvel, E.P.J. 1986, *ApJ*, 305, 235
 - Tanaka, Y., & Shibazaki, N. 1996, *Ann. Rev. Astr. Astrophys.*, 34, 607
 - Tananbaum, H., Gursky, H., Kellogg, E., Giacconi, R., & Jones, C. 1972, *ApJ Lett.*, 177, 5
 - Terazawa, H. 1979, *INS Rep.*, 336, (Univ. Tokyo, INS)
 - Thampan, A.V. 1999, in *Ph.D. Thesis*
 - Thampan, A.V., & Datta, B. 1998, *MNRAS*, 297, 570
 - Titarchuk, L., Lapidus I., Muslimov, A. 1998, *ApJ*, 499, 315
 - Titarchuk, L.G., & Osherovich, V.A. 1999, *ApJ*, 518, L95
 - Titarchuk, L., & Osherovich, V. & Kuznetsov, S. 1999, *ApJ*, 525, L129
 - Tsesevich, V.P. 1973, *Eclipsing Variable Stars* (Wiley, New York)

- van der Klis, M. 1995, in X-Ray Binaries, ed. Lewin, W.H.G., van Paradijs, J., & van den Heuvel, E.P.J., 252
- van der Klis, M. 2000, *Ann. Rev. Astr. Astrophys.*, 38, 717
- van der Klis, M., Wijnands, R.A.D., Horne, K., & Chen, W. 1997, *ApJ*, 481, L97
- van Paradijs, J. 1979, *ApJ*, 234, 609
- van Paradijs, J. 1989, in *Timing Neutron Stars*, eds. Ogelman, H., & van den Heuvel, E.P.J. (Kluwer Academic Publishers, Dordrecht), 191
- van Paradijs, J., 1995, in X-Ray Binaries, ed. Lewin, W.H.G., van Paradijs, J., & van den Heuvel, E.P.J., 536
- Vrtilik, S.D., Raymond, J.C., Garcia, M.R., Verbunt, F., Hasinger, G., & Kürster, M. 1990, *A&A*, 235, 162
- Walecka, J.D. 1974, *Ann. Phys.*, 83, 491
- Walter, F.M., Bowyer, S., Mason, K.O. & Clarke, J.T. et al. 1982, *ApJ Lett.*, 253, 67
- White, N.E. 1995, in X-Ray Binaries, ed. Lewin, W.H.G., van Paradijs, J., & van den Heuvel, E.P.J., 1
- White, N.E., Stella, L., & Parmar, A.N. 1988, *ApJ*, 324, 363
- White, N.E., & Swank, J.H., 1982, *ApJ Lett.*, 253, 61
- Wijnands, R., Homan, J., Van der Klis, M., Kuulkers, E., van Paradijs, J., Lewin, W.H.G., Lamb, F.K., Psaltis, D., & Vaughan, B. 1998, *ApJ*, 493, L87
- Wijnands, R., & Van der Klis, M. 1998, *Nature*, 394, 344
- Witten, E. 1984, *Phys. Rev. D*, 30, 272
- Xu, R.X., & Busse, F.H. 2001, [astro-ph/0101011](#)
- Xu, R.X., Qiao, G. J., & Zhang, B. 1999, *ApJ*, 522, L109
- Xu, R.X., Zhang, B., & Qiao, G. J. 2001, *Astroparticle Phys.*, 15, 101
- Yamada, T., & Fukue, J. 1993, *PASJ*, 45, 97
- Zdzunik, J.L. 2000, *A&A*, 359, 311

- Zdunik, J.L., Bulik, T., Kluźniak, W., Haensel, P., & Gondek-Rosinska, D. 2000a, *A&A*, 359, 143
- Zdunik, J.L., Haensel, P., Gondek-Rosinska, D., & Gourgoulhon, E. 2000b, *A&A*, 356, 612
- Zeldovich, Ya. B., & Guseynov, O.H. 1965, *ApJ*, 144, 840

List of Publications

Appeared or In Press (In Refereed Journals)

- [1] Study of accretion discs around rapidly rotating neutron stars in general relativity and the implications for four Low Mass X-ray Binaries, Sudip Bhattacharyya, 2001, *Astronomy and Astrophysics*, in press (astro-ph/0112178).
- [2] Limits to the mass and the radius of the compact star in SAX J1808.4-3658 and their implications, Sudip Bhattacharyya, 2001, *Astrophysical Journal Letters*, **554**, 185.
- [3] Temperature profiles of accretion discs around rapidly rotating strange stars in general relativity: a comparison with neutron stars, Sudip Bhattacharyya, Arun V. Thampan & Ignazio Bombaci, 2001, *Astronomy and Astrophysics*, **372**, 925.
- [4] General relativistic spectra of accretion discs around rapidly rotating neutron stars: Effect of light bending, Sudip Bhattacharyya, Dipankar Bhattacharya & Arun V. Thampan, 2001, *Monthly Notices of the Royal Astronomical Society*, **325**, 989.
- [5] General relativistic spectra of accretion disks around rotating neutron stars, Sudip Bhattacharyya, Ranjeev Misra & Arun V. Thampan, 2001, *Astrophysical Journal*, **550**, 841.
- [6] Temperature profiles of accretion disks around rapidly rotating neutron stars in general relativity and implications for Cygnus X-2, Sudip Bhattacharyya, Arun V. Thampan, Ranjeev Misra & Bhaskar Datta, 2000, *Astrophysical Journal*, **542**, 473.
- [7] Neutron stars and accretion disks in low mass X-ray binaries, Sudip Bhattacharyya, 1999, *Indian Journal of Physics*, **73B**, 889.

Submitted

- [1] Correlated X-ray timing and spectral behavior of GX 349+2: RXTE PCA data, Vivek K. Agrawal & Sudip Bhattacharyya, 2001, *Astronomy and Astrophysics*, submitted (astro-ph/0112545).

Appeared or In Press (In Conference Proceedings)

- [1] Millisecond X-Ray Pulsar SAX J1808.4-3658: Limits to the Mass and the Radius of the Compact Star, Sudip Bhattacharyya, 2001, in the proceedings of '5th Hellenic Astronomical Conference', Crete, Greece, September 20-22, 2001 (astro-ph/0112175).
- [2] General Relativistic Spectra from Accretion Disks around Rapidly Rotating Neutron Stars, Sudip Bhattacharyya, Dipankar Bhattacharya, Ranjeev Misra & Arun V. Thampan, 2001, in the proceedings of 'The Physics of Cataclysmic Variables and Related Objects', Goettingen, August 5-10, 2001 (astro-ph/0112136).